University of Nevada, Reno

Development of a Dual-Wavelength Photoacoustic Instrument for Measurement of Light Absorption and Scattering by Aerosol and Gases

A dissertation submitted in partial fulfillment of
the requirements for the degree of Doctor of
Philosophy in Atmospheric Science

by

Kristin A. Lewis

William P. Arnott, Ph.D./Dissertation Advisor

May, 2007

University of Nevada, Reno
Statewide • Worldwide

THE GRADUATE SCHOOL

We recommend that the dissertation
prepared under our supervision by

KRISTIN A. LEWIS

Entitled

Development of a Dual-Wavelength Photoacoustic Instrument
for Measurement of Light Absorption and Scattering by Aerosol and Gases

be accepted in partial fulfillment of the
requirements for the degree of

DOCTOR OF PHILOSOPHY

William P. Arnott, Ph.D., Advisor

Hans Moosmüller, Ph.D., Committee Member

Alan W. Gertler, Ph.D., Committee Member

Dhanesh Chandra, Ph.D., Committee Member

Mae S. Gustin, Ph.D., Graduate School Representative

Marsha H. Read, Ph. D., Associate Dean, Graduate School

May, 2007

Abstract

A dual-wavelength photoacoustic instrument has been developed for measurement of light absorption and scattering by aerosol and gases. The novel instrumentation allows for in situ measurement of optical properties of atmospheric constituents simultaneously at two wavelengths. Two compact diode lasers, operating at 405 nm and 870 nm, are employed, providing for assessment of spectral variation in aerosol optical properties from near-UV to near-IR wavelengths. Measurements of light scattering by reciprocal nephelometry within the instrument resonator accompany photoacoustic absorption measurements and allow for calculation of extinction. The dual-wavelength photoacoustic builds on previous single-wavelength photoacoustic instrumentation. The theory of instrument operation is described in detail, including separation and measurement of noise from signal and acoustic considerations for single and dual-wavelength absorption measurements. Also described and implemented is a simple method of instrument calibration. The calibration process utilizes NO_2 gas, salt aerosol, and kerosene-flame soot aerosol, and so covers a range of optical properties relevant to atmospheric constituents.

The dual-wavelength photoacoustic instrument was used during the 2006 Fire Lab at Missoula Experiment (FLAME) to measure optical properties of wood smoke from a variety of biomass fuels. A range of single scattering albedo values was measured for different fuel types, and the spectral dependence of absorption was quantified and parameterized using the Ångström exponent of absorption. Increased absorption at shorter wavelengths, characterized by an Ångström exponent greater than one, was found

for many highly scattering aerosols. The measurements show conclusively that light absorbing organic material is present in wood smoke. Spectral properties of this organic material, which preferentially absorbs UV and near-UV radiation, indicate that casual use of the inverse wavelength dependence of aerosol light absorption in remote sensing and modeling applications can introduce large errors at UV and visible wavelengths when extrapolated from near-IR absorption for certain types of wood smoke. The spectral variation in optical properties provides insight into differentiation of aerosols from mobile or industrial sources versus those from biomass burning. Urban aerosol measurements made on the University of Nevada, Reno campus complement laboratory wood smoke measurements and confirm instrument stability and sensitivity for ambient measurements.

Acknowledgements

It is with gratitude that I acknowledge the agencies that provided funding for various parts of this research: the National Science Foundation Major Research Instrumentation Program, the U.S. Department of Energy Atmospheric Science Program, the National Park Service, the State of Nevada Applied Research Initiative, and the University of Nevada, Reno Graduate School.

This work would not be possible without the contributions of the many researchers who lent me their time, data, and expertise throughout the extent of this project. I would like to thank Cyle Wold of the Missoula Fire Science Lab for providing the wood smoke scattering measurements, Yury Desyaterik and Alex Laskin of EMSL/PNNL for the SEM microanalysis of wood smoke particles, and researchers from Colorado State University and the National Park Service, including Derek Day and Gavin McMeeking, for providing and assisting with the IMPROVE aerosol sampler measurements. In addition, the impressive work of Stephanie Winter, who spent hours and hours pounding raw wood smoke data into a useful form, is crucial to the results presented in this paper.

I would like to thank my committee members for the time and guidance they have provided during my final progression toward graduation as well as throughout my tenure at the Desert Research Institute and University of Nevada, Reno. Thank you, Dr. William P. Arnott, Dr. Hans Moosmüller, Dr. Alan W. Gertler, Dr. Dhanesh Chandra, Dr. Jennifer Huntley-Smith, and Dr. Mae S. Gustin.

I am very grateful to my professors and collogues from the Saint Mary's College of California School of Science, the University of Oregon Department of Physics, and the Atmospheric Science Department of DRI/UNR. I would especially like to recognize Dr. Chris Ray, Dr. Jessica Kintner, Shannon O'Leary, Laura Riihimaki, Subhasharee Mishra and Dr. Pat Arnott, without whom I might be completing a very different dissertation or no dissertation at all. Beyond demonstrating to me the qualities of a good scientist, mentor and friend, they always believed in my potential in this field. The continued support of my professors and friends has given me confidence in my academic endeavors, and I look forward to continuing my education under their guidance.

The truly outstanding experience that I have had as a graduate student at the Desert Research Institute and University of Nevada is attributable to my advisor, Dr. Pat Arnott: an inspiring teacher, talented researcher, and remarkably interesting person. Thank you. I feel deeply fortunate to have been invited into your laboratory.

I would like to acknowledge my parents, my favorite people, Kim and Mary Anderson: I appreciate you so sincerely "thank you" hardly seems adequate. To my wonderful family and friends, thanks for the support; thanks for the fun.

Most of all, thank you to my husband, Daniel, whose partnership allows me to be the very best version of myself.

Table of Contents

Abstract i

Acknowledgments iii

Table of Contents v

List of Tables viii

List of Figures ix

Chapter 0. Description of Dissertation 1

0.1 Introduction 1

Chapter 1. Single-Wavelength Photoacoustic Instrumentation 4

1.1 Introduction 4

1.2 Instrument Survey 5

1.3 Photoacoustic Instrument Operation and Components 10

1.4 Photoacoustic Theory and Calculation of Light Absorption 17

1.5 Acoustic Response under Changing Pressure Conditions 23

1.6 Photoacoustic Instrument Noise 31

1.7 Scattering Measurement 38

1.8 References 42

Chapter 2. Dual-Wavelength Photoacoustic Instrumentation 45

2.1 Introduction 45

2.2 Instrument Design and Laser Alignment 48

2.3 Dual-Wavelength Photoacoustic Signal Measurement 52

2.4 References 55

Chapter 3. Instrument Calibration 56

3.1 Introduction 56

3.2 Calibration Theory 58

3.3 Experimental Set-Up 60

3.4 Calibration Results 63

3.5 Discussion 78

3.6 References 81

Chapter 4. Measurement of Wood Smoke Optical Properties 82

4.1 Introduction 82

4.2 Fire Lab at Missoula Experiment (FLAME) 83

4.3 Radiative Property Parameters 87

4.4 Results 90

4.4.1 Aethalometer and Photoacoustic Analysis 90

4.4.2 Nephelometer and Photoacoustic Analysis 94

4.4.3 Spectral Response by Fuel Type 97

4.5 Conclusion 110

4.6 References 112

Chapter 5. Ambient Measurement in an Urban Environment 114

5.1 Introduction 114

5.2 Ambient Absorption Time Series 115

5.3 Meteorological Analysis 117

5.4 Spectral Variation of Ambient Aerosol Light Absorption 124

5.5 Conclusion 133

5.6 References 134

Chapter 6. Summary, Conclusions, and Future Work 136

6.1 Summary and Conclusions 136

6.2 Future Work 138

Appendix A. Polynomial Fit of Acoustic Pressure Response Equation during Acoustic Calibration 140

List of Tables

Table 1.1	Theoretical and empirical linear parameters from Equation 1.23	30
Table 4.1	Fuel listing and classification for FLAME 2006 chamber burns	86
Table 4.2	Summary of carbon components measured by the TOR combustion method as a function of temperature and added oxygen	105

List of Figures

Figure 1.1	Schematic of the photoacoustic resonator and instrument components	11
Figure 1.2	Acoustic standing wave in resonator	12
Figure 1.3	Illustration of the characteristics of the critical orifice	17
Figure 1.4	Acoustic noise within the resonator under conditions of changing pressure	24
Figure 1.5	Inverse of resonator quality factor as a function of the inverse of the square root of resonator pressure	28
Figure 1.6	Inverse of the square root of ambient pressure as a function of resonance frequency	30
Figure 1.7	Idealized illustration of microphone power magnitude as a function of frequency, including both signal and noise	35
Figure 1.8	Acoustic noise as a function of flow rate	36
Figure 1.9	Noise at varying flow rates as a function of frequency	37
Figure 1.10	Ratio of noise magnitude to noise at zero flow as a function of frequency (log plot)	38
Figure 2.1	Arrangement of lasers, long wave pass dichroic beamsplitter and mirrors in original laser combination and alignment scheme	50
Figure 2.2	Schematic of dual-wavelength photoacoustic instrument	51
Figure 3.1	Schematic of scattering aerosol production and calibration set-up	62
Figure 3.2	Schematic of absorbing aerosol production and calibration set-up	63
Figure 3.3a	NO_2 calibration time series, Run 1	64
Figure 3.3b	NO_2 calibration time series, Run 2	64
Figure 3.4	NO_2 gas calibration results	66
Figure 3.5a	Scattering calibration time series, Run 1	68

Figure 3.5b	Scattering calibration time series, Run 2	68
Figure 3.5c	Scattering calibration time series, Run 3	69
Figure 3.6a	Scattering calibration results at 405 nm	70
Figure 3.6b	Scattering calibration results at 870 nm	70
Figure 3.7a	Kerosene soot absorption calibration time series, Run 1	72
Figure 3.7b	Kerosene soot absorption calibration time series, Run 2	72
Figure 3.8a	Kerosene soot absorption calibration results at 405 nm, new scattering calibration factors applied	74
Figure 3.8b	Kerosene soot absorption calibration results at 870 nm, new scattering calibration factors applied	74
Figure 3.9a	Kerosene soot absorption calibration results at 405 nm, new scattering calibration factors not applied	76
Figure 3.9b	Kerosene soot absorption calibration results at 870 nm, new scattering calibration factors not applied	76
Figure 3.10	Single scattering albedo time series for kerosene-flame soot absorption calibration runs	78
Figure 4.1	FLAME chamber burn experimental set-up	85
Figure 4.2	Chamise fuel: Aethalometer and dual-wavelength photoacoustic measurements	93
Figure 4.3	Rice straw fuel: Aethalometer and dual-wavelength photoacoustic measurements	94
Figure 4.4	Chamise fuel: nephelometer and photoacoustic measurements of scattering coefficient	96
Figure 4.5	Rice straw fuel: nephelometer and photoacoustic measurements of scattering coefficient	96
Figure 4.6	Ångström exponent of absorption *b(405/870)* versus single scattering albedo at 405 nm for all FLAME burns	99

Figure 4.7	Ångström exponent of absorption *b(532/870)* versus single scattering albedo at 532 nm for all FLAME burns	100
Figure 4.8	Average photoacoustic absorption and scattering percent by burn, 405 nm	103
Figure 4.9	Average photoacoustic absorption and scattering percent by burn, 870 nm	103
Figure 4.10	Percent mass concentration by burn: inorganic material, organic carbon, and elemental carbon components	107
Figure 4.11	CCSEM/EDX image from chamise burn (burn B)	109
Figure 4.12	CCSEM/EDX image from ponderosa pine burn (burn A)	109
Figure 4.13	CCSEM/EDX image from rice straw burn (burn E)	110
Figure 5.1a	Ambient photoacoustic measurements of aerosol absorption, 405 nm	116
Figure 5.1b	Ambient photoacoustic measurements of aerosol absorption, 870 nm	116
Figure 5.2	Wind speed time series	118
Figure 5.3a	Reno atmospheric sounding: December 24, 2006; 4:00 LST	120
Figure 5.3b	Reno atmospheric sounding: December 24, 2006; 16:00 LST	120
Figure 5.4a	Reno atmospheric sounding: December 26, 2006; 4:00 LST	121
Figure 5.4b	Reno atmospheric sounding: December 26, 2006; 16:00 LST	122
Figure 5.5a	Reno atmospheric sounding: December 21, 2006; 4:00 LST	123
Figure 5.5b	Reno atmospheric sounding: December 21, 2006; 16:00 LST	124
Figure 5.6a	Ambient measurements of absorption at 405 nm over 24 hours, December 21 – 25, 2006	126
Figure 5.6b	Ambient measurements of absorption at 870 nm over 24 hours, December 21 – 25, 2006	126
Figure 5.7a	Ambient measurements of absorption at 405 nm over 24 hours, December 28 – 31, 2006 and January 2, 2007	127

Figure 5.7b Ambient measurements of absorption at 870 nm over 24 hours, December 28 – 31, 2006 and January 2, 2007 127

Figure 5.8 Ångström exponent of absorption; average by day of ambient measurement 129

Figure 5.9 Ångström exponent of absorption over a 24-hour day 130

Figure 5.10a Occurrence of Ångström exponent values from midnight to 10:00 132

Figure 5.10b Occurrence of Ångström exponent values from 10:00 to 16:00 132

Figure 5.10c Occurrence of Ångström exponent values from 16:00 to midnight 132

0 Description of Dissertation

0.1 Introduction

The properties of suspended particulate matter in air, or atmospheric aerosol, are studied by research scientists for a number of reasons. Particles can reduce visibility and pose a health hazard when inhaled. An area of aerosol research where numerous questions remain lies in the role of particles in the distribution of atmospheric energy and climate change. Because they absorb and scatter radiation, atmospheric aerosols have the potential to modify climate. In order to appreciate the impact that particles from different sources have on the global radiation balance, absorption and scattering properties of aerosols must be better understood. One parameter of importance in this research, in that optical properties are rarely measured across the entire solar spectrum, is how absorption and scattering coefficients of an aerosol depend on wavelength. A number of instruments exist to measure aerosol properties, including absorption and scattering by the particles at varied wavelengths. The novel dual-wavelength photoacoustic instrumentation described in this dissertation not only seeks to contribute answers to questions concerning the optical properties of aerosol and gases, but also improves upon existing instrumentation currently employed in atmospheric measurements.

The dissertation is organized as follows. The first two chapters provide detailed instrument descriptions, and Chapter 3 discusses evaluation of the calibration of the described instrumentation. Chapters 4 and 5 present two separate applications of the instrument for measurement of light absorption and scattering by aerosol particles from different combustion sources.

Much of Chapter 1 serves as a review. Along with a presentation of other commonly employed instrumentation for measurement of aerosol and gas optical properties, components and operation of the single-wavelength photoacoustic instrument, much of which has been previously discussed in the literature, are described in detail. In addition to this instrument review, Chapter 1 includes expansion upon previously published work. Operational theory of the photoacoustic instrument concerning phase sensitive detection and measurement of noise are presented for the first time. New measurements that contribute to an understanding of instrument operation are also discussed in Chapter 1: measurement of acoustic response under changing pressure conditions, and measurement of acoustic noise as a function of flow rate and frequency.

The dual-wavelength photoacoustic instrument and its development, described in Chapter 2, are entirely novel and presented for the first time in this dissertation. Photoacoustic instrument calibration using NO_2 gas and absorbing kerosene-flame soot aerosol have previously been conducted separately. The calibration evaluation described in Chapter 3 integrates several calibration methods to explore their consistency. Calibration using both gas and two different particle species (NO_2 gas, kerosene-flame soot, and scattering salt aerosol) is also conducted and described here for the first time.

The initial and most important application of the dual-wavelength instrument is discussed in Chapter 4: measurement of wood smoke optical properties from a variety of biomass fuels during a campaign that took place at the Fire Sciences Laboratory in Missoula, Montana during spring of 2006. Aerosol absorption and scattering measurements made by two photoacoustic instruments and a 7-wavelength Aethalometer are presented with integrating nephelometer and IMPROVE aerosol sampler

measurements obtained from experiment collaborators. Analysis of all data in both Chapters 4 and 5 was conducted by the author of this dissertation, and all conclusions represent her contribution. The second application of the instrument, described in Chapter 5, involved urban ambient measurements made during the winter of 2007 in Reno, Nevada. These measurements served primarily to evaluate the dual-wavelength instrument's use in ambient applications rather than quantify properties of Reno air quality. However, the 14-day ambient data set of absorption measurements made at two wavelengths suggests certain interesting hypotheses regarding aerosol spectral properties and source apportionment in light of wood smoke results obtained from the Fire Lab measurements reported in Chapter 4. Absorption and scattering measurements made at 405 nm during both the wood smoke and ambient campaigns are particularly unique in that no photoacoustic measurements at this wavelength have been previously analyzed.

1 Single-Wavelength Photoacoustic Instrumentation

1.1 Introduction

One important element in the complex system of atmospheric radiation transfer involves the optical properties of aerosol. Beyond the negative consequences that aerosols pose to human health and visibility, they also affect the lifetime of clouds and global radiation balance (Horvath, 1993; Lohmann and Feichter, 2005). The primary means of particulate interaction with radiation are aerosol light absorption and scattering, or the sum of these: light extinction. It is the proportion of light scattering to extinction that determines whether a particular aerosol species will provide a cooling or warming effect on the atmosphere. Sulfate and nitrate aerosols from anthropogenic sources, which predominately scatter radiation, are thought to be counteracting to some extent global warming caused by greenhouse gases such as carbon dioxide (Charlson et al., 1992). Light absorbing particles, primarily produced by incomplete combustion of carbonaceous fuels, have the opposite effect and warm the atmosphere. In fact, it has been proposed that the warming effect of carbonaceous aerosols may balance the cooling effect of scattering aerosols (Jacobson, 2001). Uncertainties in the source magnitude, global distribution and mixing state of light absorbing aerosols only compound the challenges posed to climate modelers and experimentalists due to measurement discrepancies and further issues related to the absorption and scattering properties of the particulates (Andreae, 2001).

The only method available to directly measure light absorption by suspended atmospheric particles is use of the photoacoustic instrument. The instrument described in

this chapter quantifies both absorption, by the photoacoustic method, and scattering, utilizing reciprocal nephelometry. Instrument properties and measurement method, including acoustic response, calibration and noise considerations, will be discussed.

1.2 Instrument Survey

Aerosol light absorption is most commonly measured by removing suspended particles from the air and depositing them at a known flow rate on a filter. Light absorption is then measured using a radiation source to illuminate the loaded filter and an optical detector to quantify incremental changes in transmittance or reflectance with time. The filter substrate causes multiple scattering enhancement of particle light absorption to amplify the signal, and thus improves the sensitivity of such measurements. However, filter interactions also provide the primary challenge posed by the instruments: to determine appropriate calibration.

The Particle Soot Absorption Photometer (PSAP) manufactured by Radiance Research, Seattle, WA and the Aethalometer by Magee Scientific (Hansen, Rosen, and Novakov, 1984) are widely used filter-based instruments which produce real-time measurements. Both single and multi-wavelength versions of the Aethalometer are commercially available. A modified version of the PSAP, which measures absorption at three wavelengths (467 nm, 530 nm, and 660 nm) has been developed and calibrated but is not commercially available (Virkkula et al., 2005).

Errors in absorption measurements by the PSAP exist due to filter interactions and aerosol scattering effects. An artifact absorption will be produced by the PSAP if light-scattering particles cause attenuation of radiation through a loaded filter. The structure of

the filter medium is designed to minimize detrimental effects of light scattering by its optically diffuse properties. The manufacturer's calibration for PSAP measurement seeks to amend the nonlinear instrument response of a loading filter as well as the augmentation of absorption by the filter substrate. The instrument, however, was found to interpret about 2% of scattering as absorption. After correcting for this effect an additional empirical correction of 22% was found necessary to rectify overestimates in absorption measurements (Bond, Anderson, and Campbell, 1999). The calibration requires an additional instrument for quantification of light scattering by the aerosol sample, and is valid for filter transmission between 70 and 100 percent. Further review of the empirical calibration proposed by Bond et al. (1999) was conducted during the Reno Aerosol Optics Study (RAOS) (Sheridan et al., 2005). While the Bond et al. (1999) calibration was found to provide a reasonable correction for atmospherically relevant aerosol samples (those with absorption levels less than 25 Mm^{-1} and single scattering albedo between 0.8 and 0.85), a less favorable agreement with RAOS results was found for lower single scattering albedos associated with sources such as diesel vehicle emissions, for example.

Aethalometers are calibrated by the manufacturer to present mass concentration of black carbon as opposed to aerosol light absorption. However, recent work has sought determination of aerosol light absorption coefficients from Aethalometer measurements (Arnott et al., 2005a; Weingartner et al., 2003). Efforts to this end by Arnott et al. (2005a) produced an algorithm to quantify light absorption from Aethalometer black carbon mass concentration that accounts for the scattering offset described above as well as filter loading effects. Because light absorption measurement by particles embedded on

a filter is strongly affected by multiple scattering the Aethalometer tends to overestimate absorption on a clean filter and underestimate it on a loaded filter. The filter loading effects come about because light absorption by particles on a loaded filter causes a reduction in the multiple scattering enhancement factor, and thereby produces an apparent reduction in measured values. The Arnott et al. (2005a) Aethalometer calibration also requires additional instrumentation to provide measurements of light scattering to correct for scattering effects on filter transmission. Another unresolved issue in filter-based measurement of light absorption is the effect of particle deposition within and on the surface of the filter, as the optical signal is expected to be dependent on depth and uniformity of particle positioning in the filter substrate (Arnott et al., 2005a).

The large physical variation in aerosol properties such as single scattering albedo, particle size or mixing state is such that suitable calibration for filter-based instruments is a challenge. In spite of the numerous attempts to correct for filter-based artifacts, the complexities of ambient aerosol properties and their interaction with the filter substrate have prevented determination of a universal calibration scheme for PSAPs and Aethalometers (Andreae and Gelencser, 2006).

The Multi-Angle Absorption Photometer (MAAP) is a filter-based instrument for measurement of aerosol light absorption that does not require parallel measurement of light-scattering coefficients for calibration (Petzold et al., 2005; Petzold and Schönlinner, 2004). In addition to transmission, the MAAP measures back-scattered radiation at multiple angles to better determine irradiances in the forward and back hemispheres and account for optical effects of the filter and light-scattering particles. Absorptivity is

acquired from the difference of total irradiance and filter transmissivity plus filter reflectivity.

The prototypical instrument for measuring light scattering by aerosols is the integrating nephelometer by TSI Incorporated, Shoreview, MN. The TSI Model 3563 measures total scattering coefficient and backscattering coefficient at three wavelengths: 450, 550 and 700 nm. Operation of the integrating nephelometer is as follows. An air sample is continually drawn through the sample volume and is illuminated over an angle of 7 to 170 degrees by a cosine-weighted diffuse light source. Photomultiplier tubes (PMTs) serve as radiation detectors and view the scattering volume. Geometrical integration of the angular distribution of radiation scattered by either a gas or aerosol sample allows for calculation of the sample's scattering coefficient (Anderson et al., 1996). High-pass and band-pass filters separate scattered light into three wavelengths prior to the PMTs, and a shutter is employed to block light from scattering angles less than 90^{o} when measurement of hemispherical backscatter is desired. Rayleigh scattering of the air itself along with PMT dark current are background subtracted from the measured scattering signal, and the instrument compensates for any changes in the light source. The nephelometer can be calibrated using a gas with a known scattering coefficient such as carbon dioxide.

Extensive assessment of the uncertainties (Anderson et al., 1996) and recommended calibrations (Anderson and Ogren, 1998) for the model 3563 TSI integrating nephelometer have been developed. The largest source of systematic uncertainty in the integrating nephelometer's measurements, as determined by Anderson et al. (1996), arises from nonidealities in the wavelength and angular sensitivities of the

nephelometer. Because light scattering is measured over a narrow but finite wavelength range that is not perfectly centered on the nominal value nonidealities in wavelength come about. Nonidealities in angular sensitivity stem from a number of sources, including imperfect cosine-weighted illumination intensity and instrument geometry restrictions that reduce scattering angle viewing from the ideal range of 0^o to 180^o to 7^o to 170^o. Therefore, near-forward and near-backward scattering are not measured by the detector. Wavelength and angular nonidealities are strongly dependent on particle size, with increased error for larger particles.

Scattering by particles or gas molecules that are significantly smaller than the wavelength of incident light is referred to as Rayleigh scattering. In this regime light scattering has simple properties, such as symmetrical forward and backward scattering and a well understood relation between molecule/particle diameter and coefficient of scattering, so that nonidealities are not size dependent. However, for scattering particles of size on the same order as the wavelength of incident light (the Mie scattering regime) the scattering phase function (the angular geometry of scattered light) is strongly size dependent. To compound the problem, the phase function of coarse particles in the Mie regime is dominated by near-forward diffraction, much of which is not detected due to the 7^o truncation angle (Moosmuller and Arnott, 2003). Unfortunately scattering is most efficient and most particle mass exists in this regime. The particle size-dependent errors introduced by nephelometer nonidealities, such as truncation angle, are limited by instrument design.

The photoacoustic instrument represents the only instrument that can measure aerosol light absorption directly on airborne particulate matter. It provides a

measurement that can be compared to the more commonly used PSAP and Aethalometer, but it is without the filter-based artifacts and resulting correction factors. An evaluation mechanism for calibration of light absorption by the photoacoustic instrument exists in employing light absorbing gases such as nitrogen dioxide (Arnott, Moosmüller, and Walker, 2000). The large dynamic range of measurement provides another advantage to photoacoustic spectrometry. Finally, inclusion of scattering measurement along with light absorption within a single instrument allows for calculation of extinction, the most important factor in a particle's radiative forcing effect on the atmosphere.

1.3 Photoacoustic Instrument Operation and Components

In operation of the photoacoustic instrument sample air is continuously drawn through an acoustic resonator. The sample air is illuminated by laser radiation that is power modulated at the resonance frequency of the cavity. Radiation is absorbed by aerosol particles within the sample resulting in particle heating, and due to the very small size and high thermal conductivity of the particulates this heat is rapidly transferred to the surrounding air. A change in pressure is induced by the heated air. The varying pressure disturbance caused by particle heat transfer is amplified by constructive interference associated with the standing wave in the resonator because the laser is modulated at resonance frequency. The pressure fluctuations are measured using a microphone on the resonator. Therefore, aerosol light absorption, manifested by particle heat transfer, is measured by the microphone as an acoustic signal (Arnott et al., 1999).

The microphone dynamic range covers at least 6 orders of magnitude, resulting in a very large dynamic range for light absorption measurement (Arnott et al., 2005b). The

microphone signal is first amplified by the microphone preamplifier, and the signal is then again amplified using a low-noise programmable preamplifier (model SR560, Stanford Research Systems, Sunnyvale, CA). The programmable preamplifier also serves as a broad band-pass filter, usually set to permit frequencies between 300 Hz and 10 kHz. The nominal resonance frequency is 1500 Hz.

A schematic of the resonator section of the photoacoustic instrument along with the laser and photodetector is shown in Figure 1.1.

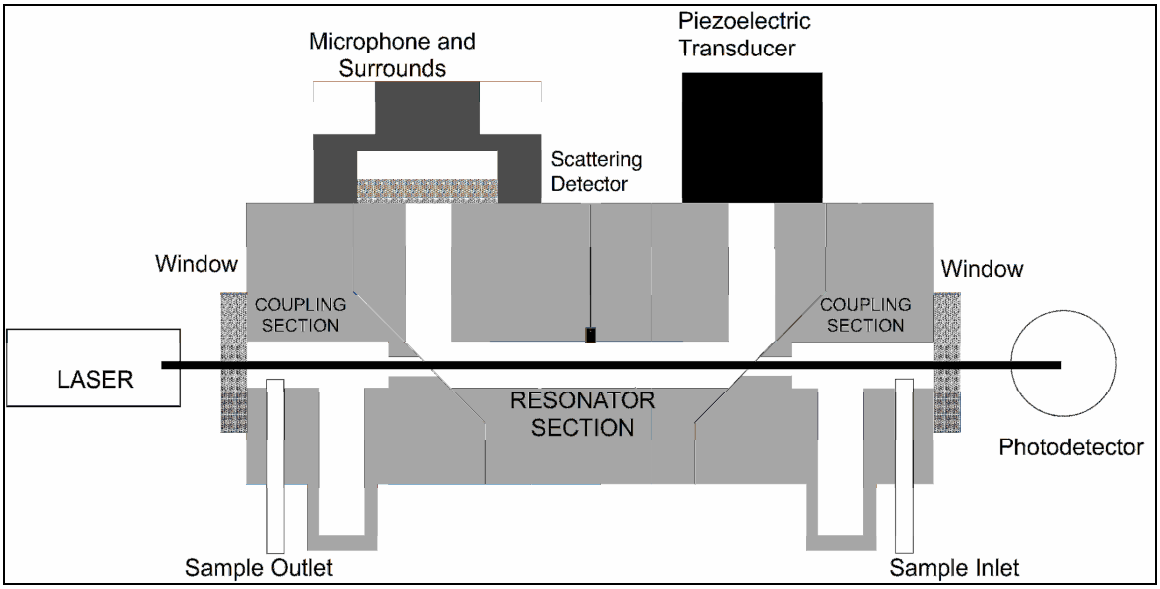

Figure 1.1 Schematic of the photoacoustic resonator and instrument components, including microphone and mounting surrounds, scattering detector, piezoelectric transducer, laser, and photodetector

The resonance cavity is one acoustic wavelength in length and *U*-shaped, such that the horizontal section is ½ of an acoustic wavelength long and the two vertical sections are ¼ of a an acoustic wavelength long. Low pressure nodes of the standing wave exist at the 90^{o} corners of the resonator. High pressure antinodes exist at the center of the horizontal section, where sample illumination occurs, and at both ends of the vertical sections. This design allows for entrance and exit of the laser beam and air sample at the low pressure

sections of the standing wave, causing minimal disturbance to the acoustic signal. Much like how the nodes of a standing wave on a string can be pinched and the string wave will continue to oscillate unimpeded, so do the laser and sample inlet and outlet in the resonator reside at the nodes of the acoustic standing wave to prevent wave interference. The microphone resides at one end of the U-shaped resonator, and a piezoelectric transducer is at the other end. The center of the cavity where particle heat transfer takes place and the ends where the microphone and piezoelectric signals are measured contain high pressure points of the acoustic standing wave that are 180^{o} out of phase (i.e. positive versus negative pressure) in the cycle. See Figure 1.2 for an illustration of the standing wave.

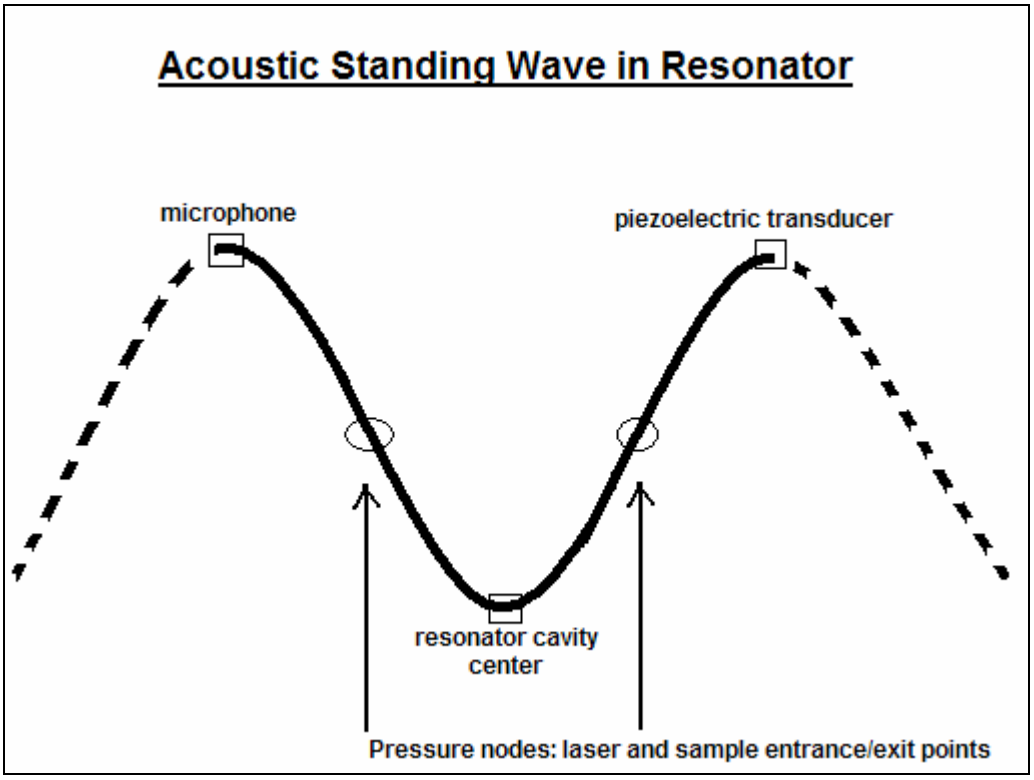

Figure 1.2 The laser beam and air sample enter and exit the resonator at stationary points of the standing wave. High-pressure antinodes exist at microphone, piezoelectric transducer and central cavity locations.

Also located on the center of the resonator cavity is a cosine-weighted detector fiber coupled to a photomultiplier tube for light scattering detection, explained further in Section 1.7.

The resonance frequency of the resonator cavity, f_o, depends on the speed of sound and, therefore, is a function of the ambient temperature and relative humidity. The piezoelectric transducer is utilized to determine the resonance frequency along with resonator quality factor (gain) during acoustic calibrations of the instrument. During acoustic calibrations the piezoelectric transducer acts as a sound source to scan the frequency response of the resonator. Pressure is measured as a function of frequency within the vicinity of resonance, resulting in a pressure curve that peaks at f_o. The theory related to the acoustic calibration is discussed in Section 1.4 and in Appendix A.

A diode laser serves as a convenient radiation source for the photoacoustic instrument. The acoustic signal is proportional to laser beam power, so that the laser must meet certain power standards depending on the necessary range of absorption measurements. Currently on five of the instruments in use the modulated laser power ranges from 2 to 1000 milliwatts (mW). The radiation wavelength is chosen such that gaseous absorption in atmospheric conditions is minimal, and operation is selected at a wavelength where a power modulated diode laser source is available The motivation for measurement also determines laser wavelength, such as whether absorption and scattering measurements of ultraviolet (UV), visible, or infrared (IR) radiation are desired. It has been shown that absorption at near-IR or IR wavelengths responds overwhelmingly to the elemental or black carbon nature of carbonaceous aerosol, while

absorption at ultraviolet wavelengths responds to organic carbon components as well (Kirchstetter, Novakov, and Hobbs, 2004).

It was stated in the introduction that the primary light absorbing species in the atmosphere is aerosol produced by incomplete combustion of carbonaceous fuels. Further discussion and definition of terms commonly used in the atmospheric sciences to describe such aerosol is warranted, and will serve as a brief aside in this paragraph. The terms *elemental carbon* and *black carbon* are both operational definitions that evidence their methods of evaluation. *Elemental carbon* relates to the chemistry of the compound, and generally identifies carbon that does not volatilize below a certain temperature. For certain combustion processes and fuel types, such as diesel exhaust, a strong correlation has been shown between elemental carbon content and light absorption. In atmospheric science *black carbon* refers to light-absorbing carbonaceous particulates and is expected to satisfy the following assumptions. Black carbon is strongly absorbing across a broad wavelength spectrum such that absorption is inversely proportional to wavelength, and light absorption is proportional to mass concentration for small particles. Use of the term *black* is often associated with measurement of carbon compounds by filter-based optical methods, such as the Aethalometer. Two much more general terms that have somewhat fallen out of favor in describing light-absorbing aerosols are *soot* and the very early reference of *smoke*. *Soot* can describe any darkly-colored absorbing aerosol containing carbon and generated by combustion (Bond and Bergstrom, 2006). Because the photoacoustic instrument measures light absorption properties of atmospheric aerosol, the terms most commonly used in this discussion will be *black carbon* or, more often, *light absorbing carbon*, as suggested by Malm et al. (1994) and Bond and Bergstrom (2006),

to denote the light-absorbing and carbonaceous nature of the compound in question without inferring the properties or assumptions that are implied by other commonly used terms.

Laser power during instrument operation is measured by a photodiode after the laser beam exits the acoustic resonator. The photodiode resides on an integrating sphere situated far enough away from the resonator to prevent back scatter of light back into the sample cavity. Laser power measurement is necessary in part as signal calibration because the acoustic signal is proportional to laser power; the laser power measurement is directly used in calculating light absorption. In measuring very high concentrations of light-absorbing and/or scattering species the decrease in measured laser power due to light extinction can also serve as a means to calibrate the response of the instrument.

Pressure, temperature and relative humidity sensors are located on the sample line downstream of the resonator cavity, and their measurements serve as reference to the basic thermodynamic conditions of the air sample. Two filters are also present on the photoacoustic instrument. The first is prior to the inlet into the acoustic resonator and through which the air sample can be diverted to filter out any aerosol entering the cavity in order to make a background measurement of light absorption during a "zeroing" of the instrument. Background light absorption is subtracted from the sample light absorption signal. The photoacoustic instrument can be set to automatically zero itself regularly, such as every 200 measurements, or an immediate zeroing of the measurement can be accomplished at any time during operation. A background signal can arise from slight misalignment of the laser beam and resulting absorption and heat transfer by the cavity walls, or from absorption by the gaseous portion of the sample, such as NO_2 absorption.

The filter currently used on the instrument in this position is much smaller than those employed in the past to facilitate rapid equilibrium of the filter substrate to changing ambient temperature and relative humidity conditions. A small flow of ambient air is sustained at all times through this filter to maintain this equilibrium.

Flow rate through the photoacoustic instrument is regulated by a critical orifice located on the sample line downstream of the resonator and upstream of the sampling pump. The typical flow rate is approximately 1 liter per minute (LPM). A critical orifice is a simple, very narrow hole which under sufficient suction conditions causes a pressure drop of at least 50% directly downstream of the orifice compared to the pressure upstream in the resonator. Air velocity through the orifice reaches the speed of sound; flow rate is critical and remains constant. Flow rate through a critical orifice is proportional to the hole area. An important advantage of using of a critical orifice in the photoacoustic instrument is that noise from the pump is blocked at the orifice point and unable to enter the instrument cavity through the pump line and clutter the acoustic signal. Because air traveling through the critical orifice is moving at the speed of sound, any sound from the pump traveling toward the sample cavity and also moving at this speed reaches a barrier of sorts in air moving the opposite direction and, therefore, proceeds no further. This sound is instead returned to the pump. An illustration of the critical orifice is shown in Figure 1.3.

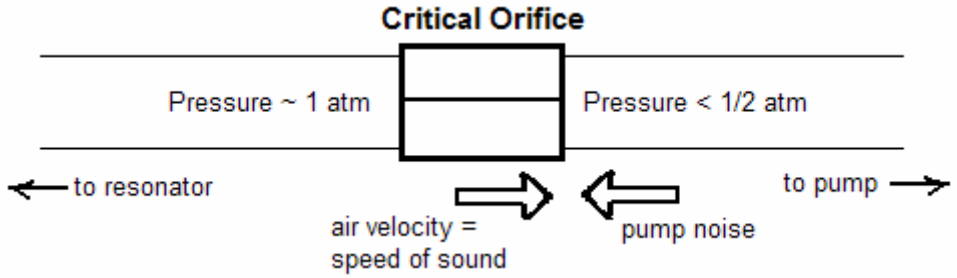

Figure 1.3 Illustration of the characteristics of the critical orifice, including 50% pressure drop, air speed through the orifice, and blockage of pump noise traveling toward the resonator

A second filter is located in the sample line upstream of the critical orifice to remove particulate matter that has the potential to clog the hole.

1.4 Photoacoustic Theory and Calculation of Light Absorption

Light absorption, β_{abs}, measured in dimensions of inverse distance, is proportional to the measured microphone power at resonance frequency, $P_m(f=f_o)$, divided by laser power at resonance, $P_L(f=f_o)$. Fourier transformations of both microphone response and laser power measurement transform the time domain signals into complex functions in the frequency domain for determination of microphone and laser power values at the resonance frequency, f_o. Fourier analysis of the microphone and laser power signals also allows for phase sensitive detection of the light absorption signal. Light absorption is also a function of resonator cross sectional area, A_{res}, resonator quality factor, Q, and resonance frequency. The full expression for calculating β_{abs} is given by the photoacoustic equation:

$$\beta_{abs} = \frac{P_m}{P_L}\frac{A_{res}}{\gamma - 1}\frac{\pi^2 f_o}{Q}\cos(\phi_M - \phi_L) \qquad \text{(Eq. 1.1)}$$

where γ is the ratio of isobaric and isochoric specific heats for air. For dry air $\gamma = 1.4$; in general γ is dependent upon relative humidity, but negligibly so in this application. The purpose of the cosine is discussed next.

Fourier transformation of the time dependent microphone signal (a measure of absorption-induced pressure fluctuations) and photodiode signal (a measure of laser power) transforms each into a complex function of frequency. The complex values of the microphone and photodiode signal in the frequency domain are determined at a very narrow bandwidth of 1 Hz width centered at the resonance frequency. It is convenient to represent the complex microphone and laser powers at resonance in phasor form, which includes the magnitude (P_m or P_L) and phase (φ_m or φ_L) of the complex value:

$$\text{Complex Microphone Power (at resonance)} \equiv \tilde{P}_m(f_o) = P_m e^{i\phi_m} \qquad \text{(Eq. 1.2)}$$

$$\text{Complex Laser Power (at resonance)} \equiv \tilde{P}_L(f_o) = P_L e^{i\phi_L} \qquad \text{(Eq. 1.3)}$$

The measured value of β_{abs} is proportional to the real part of the ratio of complex microphone and photodiode signals,

$$\beta_{abs}(f_o) \sim \mathrm{Re}\left[\frac{\tilde{P}_m(f_o)}{\tilde{P}_L(f_o)}\right] = \mathrm{Re}\left[\frac{P_m e^{i\phi_m}}{P_L e^{i\phi_L}}\right] = \mathrm{Re}\left[\frac{P_m}{P_L} e^{i(\phi_m - \phi_L)}\right] = \frac{P_m}{P_L}\cos(\phi_m - \phi_L)$$

(Eq. 1.4)

Therefore, the actual light absorption measurement includes the ratio of microphone and laser power magnitudes at resonance frequency multiplied by the cosine of the difference of microphone and laser signal phases. Any part of the microphone signal that is induced by heat transfer due to light absorption will be in phase with the laser power, its source.

Phase sensitive detection is, therefore, referenced to the frequency of laser power modulation. When the phase difference between the microphone and photodiode signals is zero the cosine in Equation 1.4 will be maximized, as will the light absorption signal. Phase sensitive detection of β_{abs} allows the signal due to aerosol light absorption to be separated more effectively from acoustic noise.

Quantities Q and f_o are dependent on pressure, temperature, and relative humidity (RH). Resonance frequency and quality factor are determined using the piezoelectric transducer every 100 to 200 measurements. The piezoelectric transducer and microphone are used to obtain a frequency response within the vicinity of resonance. The response is manipulated to a quadratic curve of microphone pressure as a function of frequency to determine the values of resonator quality factor and resonance frequency. The resonance scan conducted by the piezoelectric transducer takes about 3 seconds to complete. Peak pressure at resonance, P_o, is also determined by the curve fit. Though it is not necessary for calculation of β_{abs}, P_o is a useful quantity in confirming continued performance and calibration of the microphone (Arnott et al., 2006). The details of Q, f_o, and P_o determination are explained in Appendix A.

The frequency of operation of the photoacoustic instrument, that is the resonance frequency and frequency of laser modulation, is approximately 1500 Hertz (Hz), with slight variation from this value depending on pressure, temperature, and RH conditions. The choice of operation frequency is limited from above by the miniscule but finite heat capacity of the aerosol particles and the resulting particle heat transfer time. The important time scale for heat transfer by the particle is the reciprocal of the resonance frequency, or the acoustic period. Illuminated particles must have enough time to absorb

radiation, and then transfer the absorbed heat to the surrounding air before the next laser pulse arrives to repeat the process and build the standing pressure wave. Chan (1975) reports that this time delay is generally on the order of 1 to 50 microseconds (μs) for aerosols in air, and is dependent upon particle size distribution. This time delay prohibits ultra high frequency operation, but has proven neglectable under standard operation of the photoacoustic instrument (Arnott et al., 2003). The photoacoustic resonator was originally designed for operation at a frequency of 500 Hz. When the original instrument was operated at the next available harmonic of 1500 Hz significant reduction in the influence of ambient noise was observed, and future instruments were designed with a 1500 Hz fundamental mode (Arnott et al., 2005b). Therefore, a lower limit on operating frequency comes about in restricting the effects of instrument noise at resonance, as ambient noise sources are strong at low frequency.

The quality factor Q, or resonance enhancement, is the amplification factor or gain of the acoustic resonator. The Q is the ratio of energy stored in the resonator to acoustic energy dissipated per radian. It can be expressed as a sum of loss terms:

$$\frac{1}{Q} \equiv \frac{\text{Acoustic Energy Dissipated per Cycle}}{\text{Energy Stored}} = \frac{1}{Q_{transport}} + \frac{1}{Q_{loss}}, \qquad \text{(Eq. 1.5)}$$

where $Q_{transport}$ refers to losses associated with thermal conduction and viscosity. Q_{loss} accounts for all other fractional losses within the resonator such as losses due to microphone flexing, bulk acoustic losses within the air mixture, and other fluid dynamical motions of the air. The chief losses in the resonator are transport losses of thermal and viscous energy associated with fluid transport and interaction with resonator walls. Fluid kinetic energy is dissipated within the viscous boundary layer at the

resonator wall, and fluid potential energy is dissipated within the thermal boundary layer (Arnott et al., 2006).

When operating the photoacoustic instrument under conditions of high relative humidity (e.g. RH > 60%) or in measuring the light absorption of volatile aerosols, the mass transfer effects of evaporation and condensation must be taken into account. The photoacoustic signal is produced by heat transfer of particles that have absorbed radiation, but a signal can also be generated by mass transfer. For example, consider light absorption by a water droplet or by a soot particle that has experienced water uptake under high RH conditions. If the droplet or particle is illuminated by radiation at a wavelength of strong absorption by water the laser light will be absorbed. Not only will this absorbed radiation heat the particle, but some power will be transferred into latent heat causing evaporation to occur and add additional water vapor to the surrounding air. These additional water vapor molecules will contribute to the acoustic signal. An illustrative analogy is the reduction of photoacoustic signal observed when gaseous NO_2 is illuminated by radiation of high enough energy to photodissociate the molecules. In this case some energy will be absorbed by the NO_2 and transferred to the surrounding air, but some energy will go into NO_2 photodissociation, causing a reduction in the observed photoacoustic signal (Raspet et al., 2003).

A more general expression to obtain light absorption coefficient β_{abs} that includes mass transfer is

$$\beta_{abs} = \frac{P_m}{P_L}\frac{A_{res}\pi^2 f_o}{Q}\mathrm{Re}\left[\frac{e^{i(\varphi_M-\phi_L)}}{\tilde{S}}\right], \qquad \text{(Eq. 1.6)}$$

where the dimensionless complex photoacoustic source, $\hat{S}$, includes both mass transfer, m, and heat transfer, h, terms.

$$\tilde{S} = mc^2 + (\gamma - 1)h \text{ ,} \qquad \text{(Eq. 1.7)}$$

where

$$m = \frac{E}{1 - iT + LE} \text{ ,} \qquad \text{(Eq. 1.8)}$$

and

$$h = \frac{1}{1 - iT + LE} \text{ .} \qquad \text{(Eq. 1.9)}$$

L is the latent heat of vaporization for liquid water in Joules per kilogram (J/kg). E is a dimensionless term associated with evaporation and condensation

$$E = \frac{\rho_w \rho_o}{\rho_d} \frac{D}{\kappa T_o} \left(\frac{L m_w}{R T_o} - 1 \right), \qquad \text{(Eq. 1.10a)}$$

where ρ_w, ρ_d, and ρ_o are the density of water vapor, density of dry air, and total density of air with water vapor, respectively, in kilograms per meter cubed. The thermal conductivity of the sample is given by κ (W/m K), D is the mass diffusion coefficient (m^2/s), and m_w is the molecular weight of water vapor (kg/mole). R is the universal gas constant (J/mole K), and T_o is the ambient temperature (K). T is a dimensionless term associated with thermal relaxation: the period of time, τ, it takes for an illuminated particle to transfer absorbed heat to the surrounding air. T can be expressed as

$$T = \omega \frac{c_p \rho r^2}{3\kappa} \equiv \omega\tau \text{ ,} \qquad \text{(Eq. 1.10b)}$$

where $\omega = 2\pi f_o$ *is* the radian frequency in radians per second, c_p is the specific heat capacity of the particle (J/kg K), ρ is the particle density (kg/m^3), and r is particle radius

(m). Therefore, the photoacoustic source term for absorption by a volatile particle can be expressed

$$\tilde{S} = \frac{Ec^2 + (\gamma - 1)}{1 - iT + LE}. \qquad \text{(Eq. 1.11)}$$

When mass transfer can be neglected, that is no evaporation or condensation occurs, E goes to zero and the source term reduces to $\hat{S}_{dry}$:

$$\tilde{S}_{dry} = \frac{(\gamma - 1)}{1 - iT}. \qquad \text{(Eq. 1.12)}$$

The source term generally used in calculating β_{abs} in Equation 1.6 is $S = \hat{S}_{dry}$, with $T = 0$, as in Equation 1.1. Assuming $T \rightarrow 0$ implies that the heat transfer time of the particle is much less than the acoustic period of resonant operation. A non-zero value of T would be apparent in operation as a phase shift between the oscillating power of the laser beam and the microphone signal. A phase difference has not been detectable in reported photoacoustic measurements (Arnott et al., 2003).

1.5 Acoustic Response under Changing Pressure Conditions

Empirical evaluation of photoacoustic instrument response under rapidly changing environmental conditions was conducted in the laboratory in order to test absorption theory and use of the instrument aloft, as in aircraft measurement. In particular, the effect on noise, acoustic response and absorption signal by changing ambient pressure conditions was assessed. The laboratory evaluations of noise, resonance frequency, and quality factor confirmed theoretical understanding of the acoustic response as a function of pressure.

In order to evaluate the contribution to acoustic noise by changing pressure conditions, the ambient pressure within the photoacoustic resonator was pumped down to below 300 mb. The instrument was then completely sealed and allowed to slowly come back to ambient pressure due to some small leak in the system. No pump was attached to the instrument, and the laser power was artificially set at 200 mW to test the acoustic response. The noise level within the resonator was found to remain constant under changing pressure conditions, as can be seen in Figure 1.4 which presents the acoustic noise as a function of air sample pressure within the resonator.

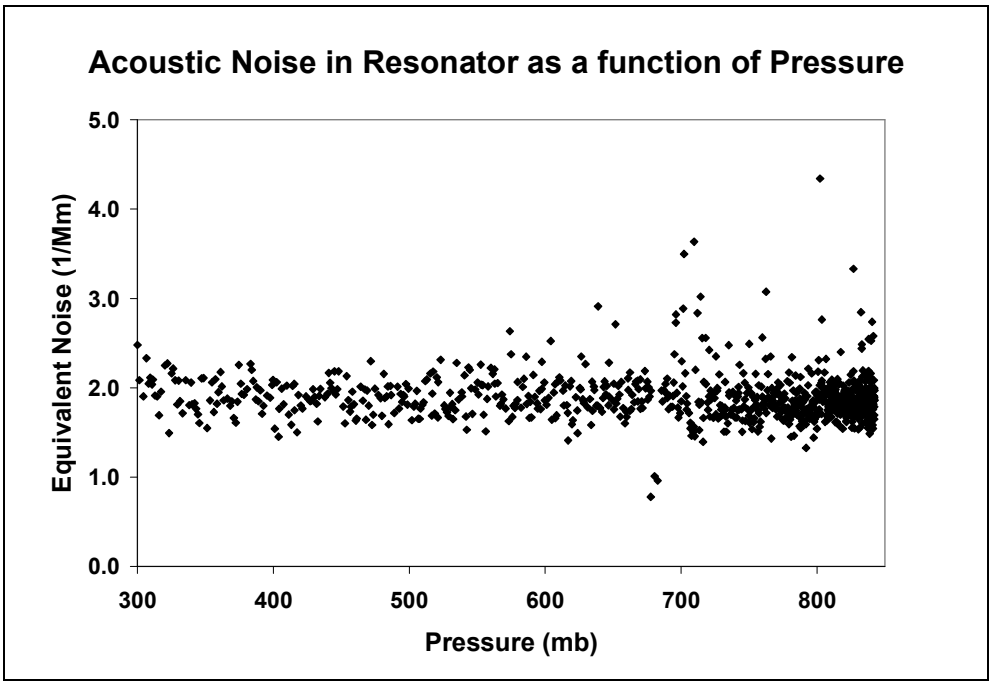

Figure 1.4 Acoustic noise within the resonator under conditions of changing pressure.

Although variation in the range of measured values increases slightly for pressures above 600 mb, the noise level remained relatively constant at around 2 Mm^{-1}. Acoustic noise produced by the instrument is not expected to be a function of pressure.

The theoretical value of the resonator quality factor in Equation 1.5 with an expanded definition of the inverse of $Q_{transport}$ can be expressed as

$$\frac{1}{Q} = \frac{1}{Q_{transport}} + \frac{1}{Q_{loss}}$$

$$= \frac{\delta_\eta}{r} + (\gamma - 1)\delta_T\left(\frac{2}{L} + \frac{1}{r}\right) + \frac{1}{Q_{loss}}, \qquad \text{(Eq. 1.13)}$$

where

$$\delta_\eta = \sqrt{\frac{\eta}{\rho \pi f_o}}, \text{ and} \qquad \delta_T = \sqrt{\frac{\kappa}{c_p \rho \pi f_o}} = \frac{\delta_\eta}{\sqrt{N_{pr}}} \qquad \text{(Eq. 1.14)}$$

represent the thermal and boundary layer thicknesses, respectively, where acoustic boundary losses occur. The resonator radius r is 0.838 cm and the resonator length L is 24.86 cm. In Equation 1.14 η is the viscosity of moist air, κ is the thermal conductivity, c_p is the isobaric heat capacity per unit mass, and $N_{pr} = \eta\, c_{p/}\, \kappa$ is the dimensionless Prandtl number. The Prandtl number of dry air at standard conditions is approximately 0.7. The density of moist air is given by

$$\rho = \frac{P(mb)}{RT}\left(2.9 - 1.1h\right), \qquad \text{(Eq. 1.15)}$$

where h represents the fraction of water vapor molecules,

$$h = \frac{RH(\%)}{100}\frac{e(T)}{P}, \qquad \text{(Eq. 1.16)}$$

and $e(T)$ is the saturation vapor pressure of water vapor as a function of temperature,

$$e(T) = 6.11(mb)\exp\left[\frac{a\left(T - T_o\right)}{T - b}\right]. \qquad \text{(Eq. 1.17)}$$

The constant values in Equation 1.17 are taken to be $a = 17.269$, $b = 35.860$ and $T_o = 273.15$ for $T > 273.15$ K (Arnott et al., 2006).

Neglecting the small term in Equation 1.13 associated with resonator length, the resonator quality factor associated with transport losses can be expressed in terms of constant and measured values:

$$Q_{transport} = \sqrt{\frac{\pi f_o (2.9 - 1.1h) P(mb)}{RT\eta}} r \frac{\sqrt{N_{pr}}}{\sqrt{N_{pr}} + (\gamma - 1)}. \qquad \text{(Eq. 1.18)}$$

Therefore, primary variations of the resonator quality factor associated with transport losses scales as the square root of ambient pressure:

$$Q_{transport} \sim \sqrt{P}, \text{ or } \quad Q_{transport} = \alpha\sqrt{P} \qquad \text{(Eq. 1.19)}$$

where

$$\alpha = \sqrt{\frac{\pi f_o (2.9 - 1.1h)}{RT\eta}} r \frac{\sqrt{N_{pr}}}{\sqrt{N_{pr}} + (\gamma - 1)}. \qquad \text{(Eq. 1.20)}$$

Assuming the following constant values,

$\eta = 1.73\times10^{-5}$ kg m^{-1} s^{-1}, viscosity of moist air
$r = 0.838$ cm, resonator radius
$R = 8.3143$ J deg^{-1} mole^{-1}, universal gas constant
$N_{pr} = \eta c_p/\kappa \approx 0.7$, Prandtl number

as well the following values composed of measured quantities

h, fraction of water vapor molecules
$\gamma = (7+h)/(5+h)$, ratio of isobaric and isochoric heats
T, temperature in Kelvin
f_o, resonance frequency in Hertz

an approximate value for the proportionality constant is $\alpha = 3.23$. The resonator quality factor can then be expressed as

$$\frac{1}{Q} = \frac{1}{\alpha\sqrt{P}} + \frac{1}{Q_{loss}}. \qquad \text{(Eq. 1.21)}$$

The inferred value associated with additional resonator losses is Q_{loss} = 300 (Arnott et al., 2006).

The photoacoustic instrument was run with laser power artificially set to 200 mW to test acoustic performance, and the pressure conditions inside the resonator were allowed to vary. Figure 1.5 presents the inverse of the empirical quality factor versus the inverse of the square root of measured pressure. According to the theoretical expression for the resonator quality factor (Equation 1.21) the slope of the plotted line is equal to the inverse of the previously derived constant, α, and the y-intercept is equal to the inverse of the resonator quality factor associated with other losses, Q_{loss}. The red line in Figure 1.5 represents a linear fit of the $1/Q$ versus $1/\sqrt{P}$ data. The R value, or correlation coefficient for the linear fit, is 0.98. Parameters for slope and y-intercept of the linear fit produce the following values for α and Q_{loss}: α = 3.38 and Q_{loss} = 290. The thin black line is the theoretically expected plot of Equation 1.21 including the estimated values of α = 3.23 and Q_{loss} = 300.

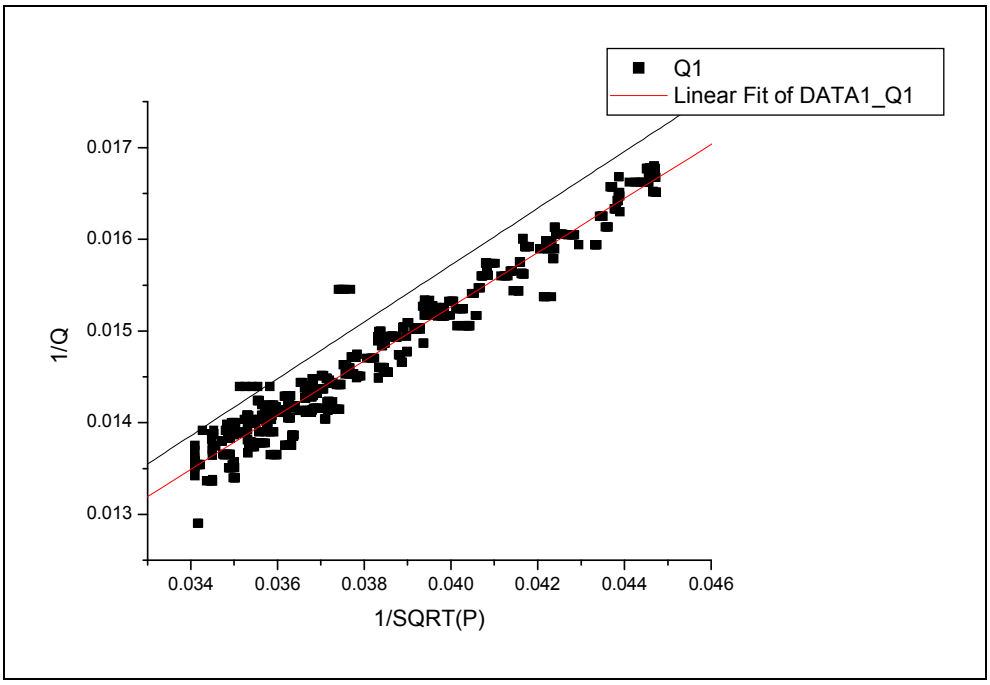

Figure 1.5 Plot of empirical and theoretical values of the inverse of resonator quality factor as a function of the inverse of the square root of resonator pressure

The results of laboratory analysis of resonator quality factor as a function of pressure indicate a reasonable and predictable relationship between the two values. The square root dependence on pressure makes the time reasonable between Q determinations on spiral ascents and descents in aircraft use.

Acoustic boundary layer losses within the resonator also affect the resonance frequency. In a perfectly lossless resonator the resonance frequency would be equal to the speed of sound divided by resonator length: $f_o = c/L$. In practice, however the resonance frequency is also a function of the resonator quality factor associated with transport losses

$$f_o = \frac{c}{L}\left[1 - \frac{1}{2Q_{transport}}\right]. \qquad \text{(Eq. 1.22)}$$

The primary variation of the resonator quality factor scales as the square root of the ambient pressure, represented in Equation 1.19, where the value of constant alpha is α = 3.23 (Arnott et al., 2006). It follows that pressure can be expressed as a function of resonance frequency:

$$\frac{1}{\sqrt{P}} = \frac{-2\alpha L}{c} f_o + 2\alpha \, . \qquad \text{(Eq. 1.23)}$$

The speed of sound in dry air is c = 343 m/s, and the resonator length is L = 0.2486 m. The form of this expression suggests the relationship between $P^{-1/2}$ and f_o.

Results from the laboratory test of acoustic resonance frequency response as measured under changing pressure conditions are shown in Figure 1.6. This figure depicts the inverse of the square root of pressure as a function of corresponding resonance frequency values. The line is a linear fit of the data, with correlation coefficient of R = -0.95.

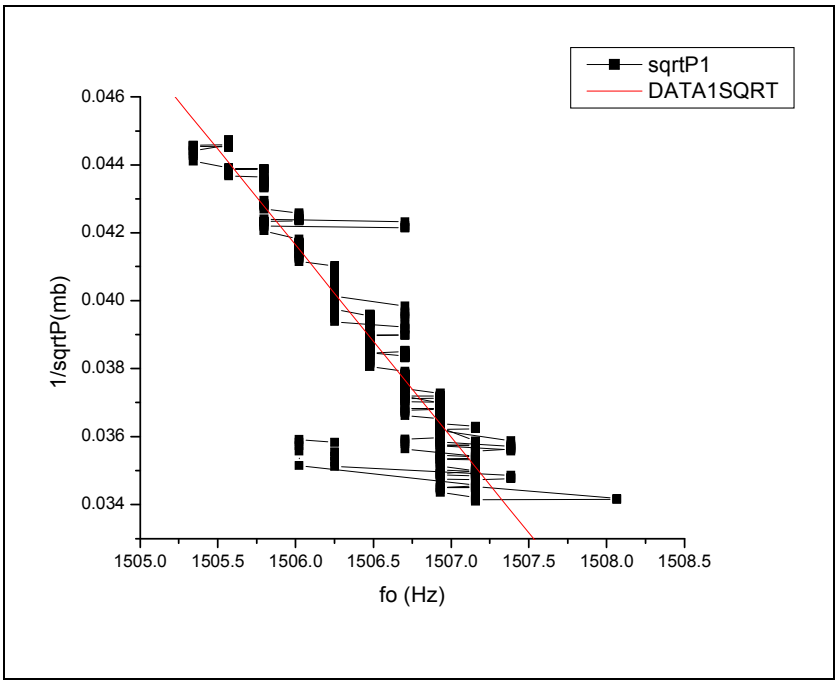

Figure 1.6 The inverse of the square root of ambient pressure as a function of resonance frequency, including linear fit

The linear fit values found for slope and y-intercept correspond reasonably well to the theoretically expected values, as shown in Table 1.1. This analysis confirms the functional form of the P, f_o relationship.

	Theoretical values	Derived values
Slope	$\frac{-2\alpha L}{c} = -0.00424$	-0.0056
Intercept	$2\alpha = 6.46$	8.54

Table 1.1 The theoretical linear parameters expected from Equation 1.23 and those parameters derived from a linear fit of the empirical data in Figure 1.6

Results from the empirical assessment of the change in values used to determine photoacoustic absorption, particularly resonance quality factor and resonance frequency, as a function of changing pressure are consistent with theoretical expectations. The

acoustic response of the resonator is not expected to be negatively affected by rapidly changing ambient pressure conditions, allowing for employment of the photoacoustic instrument aboard meteorological aircraft used to sample the vertical distribution of aerosol.

1.6 Photoacoustic Instrument Noise

The photoacoustic instrument conveniently provides a measurement of noise along with every measurement of aerosol light absorption. There are numerous sources of noise within the instrument, as well as external or environmental sources. Acoustic noise is resonance enhanced along with the absorption signal, and noise is also produced and amplified by electronic components downstream of the resonator. However, because the noise is random in phase it can largely be separated from the signal. A technique is presented in this section for assessing the noise signal at a range of frequencies off resonance. Noise can then be averaged across a broad frequency range to allow for determination of the noise level as if it were measured at the resonance frequency.

Noise arises from a variety of sources. The effects of some can be limited by filters, instrument operation, and design, such as employment of a critical orifice described previously. Other noise sources are inherent to operation, such as those which arise from electronic components of the instrument. Noise can be separated into two broad categories: acoustic noise and electrical noise.

Electrical noise is broadly used here to describe all noise sources that develop not from sound or mechanical vibration, but because the measured signal is actually electrical in nature. Instrument operation is such that the thermal energy that causes a pressure

fluctuation is converted into a measurable form, an electrical voltage, and the resulting movement of electrons adds random noise to the signal. Every component of the instrument produces both signal and noise. Charge fluctuation on the surface of the microphone induces electrical noise. The microphone preamplifier as well as the programmable preamplifier are noise sources which amplify both the signal and noise. The user interface of the instrument, the computer, is another electrical noise source. Other examples of intrinsic noise sources within the electronic instrument components include 'Johnson noise', which arises from fluctuations of electron density in a resistor as a function of temperature, and '1/f noise' arising from resistance fluctuations in a resistor that is carrying current.

Acoustic noise can come from any sound source within the instrument environment. It can also stem from vibrational motion of the instrument, such as mechanical to acoustical conversion producing vibrations in the resonator walls. Acoustic noise will be in the form of pressure fluctuations within the resonator. Therefore, just like the light absorption signal, acoustic noise will be resonance enhanced. Noise near the resonance frequency or fundamental modes of the resonator cavity will be acoustically amplified.

Acoustic noise provides the fundamental noise limit of the photoacoustic instrument. When the instrument is operated without the laser, so that no light absorption signal is produced, the remaining noise signal amplitude appears in the frequency domain as a (noisy) curve that peaks at the resonance frequency. That is, the limiting noise signal is resonance enhanced and, therefore, derives from the acoustic field of the resonator.

The primary hope regarding the instrument's noise signal is that noise is random and incoherent and is not due to a stray cricket that has burrowed into the instrument, or any other more mundane source like electronic pickup of the drive frequency. That is, the noise shows no consistent phase over time. Acoustic noise will fall within the measured frequency bandwidth centered on f_o. However, because the noise does not stem from a coherent source phase sensitive detection allows for its separation from the light absorption signal. In addition, although the acoustic noise is resonance enhanced along with the signal, its incoherence results in enhancement that scales as $Q^{1/2}$ while the signal is enhanced at resonance by Q. The signal to noise ratio is proportional to the square root of the quality factor, or SNR ~ $Q^{1/2}$ (Arnott et al., 1995).

The noise calculation by the photoacoustic instrument proceeds by first considering the complex magnitude of the microphone signal in the frequency domain at all points other than resonance. Pressure fluctuations measured by the microphone that are not at resonance frequency are not light absorption signal and, therefore, are noise. Acoustic pressure in the cavity near resonance has a well known frequency dependence modeled as a Lorentzian curve. Assuming resonance enhancement, the complex dependence of acoustic pressure on frequency is given by

$$\tilde{P}_m(f) = \frac{P_o}{\frac{2Q(f - f_o)}{f_o} + i}, \qquad \text{(Eq. 1.24)}$$

where the peak pressure at resonance is represented by P_o. A transfer function, $G(f - f_o)$, is constructed from the ratio of Equation 1.24 at resonance to the same function at frequency f:

$$G(f-f_o) \equiv \frac{P(f_o)}{P(f)} = 1 - i\frac{2Q(f-f_o)}{f_o}. \qquad \text{(Eq. 1.25)}$$

The product of $G(f - f_o)$ and acoustic pressure at some frequency f transfers the acoustic pressure measurement to the value it would have at f_o. Employing the transfer function $G(f - f_o)$, the complex microphone signal off resonance can be transferred and evaluated as if it were at resonance. Excluding a frequency bandwidth centered on resonance, the microphone signal at all frequencies is transferred and measured in this manner, and then all measurements are averaged to provide the equivalent acoustic noise signal at resonance frequency.

The expression for the noise equivalent light absorption measurement is

$$\beta_{abs}^{Noise} = \frac{A_{res}\pi^2 f_o}{P_L(\gamma-1)Q}\sum_{j=1}^{N}\frac{G(f_j-f_o)P_m(f_j)}{N}, \quad (f_j \neq f_o). \qquad \text{(Eq. 1.26)}$$

In Equation 1.26 the sum is over all values of frequency f_j that lie within the bandwidth of resonance, $\Delta f = f_o/Q$. However, the sum does not include the value $f_j = f_o$, as this is the signal. Equation 1.26 was obtained from application of the simple photoacoustic equation, Equation 1.1.

An example of an idealized measured microphone signal magnitude in the frequency domain, including signal and noise, is presented in Figure 1.7 to illustrate the equivalent noise calculation method.

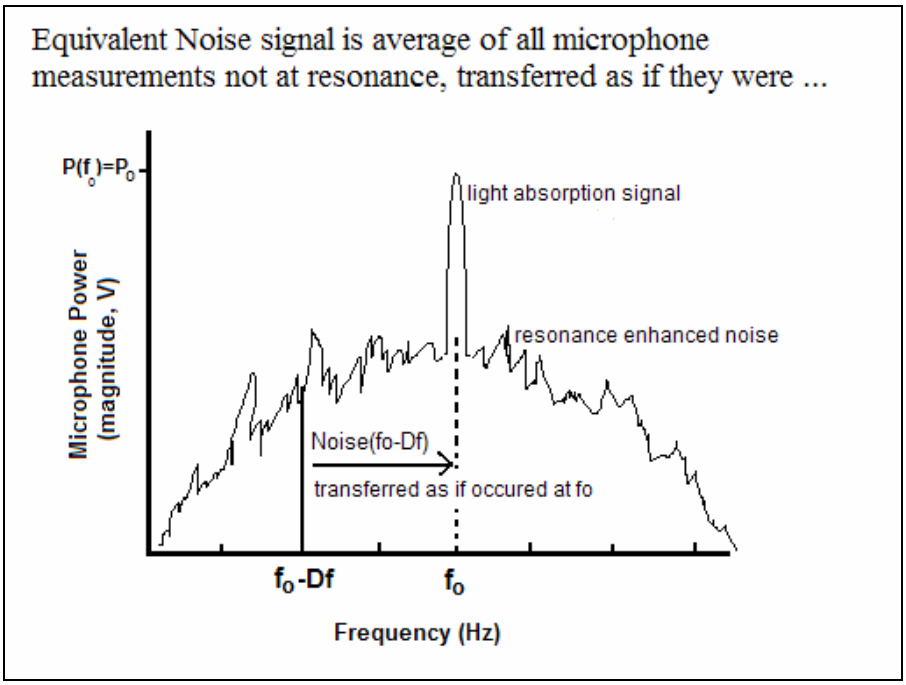

Figure 1.7 Idealized illustration of microphone power magnitude as a function of frequency, including both signal and noise

Referring to Figure 1.7, the signal is obtained from the measurement at f_o. The noise is computed from the frequency response-weighted average pressure within the bandwidth of the resonance. The ability to make a measurement of noise along with signal is a powerful property of the photoacoustic instrument.

An example of a controllable source of acoustic noise is the sample flow rate through the system. It is advantageous to maximize flow rate, especially if the photoacoustic instrument is being operated in a rapidly changing environment, such as on an aircraft. However, enhanced noise provides an operational flow rate limit. In a laboratory test of acoustic noise induced by flow rate the critical orifice was removed from a photoacoustic instrument so that flow rate could be manually adjusted with a flow restrictor on the pump line. A flow meter was put on the sample line upstream of the resonator. Starting from zero flow, flow rate was gradually increased in small increments

and the noise level in the instrument was recorded at each stage. As can be seen in Figure 1.8, the acoustic noise level was found to be constant with flow rate up until a certain critical rate was reached, at which point the noise increased sharply with increasing flow. The sudden increase is likely due to the generation of fluid vortices at junctions in the sample flow path. Figure 1.8 is a plot of acoustic noise as a function of volumetric flow rate.

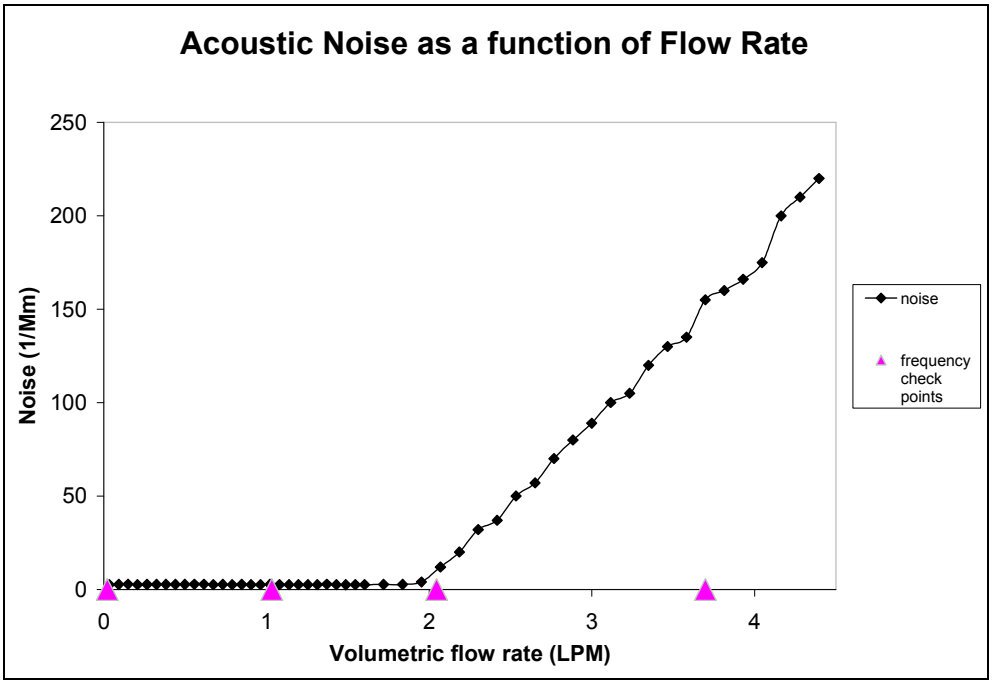

Figure 1.8 Rapidly increasing acoustic noise above a critical rate of 1.85 liters per minute provides a limit on sample flow rate through the instrument. The frequency dependence of noise was further analyzed at the indicated frequency check points

The results in Figure 1.8 indicate that the volumetric flow rate limit for acceptable measurement conditions of acoustic noise equal to roughly 2.65 Mm^{-1} is approximately 1.85 LPM.

At the flow rates indicated on Figure 1.8 by triangles the measured acoustic noise was analyzed according to frequency composition using an HP 35665A dynamic signal

analyzer. The flow rates investigated were zero flow, 1.0, 2.0 and 3.7 liters per minute. The magnitude of the noise was measured as a function of frequency, and compared at the different flow rates. The noise magnitude in volts was divided by the applied gain to properly scale each value for purposes of comparison. Figure 1.9 contains the magnitude of noise converted to standard pressure level units (dB Re 20 µPa) as a function of frequency for each flow rate. The frequency structure of the noise is modal, corresponding to acoustic modes of the instrument, with the magnitude of each mode increasing as the flow rate surpasses the critical noise-limiting point.

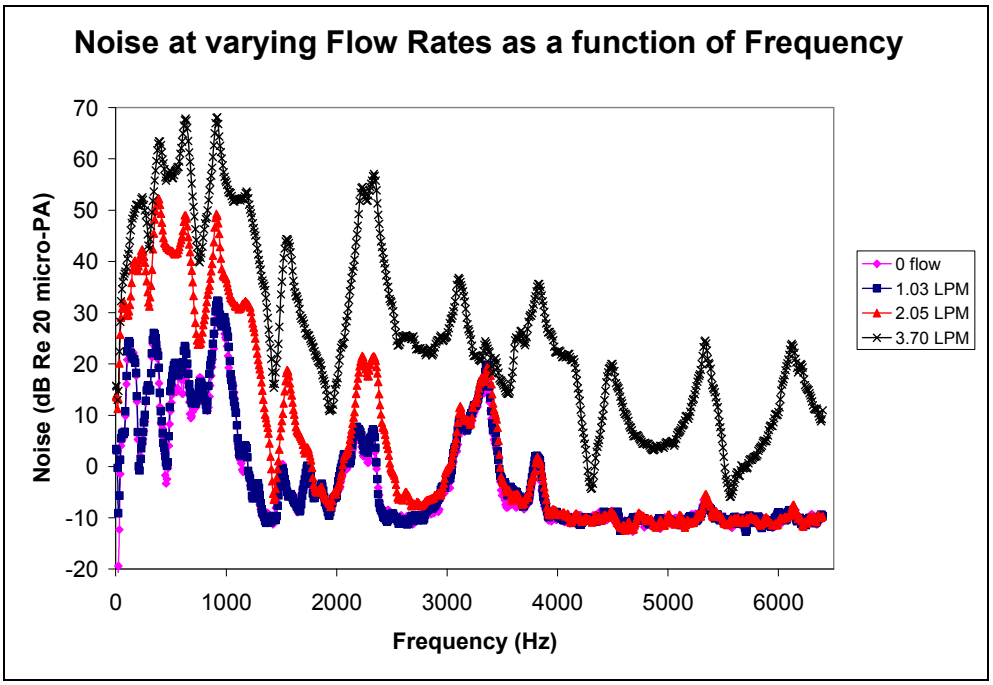

Figure 1.9 Frequency composition of acoustic noise produced by increasing flow rate indicates modal structure and resonance enhancement of noise signal

A log plot of the ratio of noise magnitude in volts at each of the non-zero flow rates to the reference noise magnitude at zero flow rate, plotted as a function of frequency is depicted in Figure 1.10.

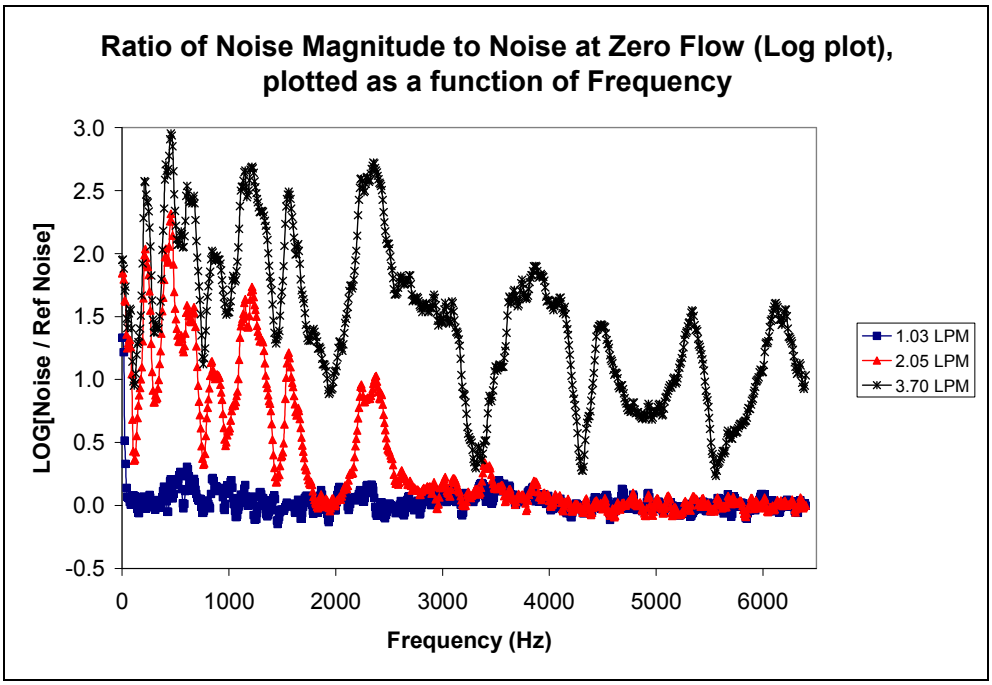

Figure 1.10 Log of the ratio of noise to reference noise at zero flow rate as a function of frequency

Figure 1.10 portrays the scale of increase in noise magnitude at each frequency mode compared to zero flow. The noise level sharply increases, particularly at resonator modes, for flow above the critical rate. Recall that the instrument generally operates at a flow rate of 1 LPM, depicted in blue in Figure 1.9 and Figure 1.10. Figures 1.9 and 1.10 reveal the resonance enhancement of acoustic noise.

1.7 Scattering Measurement

Light scattering by aerosols is measured in the photoacoustic instrument by the method of reciprocal nephelometry. "Reciprocal" refers to the fact that the light source and detector are reversed from the arrangement described previously in the more commonly employed TSI integrating nephelometer. In a reciprocal integrating nephelometer arrangement a parallel beam of light is used to illuminate a scattering

volume, and scattered light is detected by a cosine-weighted detector so that the measured voltage is proportional to the total scattering cross section. Within the instrument the laser beam provides the parallel light source and the cosine-weighted detector is positioned on the resonator to view the center of the sample cavity. The cosine-weighted sensor is fiber coupled to a photomultiplier tube (PMT).

The coefficient of scattering, β_{sca}, is calculated using the magnitude of the Fourier transformed functions of PMT signal and laser power at resonance frequency. The expression for determining β_{sca} is given by

$$\beta_{sca} = \alpha \frac{\left| \tilde{P}_{PMT} \right|}{\left| \tilde{P}_{L} \right|} , \qquad \text{(Eq. 1.27)}$$

where α is a calibration factor determined during instrument calibration. The photomultiplier tube signal is given by $P_{PMT,}$ and P_L is the measured laser power. The magnitudes of these two complex functions of frequency are used in Equation 1.27. Background measurements of scattering are also made periodically during instrument operation of light scattering by filtered (sample-free) air within the resonator. The scattering background is subtracted from the PMT signal to produce the reported coefficient of scattering.

Instrument design minimizes some of the non-idealities typical of common integrating nephelometers which introduce errors into the scattering measurement. The narrow spectral width of the diode laser of a fraction of nanometer reduces the effect of imperfect wavelength response. In addition, angular non-idealities introduced by the scattering detection truncation angle, which reduces full 4π angular integration to a range

excluding near-forward and near-backward scattering, are reduced in the reciprocal integrating nephelometer design. Existing integrating nephelometers usually integrate over scattering angles ranging from 7^o to 170^o. A larger angular range of 4^o to 176^o exists in the reciprocal nephelometer employed on the instrument. The 4^o to 176^o angular range was confirmed by evaluation of the cosine response of the light sensor conducted by Abu-Rahmah et al. (2006).

Ideal cosine response would be achieved by a two-dimensional aperture, for which the detected light flux is proportional to the product of incident light intensity and the cosine of the angle between scattering direction and detector surface normal, φ. The flux entering a real finite aperture is no longer simply proportional to the projected area due to reflection and diffraction effects, and so it is not proportional to $cos\varphi$. In practice this is compensated for by the use of a physical cosine corrector along with a photomultiplier tube as the light sensing element. The cosine corrector is placed in front of the PMT and consists of a thin disc of Teflon: a highly scattering material that diffuses incoming light and gives a near-cosine response (Abu-Rahmah, Arnott, and Moosmüller, 2006).

Some disadvantages in measurement of aerosol light scattering are imposed by instrument design. Scattering background measurements are often significantly higher in the photoacoustic/reciprocal nephelometer design than other integrating nephelometers due to trade offs in cell length for instrument compactness. With high background scattering low levels of aerosol scattering cannot be measured with high accuracy, though measurements are satisfactory for the smoke plumes discussed in Chapter 4 of this dissertation. Wall scattering from the sample cavity windows to the light sensor head

decreases with increased cell length. The resonator cell length of the photoacoustic instrument is just under 25 cm, whereas the cell length of the TSI Model 3563 integrating nephelometer is over 100 cm. Improvement to scattering measurements by the instrument could be accomplished by distancing the cell windows from the scattering volume, though at a price of increased instrument size. It is also postulated that use of a multimode optical fiber coupling the cosine sensor and PMT results in additional variation in scattering measurements. Light transmission by the multimode fiber is sensitive to fiber stress and temperature as well as where in the fiber cross-section scattered light enters, resulting in measurement deviations. To test this hypothesis the optical fiber will be removed in future instruments so that the PMT will be connected directly to the scattering sensor head.

1.8 References

Abu-Rahmah, A., Arnott, W. P., and Moosmüller, H. (2006). Integrating nephelometer with a low truncation angle and an extended calibration scheme. *Measurement Science and Technology* **17**(7)**,** 1723-1732.

Anderson, T. L., Covert, D. S., Marshall, S. F., Laucks, M. L., Charlson, R. J., Waggoner, A. P., Ogren, J. A., Caldow, R., Holm, R. L., Quant, F. R., Sem, G. J., Wiedensohler, A., Ahlquist, N. A., and Bates, T. S. (1996). Performance characteristics of a high sensitivity, three wavelength, total scatter/backscatter nephelometer. *Journal of Atmospheric and Oceanic Technology* **13,** 967-986.

Anderson, T. L., and Ogren, J. A. (1998). Determining Aerosol Radiative Properties Using the TSI 3563 Integrating Nephelometer. *Aerosol Science and Technology* **29**(1)**,** 57-69.

Andreae, M. O. (2001). The dark side of aerosols. *Nature* **409,** 671-672.

Andreae, M. O., and Gelencser, A. (2006). Black carbon or brown carbon? The nature of light-absorbing carbonaceous aerosols. *Atmospheric Chemistry and Physics Discussions* **6**(3)**,** 3419-3463.

Arnott, W. P., Hamasha, K., Moosmüller, H., Sheridan, P. J., and Ogren, J. A. (2005a). Towards aerosol light absorption measurements with a 7-wavelength Aethalometer: Evaluation with a photoacoustic instrument and a 3 wavelength nephelometer. *Aerosol Science & Technology* **39,** 17-29.

Arnott, W. P., Moosmüller, H., Abbott, R. E., and Ossofsky, M. D. (1995). Thermoacoustic Enhancement of Photoacoustic Spectroscopy: Theory and Measurements of the Signal to Noise Ratio. *Review of Scientific Instruments* **66**(10)**,** 4827-4833.

Arnott, W. P., Moosmüller, H., Rogers, C. F., Jin, T., and Bruch, R. (1999). Photoacoustic spectrometer for measuring light absorption by aerosols: Instrument description. *Atmospheric Environment* **33,** 2845-2852.

Arnott, W. P., Moosmüller, H., Sheridan, P. J., Ogren, J. A., Raspet, R., Slaton, W. V., Hand, J. L., Kreidenweis, S. M., and Collett, J. L. (2003). Photoacoustic and filter-based ambient aerosol light absorption measurements: Instrument comparisons and the role of relative humidity. *Journal of Geophysical Research* **D1,** 4034.

Arnott, W. P., Moosmüller, H., and Walker, J. W. (2000). Nitrogen dioxide and kerosene-flame soot calibration of photoacoustic instruments for measurement of light absorption by aerosols. *Review of Scientific Instruments* **71**(7)**,** 4545-4552.

Arnott, W. P., Walker, J. W., Moosmüller, H., Elleman, R. A., Jonsson, H. H., Buzorius, G., Conant, W. C., Flangan, R. C., and Seinfeld, J. H. (2006). Photoacoustic Insight for aerosol light absorption aloft from meteorological aircraft and comparison with particle soot absorption photometer measurements: DOE Southern Great Plains climate research facility and coastal stratocumulus imposed perturbation experiments. *Journal of Geophysical Research* **111**(D5)**,** 1-16.

Arnott, W. P., Zielinska, B., Rogers, C. F., Sagebiel, J., Park, K., Chow, J., Moosmüller, H., and Watson, J. G. (2005b). Evaluation of 1047-nm Photoacoustic Instruments and Photoelectric Aerosol Sensors in Source-Sampling of Black Carbon Aerosol and Particle-Bound PAHs from Gasoline and Diesel Powered Vehicles. *Environmental Science & Technology* **39**(14)**,** 5398-406.

Bond, T. C., Anderson, T. L., and Campbell, D. (1999). Calibration and Intercomparison of Filter-Based Measurements of Visible Light Absorption by Aerosols. *Aerosol Science and Technology* **30**(6)**,** 582-600.

Bond, T. C., and Bergstrom, R. W. (2006). Light Absorption by Carbonaceous Particles: An Investigative Review. *Aerosol Science and Technology* **40**(1)**,** 27-67.

Chan, C. H. (1975). Effective absorption for thermal blooming due to aerosols. *Applied Physics Letters* **26,** 628-629.

Charlson, R. J., Schwartz, S. E., Hales, J. M., Cess, R. D., Coakley, J. A., Hansen, J. E., and Hofmann, D. J. (1992). Climate Forcing by Anthropogenic Aerosols. *Science* **255**(5043)**,** 423-429.

Hansen, A. D. A., Rosen, H., and Novakov, T. (1984). The Aethalometer - An Instrument for the Real-Time Measurement of Optical Absorption by Aerosol Particles. *Science of the Total Environment* **36,** 191-196.

Horvath, H. (1993). Atmospheric Light Absorption - A Review. *Atmospheric Environment* **27A**(3)**,** 293-317.

Jacobson, M. Z. (2001). Strong Radiative Heating due to the Mixing State of Black Carbon in Atmospheric Aerosols. *Nature* **409**(6821)**,** 695-697.

Kirchstetter, T. W., Novakov, T., and Hobbs, P. V. (2004). Evidence that the spectral dependence of light absorption by aerosols is affected by organic carbon. *Journal of Geophysical Research* **109**(D21209)**,** doi:10.1029/2004JD00499.

Lohmann, U., and Feichter, J. (2005). Global indirect aerosol effects: a review *Atmospheric Chemistry and Physics* **5**(3)**,** 715-737.

Malm, W. C., Sisler, J. F., Huffman, D., Eldred, R. A., and Cahill, T. A. (1994). Spatial and seasonal trends in particle concentration and optical extinction in the United States. *Journal of Geophysical Research* **99**(D1)**,** 1347-1370.

Moosmuller, H., and Arnott, W. P. (2003). Angular truncation errors in integrating nephelometry. *Review of scientific instruments* **74**(7)**,** 10.

Petzold, A., Schloesser, H., Sheridan, P. J., Arnott, W. P., Ogren, J. A., and Virkkula, A. (2005). Evaluation of multi-angle absorption photometry for measuring aerosol light absorption. *Aerosol Science & Technology* **39,** 40-51.

Petzold, A., and Schönlinner, M. (2004). Multi-angle absorption photometry - a new method for the measurement of aerosol light absorption and atmospheric black carbon. *Journal of Aerosol Science* **35,** 421-441.

Raspet, R., Slaton, W. V., Arnott, W. P., and Moosmüller, H. (2003). Evaporation-Condensation Effects on Resonant Photoacoustics of Volatile Aerosols. *Journal of Atmospheric and Oceanic Technology* **20**(5)**,** 685-695.

Sheridan, P. J., Arnott, W. P., Ogren, J. A., Anderson, B. E., Atkinson, D. B., Covert, D. S., Moosmuller, H., Petzold, A., Schmid, B., Strawa, A. W., Varma, R., and Virkkula, A. (2005). The Reno aerosol optics study: An Evaluation of Aerosol Absorption
Measurement Methods. *Aerosol Science & Technology* **39,** 1-16.

Virkkula, A., Ahlquist, N. C., Covert, D. S., Arnott, W. P., Sheridan, P. J., Quinn, P. K., and Coffman, D. J. (2005). Modification, calibration and a field test of an instrument for measuring light absorption by particles. *Aerosol Science and Technology* **39,** 68-83.

Weingartner, E., Saathoff, H., Schnaiter, M., Streit, N., Bitnar, B., and Baltensperger, U. (2003). Absorption of light by soot particles: determination of the absorption coefficient by means of aethalometers. *Journal of Aerosol Science* **34,** 1445-1463.

2 Dual-Wavelength Photoacoustic Instrumentation

2.1 Introduction

In Chapter 1 the photoacoustic instrument was described in detail. In this chapter, a novel version of the same instrument which operates simultaneously at two wavelengths will be discussed. The dual-wavelength photoacoustic instrument employs two power-modulated lasers so that light absorption and scattering measurements are simultaneously made on a single aerosol sample at wavelengths of 405 nm and 870 nm. Information provided regarding the instrument will include details on dual laser direction and alignment into the resonator sample cavity, an instrument schematic, and discussion of acoustic considerations for measurement of two separate signals within the resonator.

Measurement of light absorption and scattering at more than one wavelength is useful in determining numerous aerosol properties including particle size, composition, and spectral response. The wavelength dependence of aerosol light scattering provides an indication of particle size. Properties of light scattering, such as the angular distribution of scattered light, are dependent on the scattering size parameter, x. The scattering size parameter is defined as

$$x = \frac{\pi D}{\lambda}, \qquad \text{(Eq. 2.1)}$$

where D is the particle diameter and λ is wavelength. Scattering by particles of size on the order of the radiation wavelength is dependent on this size parameter, and, therefore, dependent on wavelength. Particles much larger than the incident wavelength, however, will not exhibit this strong wavelength dependence. Light scattering measurements by the dual-wavelength photoacoustic instrument provide insight into the size of aerosol

particles in this manner, and allow differentiation between course mode (large) and fine mode (small) particles (Anderson et al., 1996).

Measurement of light absorption at two wavelengths provides much insight into the composition of the aerosol sample. The primary light absorbing species in the atmosphere is black carbon which, as mentioned in the Chapter 1, is expected to strongly absorb across a broad spectral range such that light absorption is inversely proportional to wavelength. Light absorption at wavelengths ranging from the near-ultraviolet to the infrared will respond in this predictable manner to carbonaceous particles of black or elemental nature. However, it has been shown that organic carbon aerosol also absorbs light, with much stronger absorption in the ultraviolet (UV) (Kirchstetter, Novakov, and Hobbs, 2004). Therefore, measurements at near-UV wavelengths respond not only to the elemental carbon nature of the sample but also to the presence of organic carbon species, both from primary and secondary sources.

The ability for simultaneous measurement also makes the instrument very valuable in applications with relatively short sampling times, and aides in instrument calibration. Because all scattering and absorption measurements are made in a single instrument there is no need to divert sample flow between two instruments operating at different wavelengths, or align two instruments serially and contend with particle loss. The advantages of simultaneous measurement within a single instrument are particularly important in aerosol plume detection, which is characterized by short detection times on the order of seconds to minutes.

Instrument calibration is constrained by having light absorption measurements at two wavelengths within a single instrument. The microphone is a common detector for

the absorption measurement at each wavelength. Unlike the photodiode, which measures laser power, the microphone has no spectral sensitivity. Therefore, while the photodiode must be calibrated separately at each wavelength, the wavelength-independent microphone calibration needs only to be conducted once at a single wavelength. This is in contrast to consideration of two photoacoustic instruments, each with a photodiode and a microphone to calibrate, or to the spectrally sensitive photomultiplier tube which also must be calibrated at both wavelengths. In summary, calibration of the absorption measurement on the dual-wavelength photoacoustic instrument is limited to a single microphone calibration and, therefore, is simpler and less error inducing than additional component calibrations at additional wavelengths.

Operation at the visible (near-UV) wavelength of 405 nm provides the option of measurement of absorption by nitrogen dioxide gas. NO_2 is an important gas in atmospheric chemistry, particularly in determination of the planet's ozone distribution, and one of the U.S. Environmental Protection Agency's "criteria" pollutants (Crutzen, 1979). If measurement of absorption by NO_2 is not desired, the gas can be removed by a denuder on the sample line upstream of the resonator. It can also be background-subtracted from the absorption signal since NO_2 is not removed by the filter during the instrument's background level assessment. Measurement of absorption by NO_2 can be used as a calibration method for the photoacoustic signal as well (Arnott, Moosmüller, and Walker, 2000). For sufficiently high concentrations of NO_2, extinction, measured from reduced gas transmissivity, is large enough that Rayleigh scattering by the gas molecules can be ignored. Arnott et al. (2000) used high concentrations of NO_2 gas during calibration of a 532 nm single-wavelength photoacoustic instrument to obtain and

confirm agreement between extinction and absorption measurements. One consideration for this calibration method, however, is evidence that NO_2 photodissociates to some extent at 405 nm, causing a reduction in the observed absorption signal. This issue will be discussed further in Chapter 3 where calibration methods are considered.

2.2 Instrument Design and Laser Alignment

The beams of the two lasers employed on the dual-wavelength photoacoustic instrument must both be directed cleanly through the resonator. Unwanted interaction of the lasers with the resonator walls introduces additional background light scattering and lowers the available laser power for absorption measurement. The windows employed to allow the laser beam to enter and exit the resonator have a broadband anti-reflective coating that allows maximum transmittance of both 405 nm and 870 nm radiation (CVI Laser, LLC product number W2-PW1-1025-UV-670-1064-0). The two laser beams are combined outside of the resonator so that the beams overlap and enter the resonator cavity coincidently. A long wave pass dichroic beamsplitter specified to transmit 850 nm radiation and reflect 400 nm radiation (CVI Laser, LLC product number LWP-45-RS400-TP850-PW-1025-UV) is used for combining the beams. Product specifications for the beamsplitter provide that reflectance is greater than 99.5% at 400 nm, and average transmission is greater than 85% for long wave pass beamsplitters.

The primary limiting factor on the sensitivity of photoacoustic measurement is the laser power. More laser power produces more energy absorbed and, therefore, larger acoustic pressure values. The modulated laser power at 405 nm was 93 mW, and was 900 mW at 870 nm. Using the inverse wavelength dependence of aerosol light

absorption, the 870 nm measurement signal to noise ratio (sensitivity) is 5 times that of the 405 nm measurement. The 405 nm laser, because it has lower optical power output so that greater absolute efficiency is needed at that wavelength, is reflected by the beamsplitter while the 870 nm beam is transmitted. For maximum efficiency the reflected laser beam is S-polarized (polarized perpendicular to the plane created by normal to beamsplitter surface and laser propagation direction), and the transmitted beam is P-polarized (parallel polarization). The lasers are aligned perpendicularly, and the surface of the beamsplitter is aligned at an angle of 45 degrees to the propagation direction of both beams.

The original design for laser alignment included two broadband mirrors with rotation capability positioned on an optical table to direct the combined beams into the resonator. Each laser was mounted on a "5-axis Aligner" (New Focus product number 9082) with translation and pivoting capability. The original system for laser combination and direction, including the two mirrors, is shown in Figure 2.1.

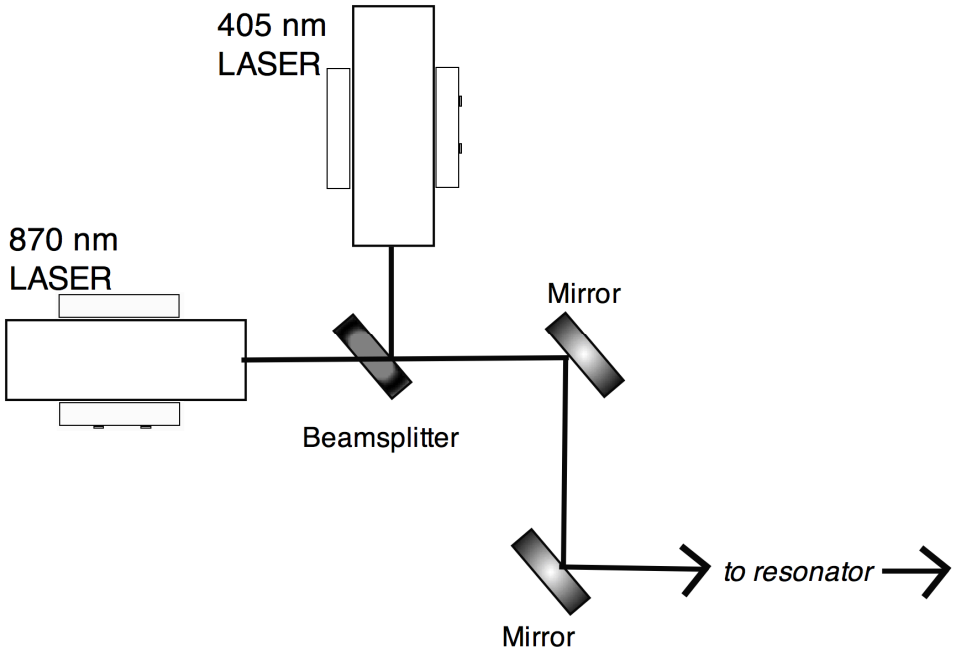

Figure 2.1 Arrangement of lasers, long wave pass dichroic beamsplitter and mirrors in original laser combination and alignment scheme

The first mirror served primarily to direct the combined beams to the appropriate height, while the second provided further beam direction in both the vertical and horizontal planes so that the lasers could be guided cleanly through the resonator. This design gave maximum control of laser alignment and beam direction. However, it increased the distance needed between the lasers and the resonator and added to instrument size. In addition, the increased number of optical elements complicated alignment of the lasers.

The current alignment scheme, as shown in the dual-wavelength photoacoustic instrument schematic in Figure 2.2, does not employ the mirrors to direct the two beams into the resonator. Instead, a drafting program, Solid Works, was used to construct a finely machined aluminum plate that the lasers and beamsplitter are bolted to. Precise measurements of laser propagation through the beamsplitter allow for simple beam combination and laser alignment without additional optical elements. The laser plate

rests on an adjustable platform. Slight manipulation of both the laser/beamsplitter platform as well as minor rotational adjustment of the beamsplitter provide additional control of laser alignment.

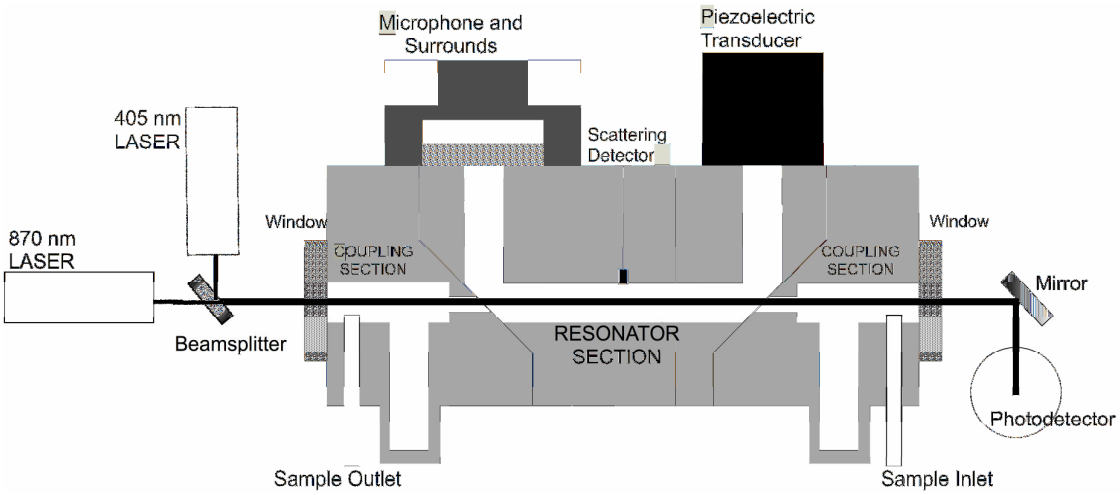

Figure 2.2 Schematic of dual-wavelength photoacoustic instrument. Two laser beams are combined and directed into the resonator by a long wave pass dichroic beamsplitter. A mirror guides the exiting laser beams into an integrating sphere containing photodetectors for measurement of laser power at each wavelength

On the dual-wavelength photoacoustic instrument the integrating sphere containing the photodetectors for laser power measurement is positioned so that a mirror is needed to direct into it the laser beams exiting the resonator cavity. This arrangement, in contrast to that of the integrating sphere placed directly in line with the exiting beams, reduces radiation scattered back out of the sphere into the resonator.

Two photodiodes are used within the integrating sphere to measure laser power at each wavelength after the beams have exited the resonator. The optical power of the 870 nm laser is such that it would saturate both photodiodes if filters were not used in front of the detectors. A short pass filter with 750 nm cut-off wavelength (Edmund Optics product number NT47-585) reduces the 870 nm radiation reaching the photodiode that

measures 405 nm laser power. The optimal set-up would employ a second short pass filter in this position, but the current arrangement uses two absorptive neutral density filters of optical density 0.2 and 0.3 in front of the short pass filter. Another neutral density filter of optical density 1.0 is used in front of the photodiode which measures 870 nm laser power.

2.3 Dual-Wavelength Photoacoustic Signal Measurement

The operating frequency of the photoacoustic instrument is the temperature and relative humidity-dependent resonance frequency of the resonator cavity. In the single-wavelength instrument the laser is power modulated at this resonance frequency, and the phase of the Fourier-transformed laser power measurement serves as the reference for phase-sensitive detection. In the dual-wavelength instrument simultaneous measurement of two light absorption-induced pressure fluctuations is necessary. If both acoustic signals were modulated and analyzed at resonance the resulting microphone pressure would be a combination of the two, and the individual signals could not be separated. Therefore, in the dual-wavelength photoacoustic instrument the 405 nm laser is power modulated at resonance frequency, f_o, and the 870 nm laser is modulated off of resonance: f_o+df. The microphone pressure corresponding to one photoacoustic signal is measured at resonance, $P_m(f_o)$, and the other is measured off of resonance, $P_m(f_o+df)$. A typical value for df is five Hz, which is large enough for signal separation but close enough to f_o to still have adequate resonance enhancement of the acoustic pressure fluctuation.

Another important consideration is that calculation of light absorption using the resonance-enhanced microphone pressure in the photoacoustic equation, Equation 1.1 in Chapter 1, assumes that the magnitude of the microphone power is measured at resonance frequency. Consequently, the Fourier-transformed microphone pressure that is measured at f_o+df must be transferred and analyzed as if it occurred at f_o. The transfer function was introduced in Chapter 1 in the discussion of photoacoustic noise in Section 1.6. To review, the dependence of resonance-enhanced acoustic pressure on frequency is given by

$$\tilde{P}(f) = \frac{P_o}{\frac{2Q(f - f_o)}{f_o} + i}, \qquad \text{(Eq. 2.2)}$$

where P_o is the peak acoustic pressure at resonance, and Q is the resonator quality factor. The transfer function is the ratio of Equation 2.2 evaluated at f_o to the same pressure function measured at a different frequency, for example $f = f_o+df$:

$$\tilde{G}(f - f_o) \equiv \frac{\tilde{P}(f_o)}{\tilde{P}(f)}$$

$$\tilde{G}\left(\left(f_o + df\right) - f_o\right) = \tilde{G}(df) \equiv \frac{P(f_o)}{P(f_o + df)} = 1 - i\frac{2Qdf}{f_o}. \qquad \text{(Eq. 2.3)}$$

The magnitude of the complex transfer function $G(df)$ is

$$G(df) = \sqrt{\left(\frac{2Qdf}{f_o}\right)^2 + 1}, \qquad \text{(Eq. 2.4)}$$

and the phase of $G(df)$ in radians is

$$\phi_{G(df)} = -\arctan\left[\frac{2Qdf}{f_o}\right]. \qquad \text{(Eq. 2.5)}$$

Light absorption using a microphone pressure measured off of resonance at frequency *f* is proportional to the real part of the ratio of complex microphone power to laser power, both at frequency *f*, multiplied by the transfer function $G(f - f_o)$ as follows:

$$\beta_{abs}(f) \sim \mathrm{Re}\left[\frac{\tilde{P}_m(f)}{\tilde{P}_L(f)}\tilde{G}(f-f_o)\right] = \mathrm{Re}\left[\frac{P_m e^{i\phi_m}}{P_L e^{i\phi_L}}G(f-f_o)e^{i\phi_G}\right]$$

$$= \frac{P_m}{P_L}G(f-f_o)\cos(\phi_m - \phi_L + \phi_G) \qquad \text{(Eq. 2.6)}$$

Thus, the photoacoustic equation used to measure light absorption at 870 nm in the dual-wavelength photoacoustic instrument is

$$\beta_{abs}(f_o + df) = \frac{P_m(f_o+df)}{P_L(f_o+df)}G(df)\frac{A_{res}}{\gamma - 1}\frac{\pi^2 f_o}{Q}\cos(\phi_m - \phi_L + \phi_G), \qquad \text{(Eq. 2.7)}$$

and that used to calculate β_{abs} at 405 nm is Equation 2.7 with *df* equal to zero. In this way independent measurements of light absorption at two different wavelengths are conducted simultaneously within a single photoacoustic instrument resonator.

2.4 References

Anderson, T. L., Covert, D. S., Marshall, S. F., Laucks, M. L., Charlson, R. J., Waggoner, A. P., Ogren, J. A., Caldow, R., Holm, R. L., Quant, F. R., Sem, G. J., Wiedensohler, A., Ahlquist, N. A., and Bates, T. S. (1996). Performance characteristics of a high sensitivity, three wavelength, total scatter/backscatter nephelometer. *Journal of Atmospheric and Oceanic Technology* **13,** 967-986.

Arnott, W. P., Moosmüller, H., and Walker, J. W. (2000). Nitrogen dioxide and kerosene-flame soot calibration of photoacoustic instruments for measurement of light absorption by aerosols. *Review of Scientific Instruments* **71**(7)**,** 4545-4552.

Crutzen, P. J. (1979). The role of NO and NO2 in the chemistry of the troposphere and stratosphere. *Annual Review of Earth and Planetary Sciences* **7,** 443-472.

Kirchstetter, T. W., Novakov, T., and Hobbs, P. V. (2004). Evidence that the spectral dependence of light absorption by aerosols is affected by organic carbon. *Journal of Geophysical Research* **109**(D21209)**,** doi:10.1029/2004JD00499.

3 Instrument Calibration

3.1 Introduction

A number of instruments that are widely used in measurement of light absorption and scattering by atmospheric aerosols have been described in the previous chapters. For many, such as filter-based absorption measurements which offer a simple and precise method, the challenge in their use is development of adequate calibration and cross sensitivity analysis. In addition, commercially available integrating nephelometers utilize gaseous calibration by Rayleigh scattering with gases such as CO_2 or refrigerants (Anderson et al., 1996). The particle scattering calibration scheme used in the photoacoustic instrument avoids the need for corrections used in commercially available nephelometers when they are used to measure scattering by particles instead of scattering by gases. In this chapter calibration of the dual-wavelength photoacoustic instrument, including theory, results and uncertainties, will be discussed.

The calibration method described employs sufficiently high concentrations of either absorbing gas or laboratory-produced particulate matter to obtain simultaneous measurements of extinction, absorption and scattering. Two different aerosol species are used in this calibration method, one which only scatters radiation and one in which at least 70 percent of the extinction is due to absorption. Use of a wide range of particle properties and gaseous absorption allows for analysis of instrument performance over all ranges of operation. Nitrogen dioxide (NO_2), which strongly absorbs radiation at 405 nm, is used to evaluate the absorption calibration at that wavelength. Soot from a kerosene flame is the absorbing aerosol. A similar method of photoacoustic instrument

calibration using NO_2 and kerosene-flame soot at 532 nm and 1047 nm has been reported by Arnott, Moosmüller and Walker (2000). The scattering aerosol used for calibration is derived from simple table salt dissolved in water, nebulized to form solution droplets, and dried to form submicron-sized salt aerosol.

Measurement of extinction is obtained from transmittance of the gas or aerosol sample. Absorption is measured by the photoacoustic method, and scattering is measured by reciprocal nephelometry in the photoacoustic resonator as described in Section 1.7 of Chapter 1. When sufficiently high concentrations of the gas or aerosol are introduced into the resonator the transmissivity of the sample decreases resulting in a decrease in laser power measured by the photodetector. The extinction of laser power is understood to come entirely from either absorption by NO_2 gas or scattering by salt particles (measured independently), so that extinction measurements can be equated to either absorption or scattering measurements. For calibration using kerosene-flame soot at both 405 nm and 870 nm scattering is assumed to be accurately calibrated from the salt procedure. Extinction measurements and the sum of photoacoustic absorption and scattering measurements are compared.

The calibration method for photoacoustic instruments employs independent measurement and seeks closure between extinction and absorption plus scattering. This method is simple and robust. No precise knowledge of absorbing gas or aerosol concentration is needed for the extinction calibration, and it is useful to be able to equate the independent measurements. A calibrated resonator (with measured resonance frequency and quality factor), calibrated photodiode (known laser power for a given photodiode voltage), and calibrated microphone (known acoustic pressure per

microphone voltage) are assumed in use of the theory for determining the photoacoustic absorption coefficient. Reasonable agreement is found between extinction and measured absorption and scattering coefficients when these assumptions are fulfilled. Perfect closure, however, is never obtained due to uncertainties and perhaps non-ideal behavior of certain elements, such as the scattering sensor head.

3.2 Calibration Theory

The calibration method for the photoacoustic instrument uses measurement of sample transmittance, T, to determine the coefficient of extinction, β_{ext}. Recall, the coefficient of extinction is defined as the sum of absorption and scattering coefficients. Transmittance can be expressed using the Beer-Lambert law

$$T = \exp(-\beta_{ext} L), \qquad \text{(Eq. 3.1)}$$

where L is the path length. The product of extinction coefficient and path length is often expressed as the dimensionless optical depth, τ, of the sample:

$$\tau = \beta_{ext} L . \qquad \text{(Eq. 3.2)}$$

Assuming an initial radiation intensity I_o, which is reduced to intensity I after traversing the sample path length, transmittance can be expressed as

$$T = I / I_o = \exp(-\beta_{ext} L). \qquad \text{(Eq. 3.3)}$$

Therefore, measurement of laser radiation intensity through a known path length allows for calculation of the coefficient of extinction, β_{ext}.

For calibration I_o is taken to be the initial laser intensity, or laser power measured by the photodetector through the "clean" resonator when no sample is present. Laser

power I is measured as the NO_2 gas or aerosol sample is introduced. The sample path length is the resonator cavity length: L = 24.86 cm. The coefficient of extinction, calculated from sample transmissivity, is then compared to either the coefficient of absorption (NO_2 gas calibration) for calibration of photoacoustic absorption at 405 nm, or the coefficient of scattering (salt aerosol calibration) for calibration of scattering measured by the instrument. The kerosene-flame soot aerosol calibration of absorption at 405 nm and 870 nm is conducted following the calibration of the scattering measurement. The extinction measured by kerosene-flame aerosol is compared to the sum of photoacoustic absorption and scattering coefficients. Kerosene soot has a very low single scattering albedo, so that scattering by the aerosol is very small compared to absorption.

The simple theory described in this section for use during instrument calibration is adequate given the gas or aerosol sample meets certain criteria. Use of the Beer-Lambert law assumes only single scattering by the individual particles, and does not take into account multi-scattering theory. The optical depth of the sample (τ) must be much less than one so that multiple scattering can be ruled out. This is the case for the calibration procedure described here. Any additional attenuation of laser intensity and its effects on the scattering measurement is also not accounted for by the theory. The ideal dynamic range for gas or aerosol concentration in the resonator during calibration is bounded by two requirements. Concentration must be sufficiently high that a measurable drop in laser intensity exists. However, it must not be so high as to induce multiple scattering, additional light attenuation, or to exceed the range of measurement of the sensor in the resonator that quantifies light scattering.

3.3 Experimental Set-Up

Calibration of the dual-wavelength photoacoustic instrument was conducted in the laboratory. The sample inlet line entering the resonator was split, and a quarter turn valve at this "T" allowed for selection of ambient air or sample air. Either ambient air or the gas/aerosol sample was constantly drawn through the instrument by a pump on the outlet. Manual control of the sample through the filter also allowed for selection of particle laden versus clean air.

Nitrogen dioxide in air at a concentration of 500 parts per million, stored in a gas cylinder, could be gradually introduced into the sample line using the valve on the outlet of the cylinder. The gas concentration of the NO_2 sample was increased until absorption at 405 nm reached an acceptable level (approximately 100,000 Mm^{-1}) such that the measured laser power decreased by at least two percent. After either a steady increase or maintaining of the desired concentration of gas for two or more minutes the NO_2 valve was shut off and ambient air was drawn into the resonator. The NO_2 gas calibration results are discussed further in Section 3.4.

Figure 3.1 shows a schematic of the arrangement used to produce and draw the scattering aerosol through the photoacoustic instrument for calibration purposes. Common table salt was used to produce the aerosol used in the instrument's scattering calibration. Approximately 0.3 grams of salt were dissolved in 1 liter of water and enclosed in a container. Two misters, normally used to generate special-effects fog as entertainment, were placed in the water inside the container. The misters are ultrasonic nebulizers that produce small airborne droplets of the solution. The droplets were drawn out of the container and through an aerosol dryer by a vacuum pump. A sample outlet

line connected to the container top, and other holes for ventilation and mister power cords were drilled in the sides of the solution container. The moist salt aerosol droplets produced by the misters were drawn out through the top of the container and into an aerosol dryer. The aerosol dryer consists of a perforated pipe surrounded by an indicating silica gel desiccant, all within a Plexiglas cylinder. The desiccant surrounds the aerosol flow path and removes excess moisture by diffusional capture, but does not come into contact with the particles. The desiccant is made up of silica gel beads which change color from blue to pink to indicate when they have become saturated with moisture. The length of the aerosol dryer (and length of aerosol flow path) is approximately 0.8 m. Dry salt particles were drawn out of the aerosol dryer and into the photoacoustic resonator for scattering calibration measurements. The concentration of scattering particles was regulated by control of the misters which could either be used alone or simultaneously, and on one of three settings. Typically only one mister on its lowest setting produced enough scattering aerosol for a sufficient extinction measurement at both 405 nm and 870 nm. The air sample was diverted through the photoacoustic instrument's filter before and after a calibration run to obtain reference laser power, I_o.

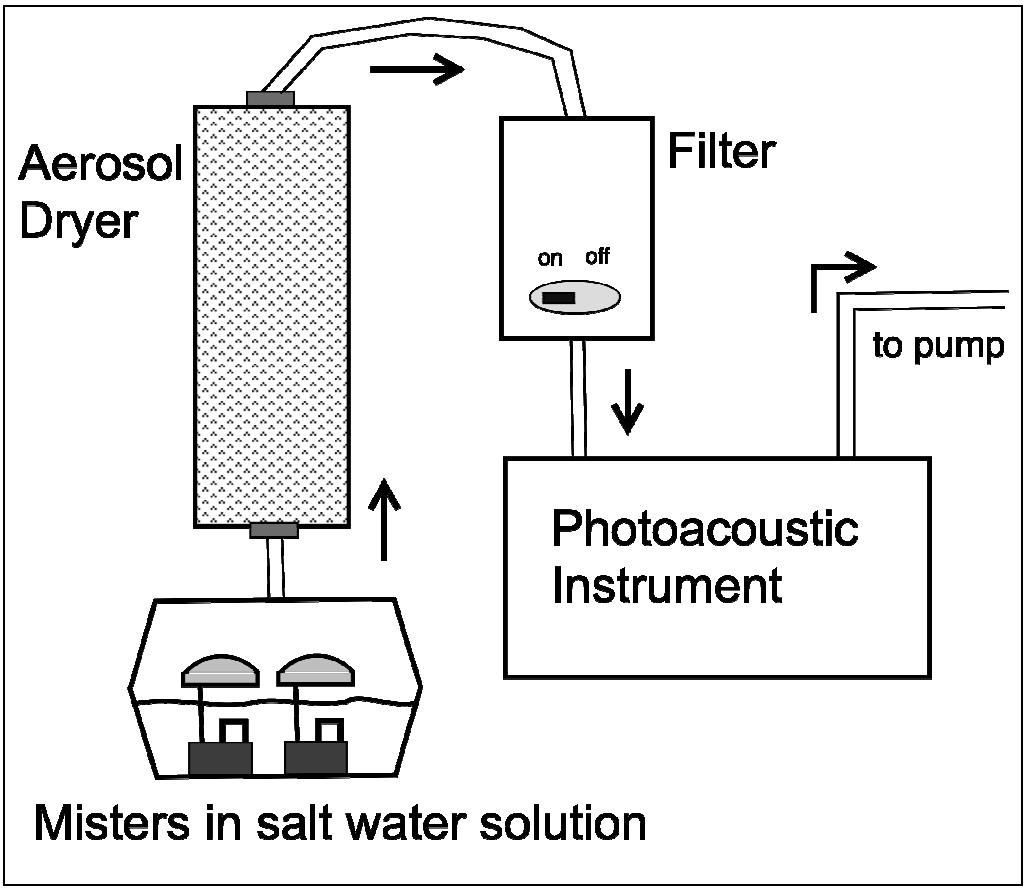

Figure 3.1 Schematic of scattering aerosol production and calibration set-up. Misters are used to generate mist or fog.

A kerosene lamp was used to produce the soot aerosol for calibration of photoacoustic absorption. A standard kerosene lamp was lit with a longer wick than normal so that excess soot was produced by the fuel-rich flame. The lamp was placed under an inverted and slightly elevated mixing chamber (a large metal garbage can) within the fume hood which allowed for cooling and mixing of the soot produced by the kerosene flame with ambient air. A sample line extending under the can drew the kerosene-flame soot sample into the photoacoustic instrument. A schematic diagram of absorbing aerosol production and delivery into the instrument is shown in Figure 3.2. The concentration of soot aerosol was controlled by the lamp flame and wick height. The

sample was diverted through the filter before and after calibration runs to obtain particle-free reference measurements.

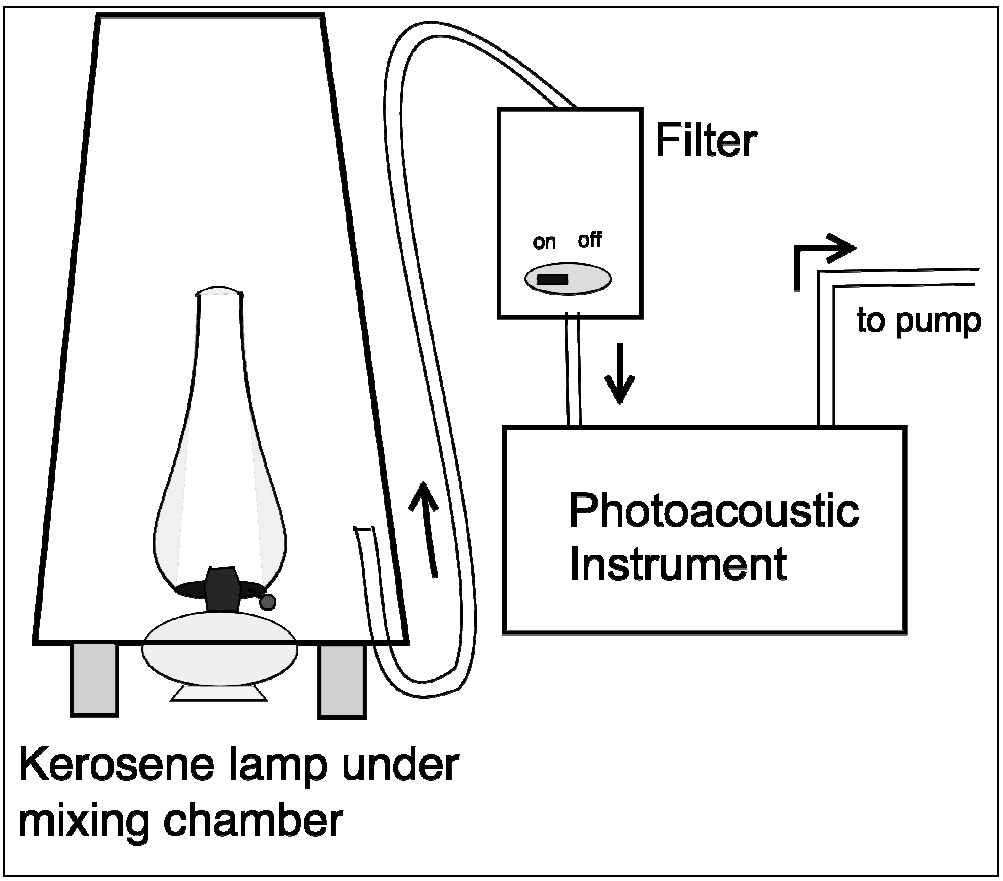

Figure 3.2 Schematic of absorbing aerosol production and calibration set-up.

3.4 Calibration Results

For NO_2 gas calibration of photoacoustic absorption at 405 nm NO_2 gas was drawn into the "clean" resonator twice for two independent measurements of extinction versus absorption. These two runs are the NO_2 gas absorption calibration and are referred to as "Run 1" and "Run 2," in the order they were conducted. Time series measurements of laser power, absorption and calculated extinction at 405 nm are depicted for Run 1 and Run 2 in Figures 3.3a and 3.3b, respectively.

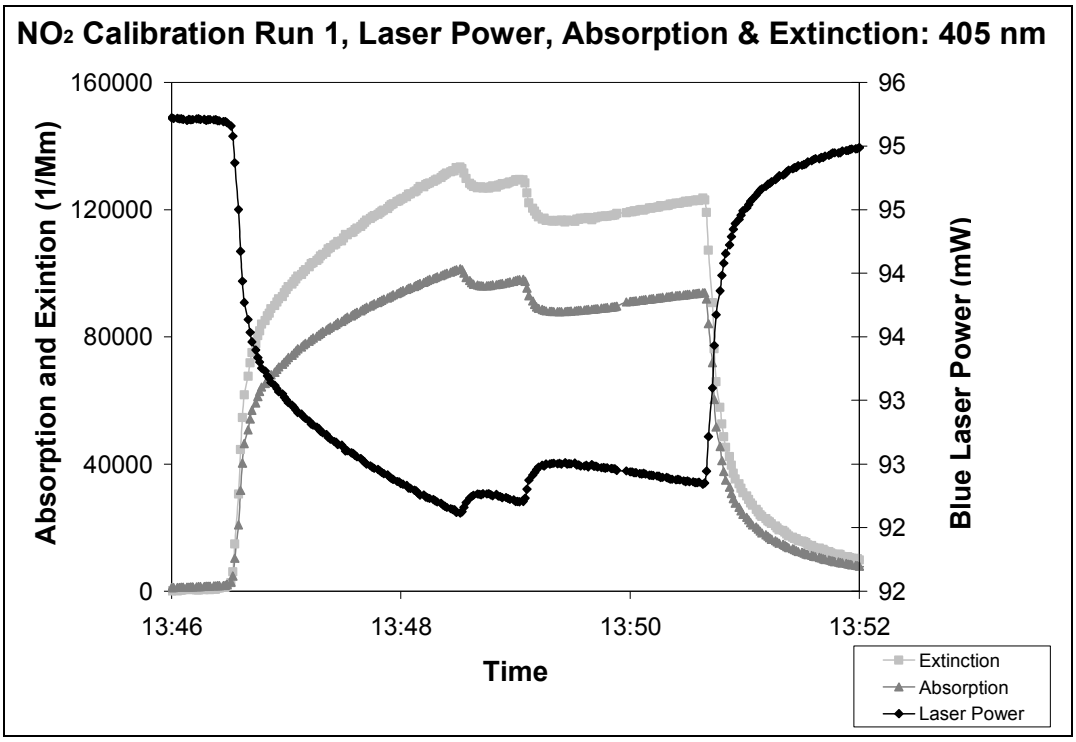

Figure 3.3a Time series of NO_2 calibration Run 1, including 405 nm laser power, absorption and extinction calculated from gas transmissivity

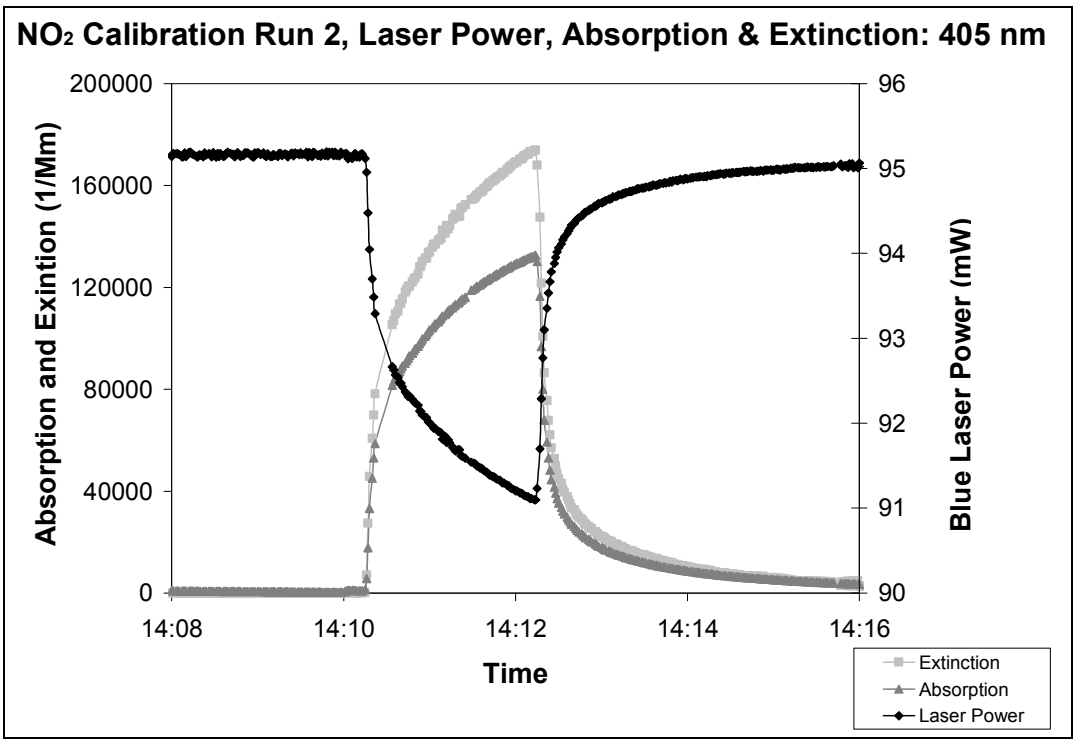

Figure 3.3b Time series of NO_2 calibration Run 2, including 405 nm laser power, absorption and extinction calculated from gas transmissivity

Photoacoustic measurements of light absorption by gas or aerosol are calculated from first principles using Equation 1.1 in Chapter 1. This equation uses the measured laser power, microphone pressure and other properties of the acoustical resonator. An evaluation of this method is provided by the comparison of measured gaseous extinction (or extinction due to an absorbing aerosol) with measured absorption.

Extinction, as determined using the theory presented in Section 3.2, is shown versus photoacoustic absorption by the NO_2 gas at 405 nm in Figure 3.4. Figure 3.4 depicts calculations and measurements from both Run 1 and Run 2. A linear fit has been applied, and the linear equation and corresponding R^2 correlation value are given for each line. The R^2 value for the linear fit of both data sets is very near unity, indicating excellent linear correlation between absorption and extinction. If all extinction was due to absorption, and absorption was perfectly calibrated to equal extinction by the gas, then the slope of the lines would be equal to one. According to the measurements presented in Figure 3.4, absorption at 405 nm should be increased by 30% to account for the total extinction by the NO_2 gas.

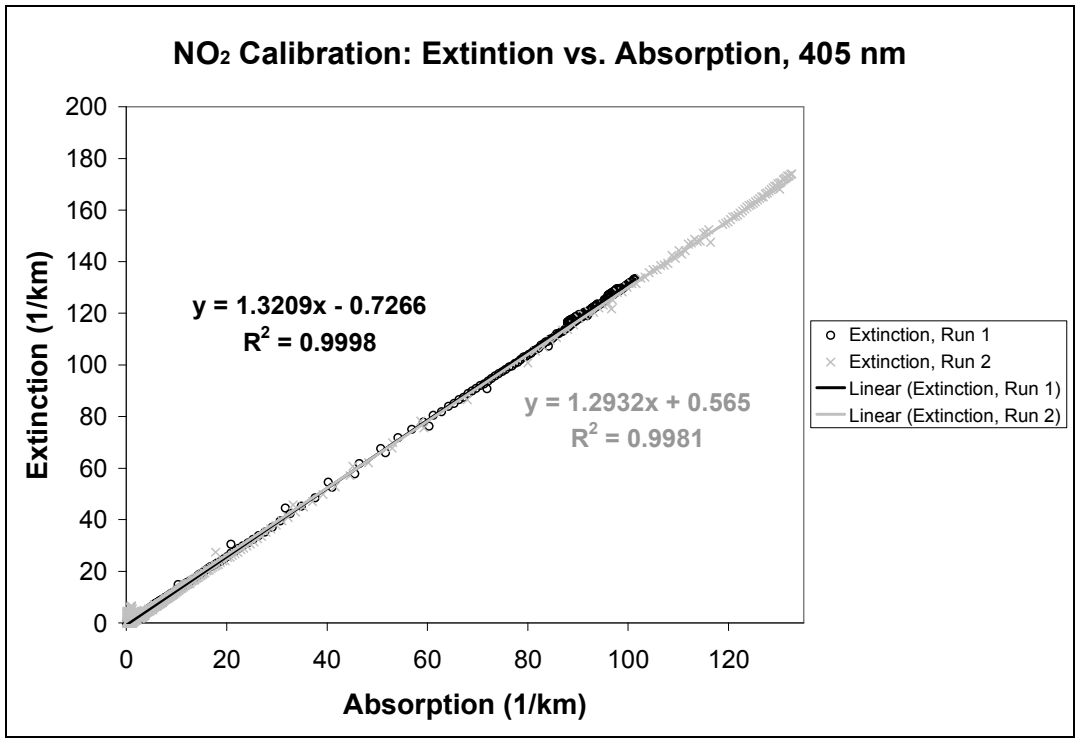

Figure 3.4 NO_2 gas calibration results

Some question exists as to whether all extinction is due to absorption by the NO_2 gas at 405 nm. NO_2 is known to photodissociate into O + NO when subject to radiation wavelengths smaller than about 400 nm (Arnott, Moosmüller, and Walker, 2000). When the molecule disassociates some energy goes into its breakup, and not all of the absorbed energy is converted into heat in the surrounding air. Therefore, light extinction would be expected to be greater than measured photoacoustic absorption. The discrepancy between extinction and the lower levels of absorption, especially in light of kerosene-flame soot absorption calibration results, suggests that some photodissociation of NO_2 may occur at 405 nm. The adjustment to absorption measurements suggested by the kerosene-flame soot calibration is less than 10%, as will be shown later in this section. In

other words, 20% of the extinction by NO_2 is inferred to be due to the energy loss associated with photodissociation of NO_2.

Scattering measurements are calibrated with the assumption of a linear relationship between particle scattering coefficients and the photodetector voltage. The slope and offset in the linear fit need to be determined for each wavelength. The offset is determined from particle-free measurements and is subtracted from subsequent measurements. Only the slope needs to be determined by particle calibration of scattering. Use of particles with negligible absorption allows for the expectation that extinction and scattering should be equal, and thus for the scattering calibration.

Three independent runs were conducted for the scattering calibration of the instrument using the salt aerosol. Time series measurements of laser power, scattering, and calculated extinction due to scattering at both 405 and 870 nm are depicted for each run in Figures 3.5a, 3.5b and 3.5c. Scattering and extinction are indicated on the left vertical axis; laser power is given on the right vertical axis. In each of these figures the measured 405 nm laser power has been multiplied by a factor of 10 for ease of observation.

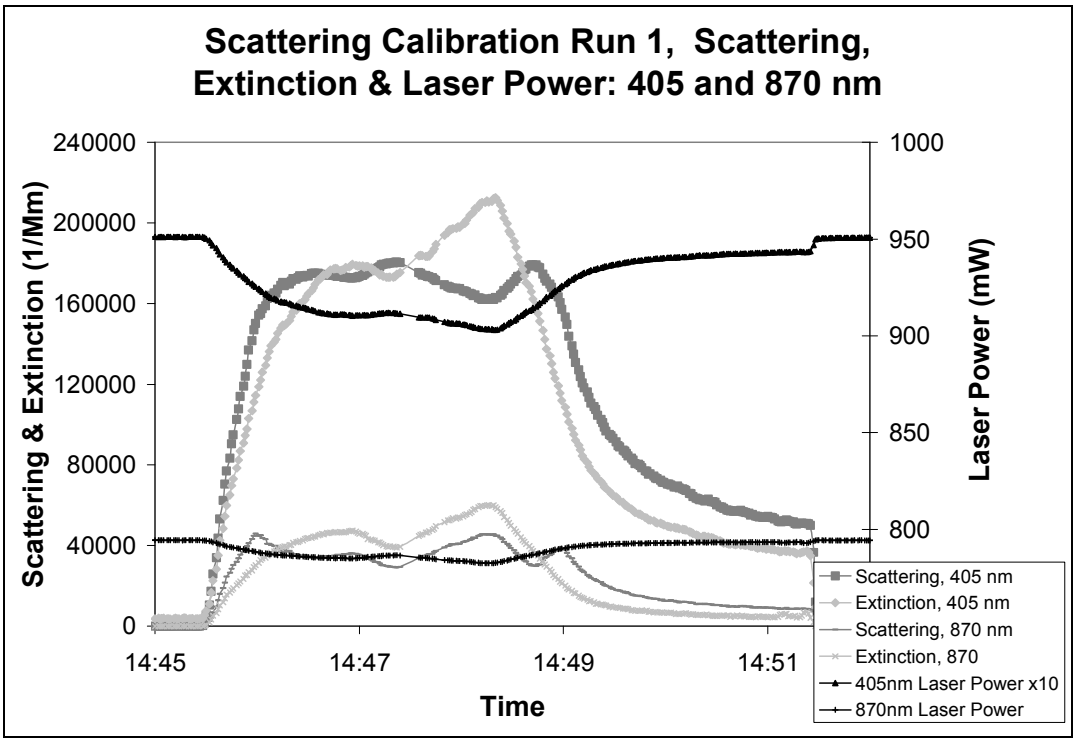

Figure 3.5a Time series of scattering calibration Run 1 at 405 and 870 nm, including laser power and coefficients of scattering and extinction

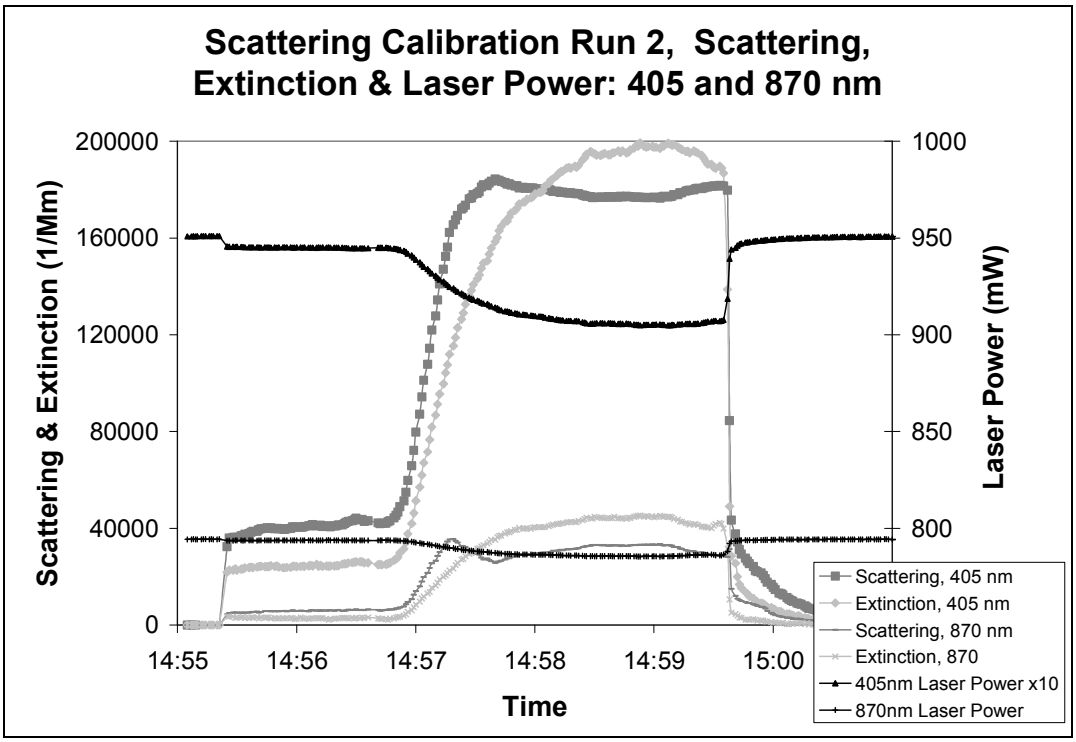

Figure 3.5b Time series of scattering calibration Run 2 at 405 and 870 nm, including laser power and coefficients of scattering and extinction

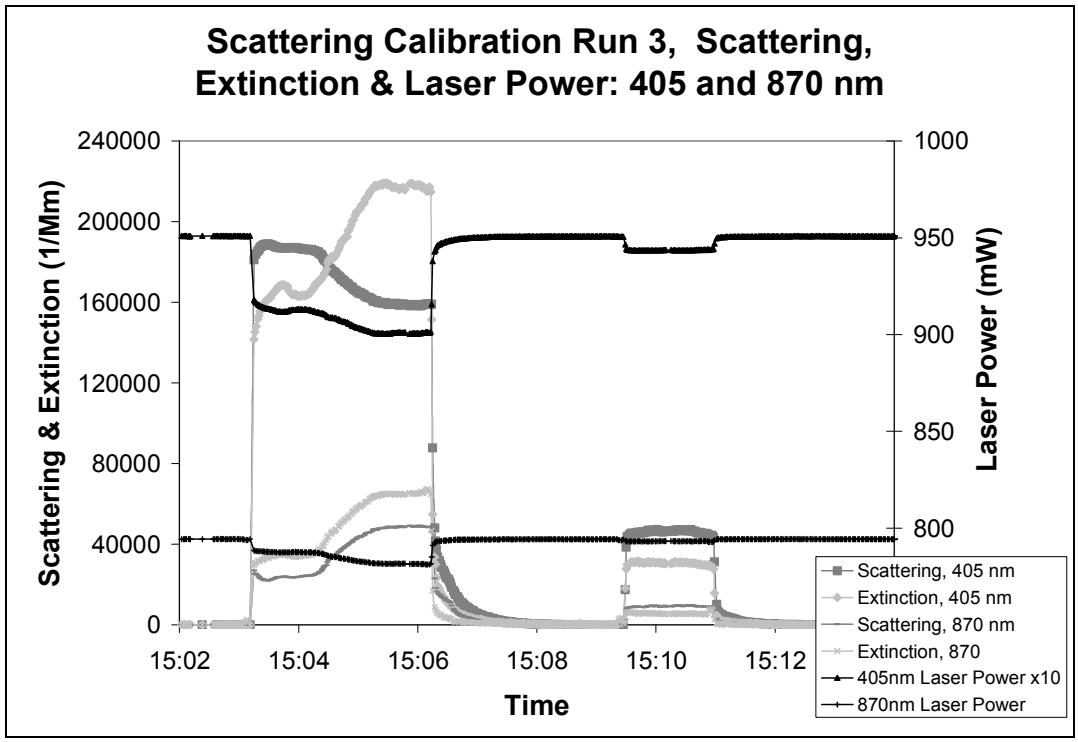

Figure 3.5c Time series of scattering calibration Run 3 at 405 and 870 nm, including laser power and coefficients of scattering and extinction

Extinction due to scattering is depicted versus the coefficient of scattering measured by the instrument in Figures 3.6a and 3.6b. Figure 3.6a shows extinction and scattering at 405 nm, and Figure 3.6b is that at 870 nm. A linear fit of the data for each run is included, as well as corresponding linear equations and R^2 values. Only scattering measurements at 405 nm from the beginning of each calibration run that are less than 100,000 Mm^{-1} (and corresponding extinction values) are presented in Figures 3.6a and 3.6b. Scattering coefficients at 405 nm greater than 100,000 Mm^{-1} are thought to be out of the dynamic range that allows for accurate measurement by the scattering photodetector and use of the calibration theory presented in Section 3.2.

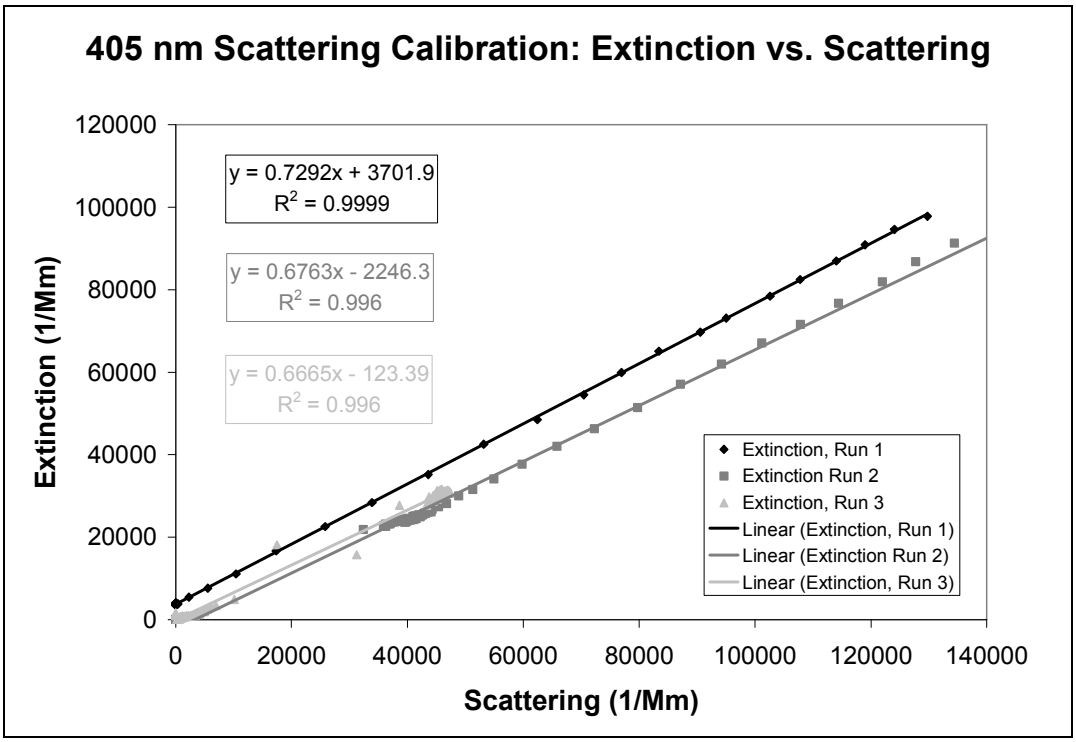

Figure 3.6a Scattering calibration results at 405 nm

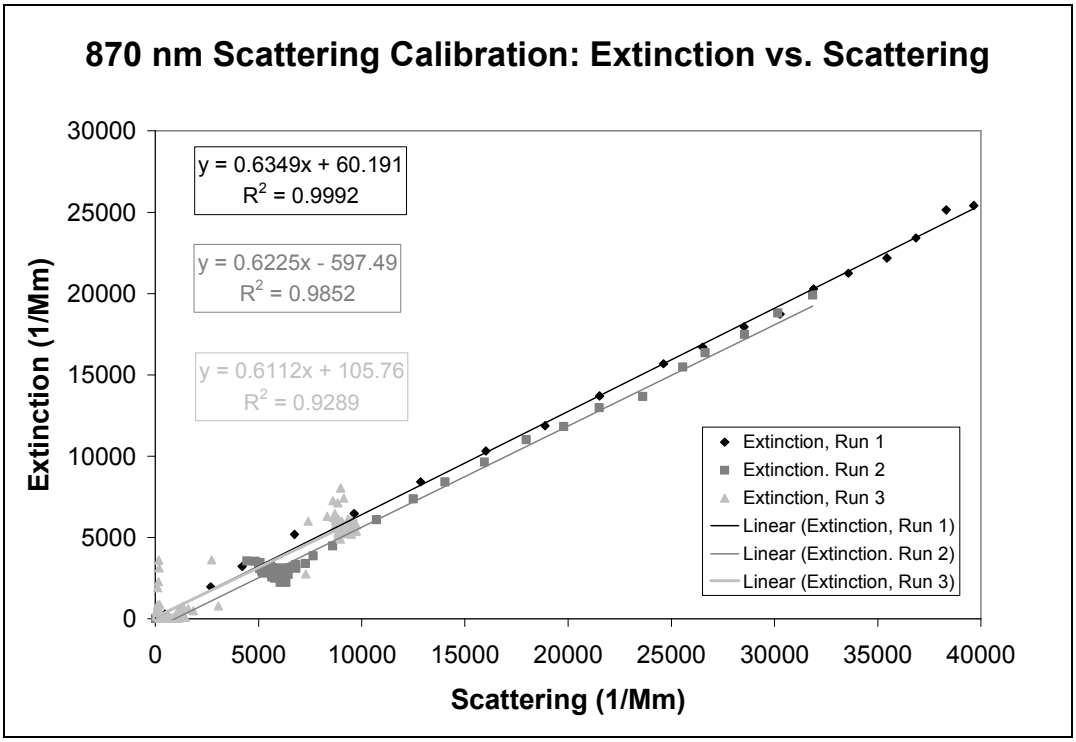

Figure 3.6b Scattering calibration results at 870 nm

The measurements shown in Figure 3.6a indicate that the coefficient of scattering measured by the photoacoustic instrument at 405 nm is too large compared with previously used values by 27% to 33%. Those in Figure 3.6b suggest that the coefficient of scattering at 870 nm needs to be reduced by 37% to 39%. These scattering calibrations at both 405 nm and 870 nm can be applied to the scattering coefficient measured during kerosene-flame soot calibration runs.

Kerosene-flame soot was used in two calibration runs for the calibration of photoacoustic absorption at both 405 nm and 870 nm. Measurements of absorption, laser power and calculated extinction as a function of time are shown for Run 1 in Figure 3.7a and for Run 2 in Figure 3.7b. The figures depict measurements at both operational wavelengths. Absorption and extinction values are given on the left vertical axis, and laser power is on the right vertical axis. Measurements of 405 nm laser power in Figures 3.7a and 3.7b have been multiplied by a factor of 10.

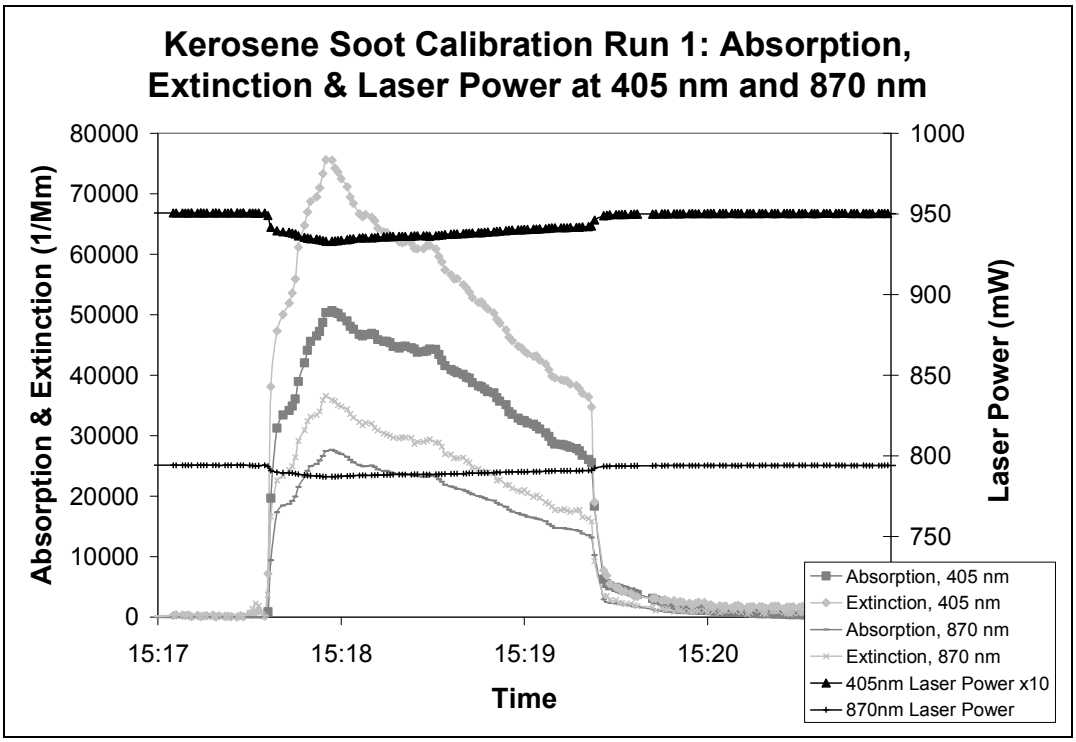

Figure 3.7a Time series of absorption calibration Run 1 at 405 and 870 nm, including laser power and coefficients of scattering and extinction

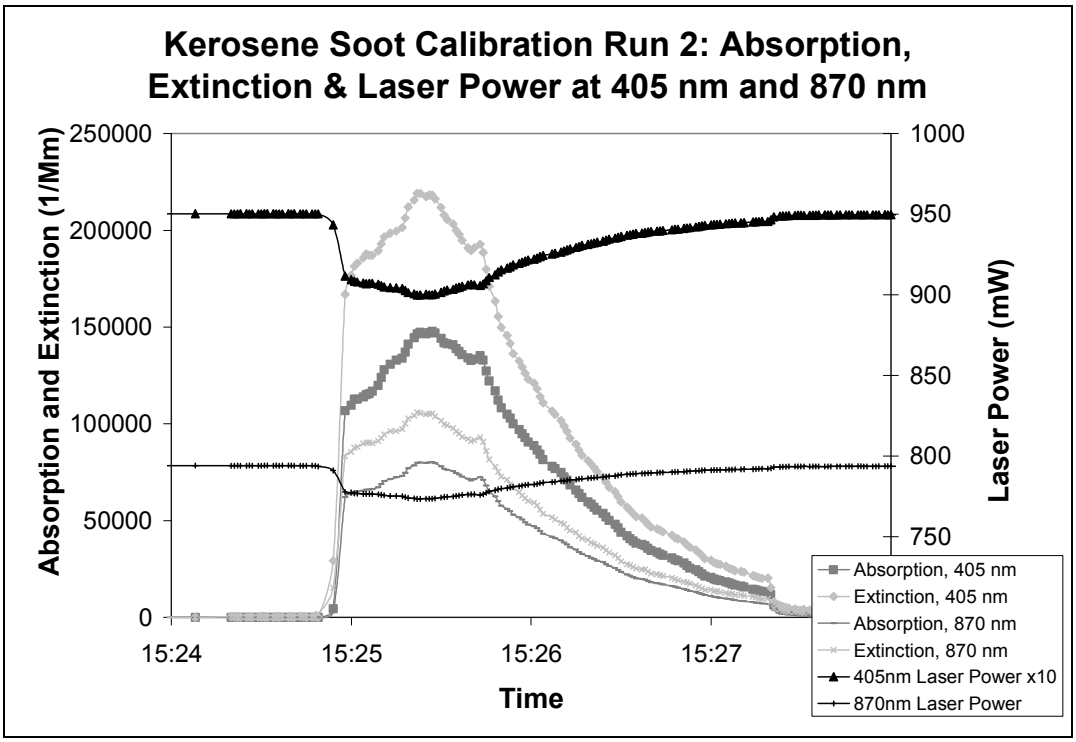

Figure 3.7b Time series of absorption calibration Run 2 at 405 and 870 nm, including laser power and coefficients of scattering and extinction

The adjustments suggested by the scattering calibration can be applied to the scattering coefficients measured during the kerosene soot absorption calibration. Results from the kerosene soot calibration where the scattering calibration has been applied and where it has not been applied are both presented. The average of the three slopes for each linear fit of extinction versus scattering in Figures 3.6a and 3.6b provides the scattering calibration factor. (See the expression for calculating the scattering coefficient, including calibration factor α, in Equation 1.27 in Chapter 1.) The resulting calibration factors to multiply scattering values by are 0.69 and 0.62 for 405 nm and 870 nm, respectively.

Figure 3.8a shows calibration results at 405 nm in which the scattering calibration from the three salt aerosol runs has been applied to kerosene soot scattering measurements. Figure 3.8b shows the same for measurements at 870 nm. Measured scattering coefficients, multiplied by the appropriate calibration factor, are subtracted from extinction coefficients to obtain aerosol light absorption. Figures 3.8a and 3.8b present absorption from this procedure versus measured photoacoustic absorption. The left vertical axis corresponds to measurements from Run 1, and the right to measurements from Run 2. Linear fits have been applied to the independent measurements at both wavelengths, and the linear functions and R^2 correlations are included next to the lines. The slopes of the linear fit results in Figure 3.8a indicate that coefficients of absorption measured at 405 nm should be increased by 10% to 12%. The calibration results for photoacoustic absorption measurements at 870 nm indicate the need for a 13% to 16% increase in measured absorption coefficients.

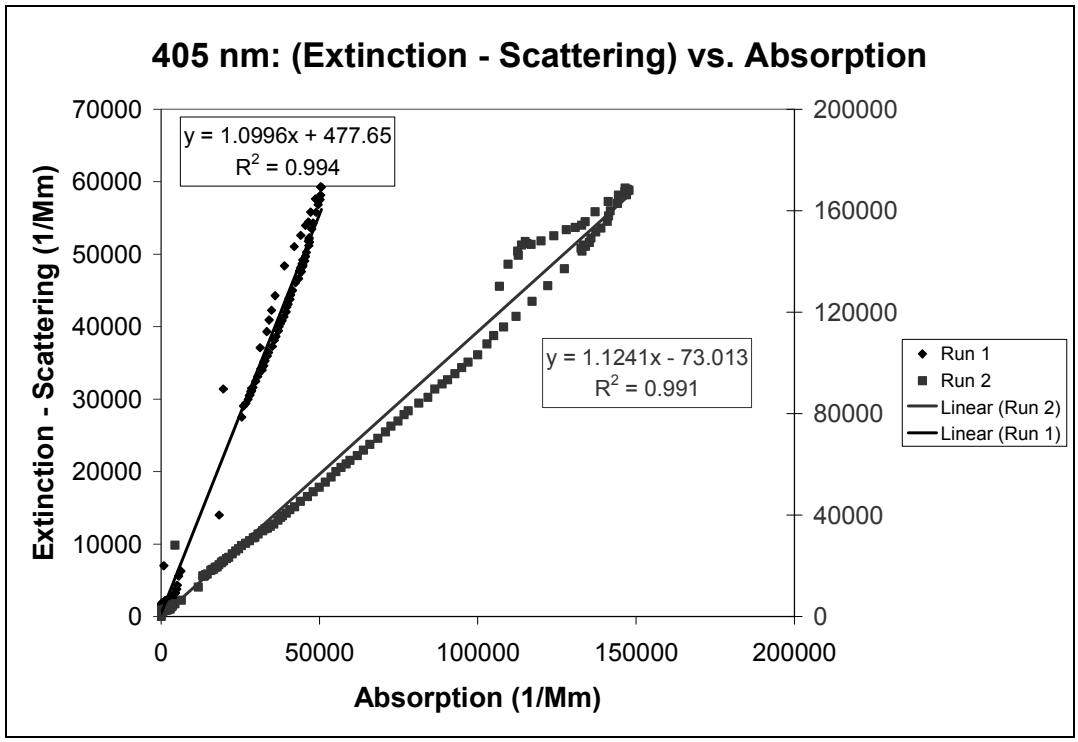

Figure 3.8a Kerosene-flame soot absorption calibration results for measurements at 405 nm; new scattering calibration factors applied to measured scattering coefficients

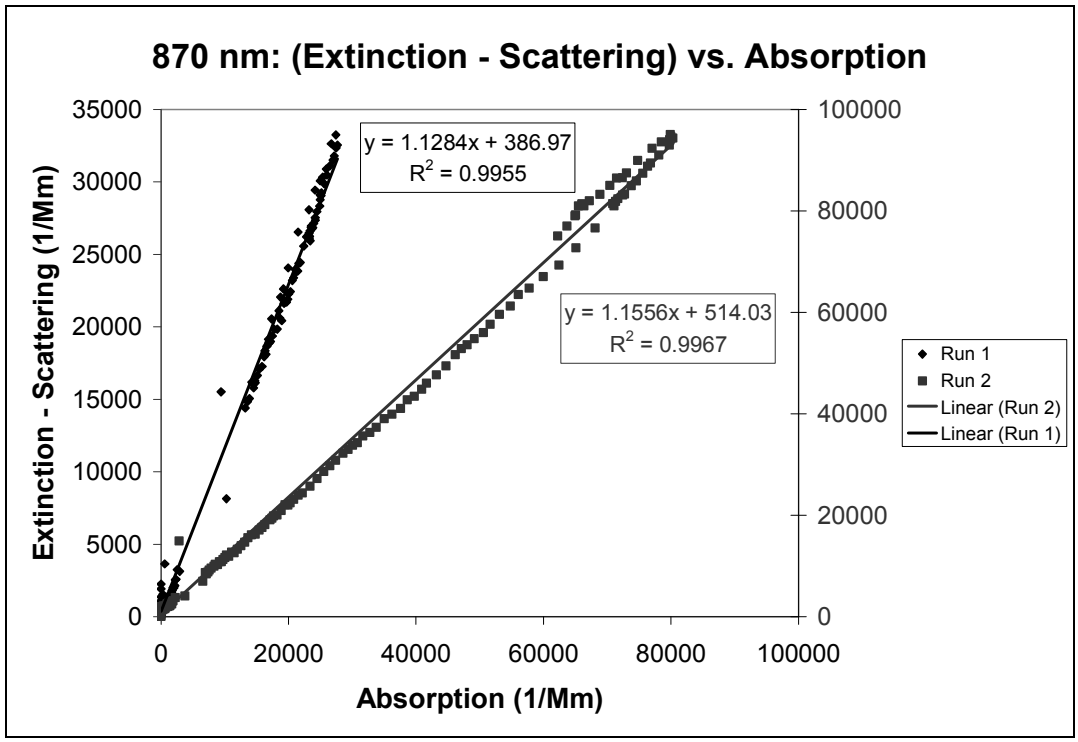

Figure 3.8b Kerosene-flame soot absorption calibration results for measurements at 870 nm; new scattering calibration factors applied to measured scattering coefficients

Figures 3.9a and 3.9b also present extinction minus scattering versus absorption for the two kerosene soot calibration runs at 405 nm and 870 nm, respectively. However, in Figures 3.9a and 3.9b the scattering calibration factor suggested by the salt calibration has not been applied to the measured scattering coefficients. Previously determined scattering calibration factors are used instead. Without the new scattering calibration applied, lesser changes are indicated by the kerosene-soot calibration to be made to absorption measurements. Calibration results for absorption coefficients measured at 405 nm indicate that absorption is overestimated by 3% to 4%, as shown in Figure 3.9a. The results from Figure 3.9b indicate that 870 nm absorption coefficients are underestimated by 6% to 7%. The differences in calibration for light absorption as depicted in Figures 3.8 and 3.9 are due to scattering calibration measurement differences. Particle morphology and composition affect the angular truncation errors in scattering measurements (Moosmüller and Arnott, 2003). Scattering contributes less than 30% to extinction for kerosene soot, so that uncertainties in scattering calibration are not emphasized. Uncertainties of plus or minus 15% for aerosol light absorption from various instruments and methods were also found during the Reno Aerosol Optics Study (Sheridan et al., 2005).

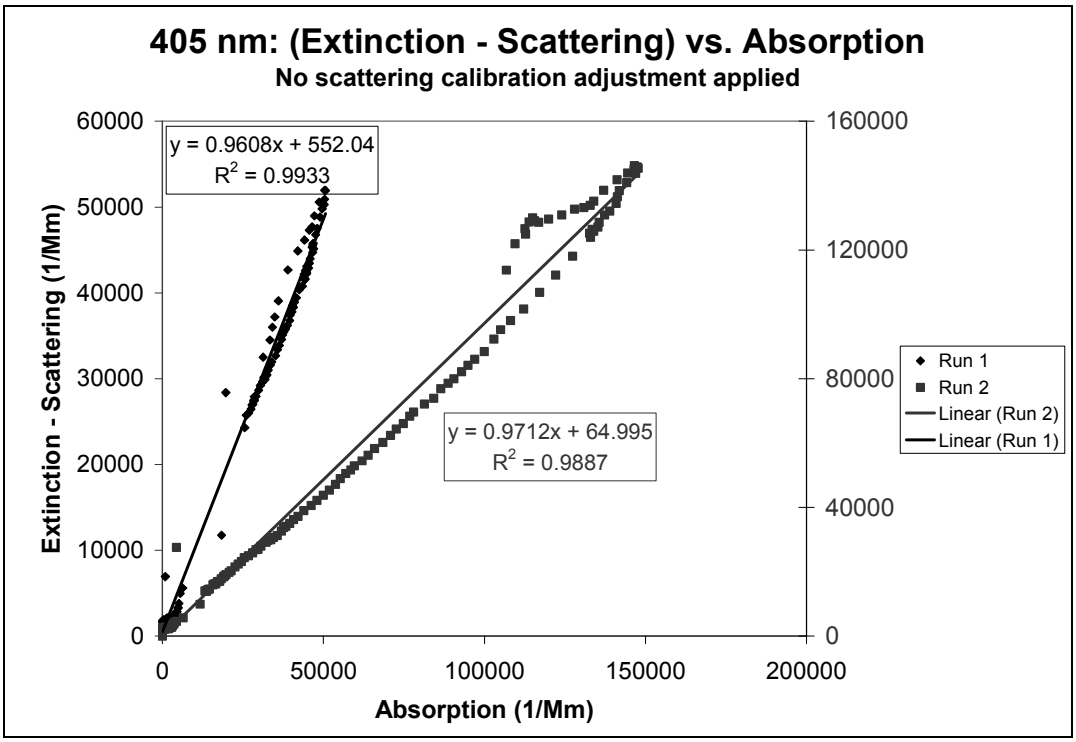

Figure 3.9a Kerosene-flame soot absorption calibration results for measurements at 405 nm; new scattering calibration factors not applied to results

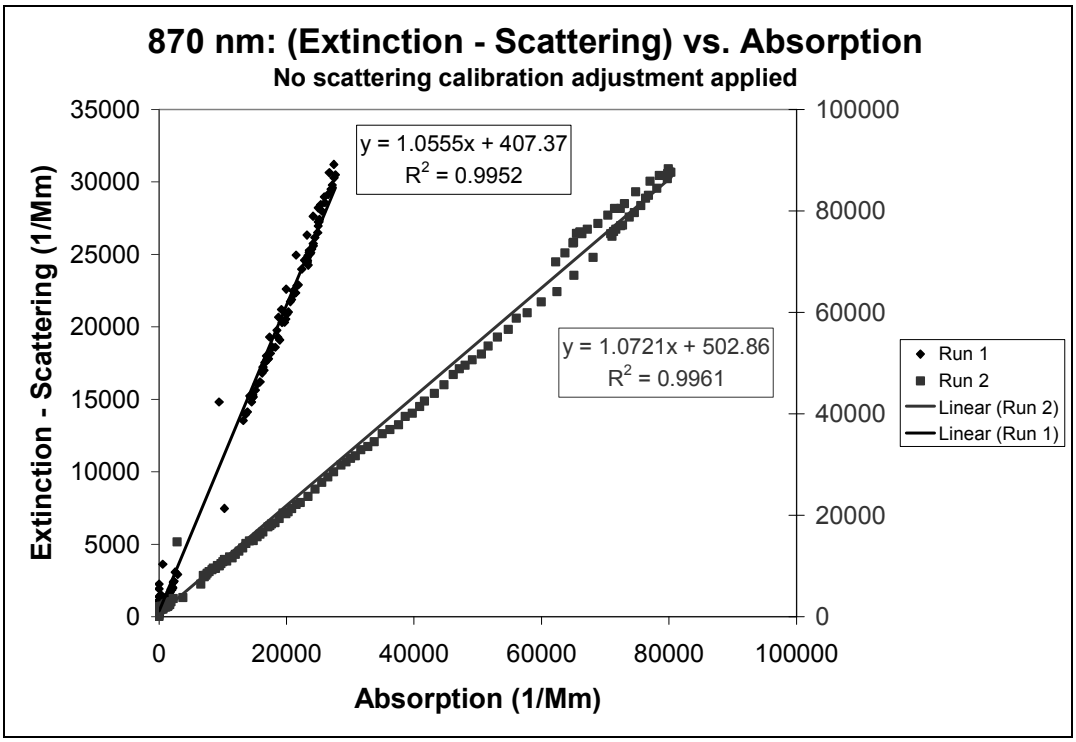

Figure 3.9b Kerosene-flame soot absorption calibration results for measurements at 870 nm; new scattering calibration factors not applied to results

A parameter which gives the relative level of scattering versus absorption can be calculated for kerosene-flame soot in order to confirm that optical properties of the soot aerosol during calibration are reasonable. Single scattering albedo, ω, is the ratio of scattering coefficient to extinction coefficient. Single scattering albedo is calculated from absorption coefficient β_{abs} and scattering coefficient β_{sca} at each wavelength independently as follows

$$\omega \equiv \frac{\beta_{sca}}{\beta_{extinction}} = \frac{\beta_{sca}}{\beta_{sca} + \beta_{abs}}. \qquad \text{(Eq. 3.4)}$$

A value of ω near unity would indicate that the aerosol is highly scattering, while a low value of ω (less than 0.5) would indicate that the majority of extinction by the aerosol is due to absorption. The parameter single scattering albedo and its implications for aerosol optical properties will be discussed further in Chapter 4.

Single scattering albedo is calculated from absorption and scattering measurements made during the kerosene-flame soot calibration runs. Time series measurements of ω for Run 1 and Run 2 at both radiation wavelengths are shown in Figure 3.10. Kerosene-flame soot is a very dark, highly absorbing aerosol, as expected. The average value for ω at 405 nm is approximately 0.22. At 870 nm the results in Figure 3.10 indicate that ω is equal to approximately 0.10. The variations in ω likely reflect the varying conditions of the kerosene soot flame and the associated particle size distribution.

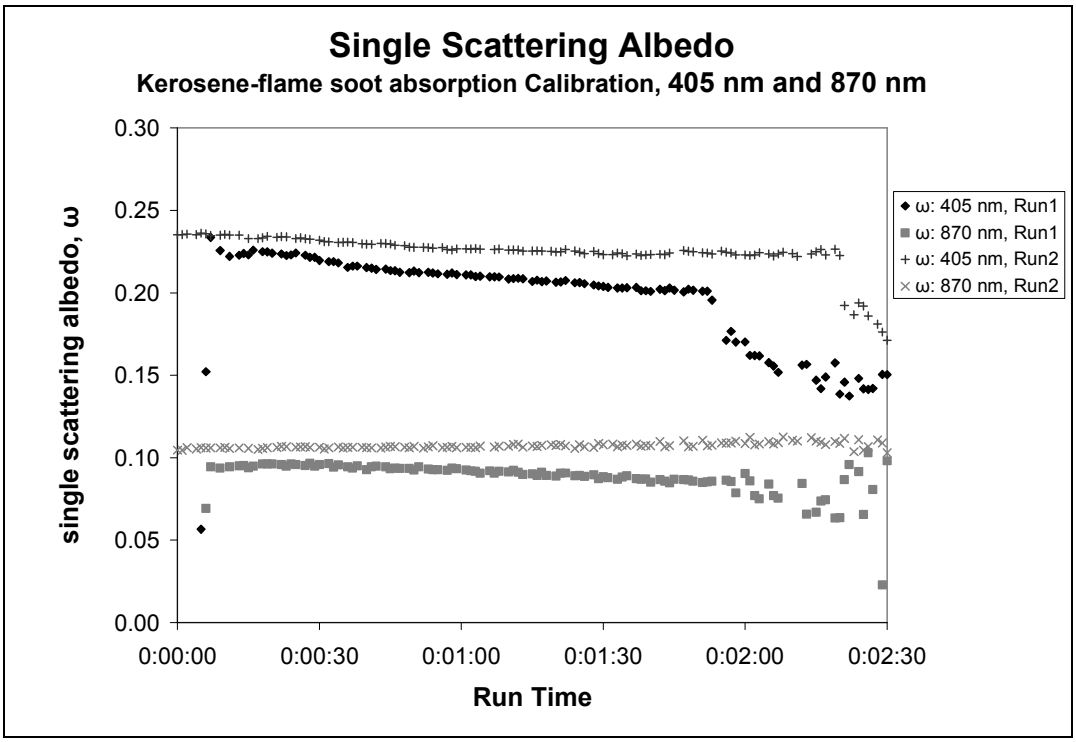

Figure 3.10 Time series calculations of ω at 405 nm and 870 nm for kerosene-flame soot absorption calibration runs

3.5 Discussion

The results from the aerosol calibrations of the dual-wavelength photoacoustic instrument indicate that scattering coefficients measured by the instrument are less than 30% or 40% below what is expected due to calculated extinction. Measured absorption coefficients by the instrument are more accurate: within 10% or 20% of expected values. The 405 nm absorption calibration indicated by the NO_2 gas calibration provides that an increase of 30% needs to be made to the measured absorption coefficients. This calibration factor is suspect, however, due to possible photodissociation of the NO_2 molecules at the radiation wavelength of 405 nm.

The calibration method is simple to perform, and it is powerful in the afforded ability to compare independent measurements of extinction with absorption and

scattering coefficients. The method, however, has limits and uncertainties that make "perfect" calibration impossible to achieve. A large uncertainty exists in the NO_2 gas calibration of absorption at 405 nm due the unknown level of photodissociation at that wavelength. Non-idealities in the instrument's scattering measurement provide another challenge in calibration. The angular and wavelength non-idealities inherent in scattering measurements made using reciprocal or typical nephelometry, as discussed in Chapter 1, introduce uncertainties into scattering measurements. The effects of the non-idealities, such as truncation angle of measured scattering volume, are dependent on aerosol scattering properties and single scattering albedo. Therefore these effects are not uniform for all particles. By applying the scattering calibration factor obtained from the salt calibration to scattering coefficients measured during kerosene soot calibration one is assuming the same scattering properties for the strongly absorbing aerosol as for the "white" scattering aerosol. Aerosol size differences and variations in imaginary refractive index will also influence the optical properties and, therefore, the calibration factors determined using this calibration method. (The imaginary refractive index of a particle determines absorption properties). In addition, the concentration of scattering aerosol must fall within the dynamic range for measurement that results in a linear relationship between particle scatter and its measurement. Multiple scattering and light attenuation are not accounted for in the calibration theory but may affect the measurements, particularly under concentration levels that have exceeded the instrument's ideal range. A more sensitive extinction measurement would improve dynamic range calibration errors. If a more sensitive means of measuring extinction existed for calibration of the

instrument such high aerosol concentrations would not be necessary to obtain an observable drop in laser power.

These particle calibrations exercise the instrument through a wide range of expected operating conditions. By comparison, gaseous calibration alone for scattering typically in use today still leaves much unfinished work, in that particle size and composition-dependent corrections have to be used as well (Anderson et al., 1996; Anderson and Ogren, 1998).

3.6 References

Anderson, T. L., Covert, D. S., Marshall, S. F., Laucks, M. L., Charlson, R. J., Waggoner, A. P., Ogren, J. A., Caldow, R., Holm, R. L., Quant, F. R., Sem, G. J., Wiedensohler, A., Ahlquist, N. A., and Bates, T. S. (1996). Performance characteristics of a high sensitivity, three wavelength, total scatter/backscatter nephelometer. *Journal of Atmospheric and Oceanic Technology* **13,** 967-986.

Anderson, T. L., and Ogren, J. A. (1998). Determining Aerosol Radiative Properties Using the TSI 3563 Integrating Nephelometer. *Aerosol Science and Technology* **29**(1)**,** 57-69.

Arnott, W. P., Moosmüller, H., and Walker, J. W. (2000). Nitrogen dioxide and kerosene-flame soot calibration of photoacoustic instruments for measurement of light absorption by aerosols. *Review of Scientific Instruments* **71**(7)**,** 4545-4552.

Moosmüller, H., and Arnott, W. P. (2003). Angular truncation errors in integrating nephelometry. *Review of scientific instruments* **74**(7)**,** 10.

Sheridan, P. J., Arnott, W. P., Ogren, J. A., Anderson, B. E., Atkinson, D. B., Covert, D. S., Moosmuller, H., Petzold, A., Schmid, B., Strawa, A. W., Varma, R., and Virkkula, A. (2005). The Reno aerosol optics study: An Evaluation of Aerosol Absorption Measurement Methods. *Aerosol Science & Technology* **39,** 1-16.

4 Measurement of Wood Smoke Optical Properties

4.1 Introduction

A campaign to measure wood smoke properties which took place in the spring of 2006 at the Forest Service's Fire Sciences Laboratory in Missoula, Montana provided an opportunity for evaluation and operation of the dual-wavelength photoacoustic instrument. It was employed along with a number of other instruments to measure optical, chemical, and morphological properties of smoke from a variety of biomass fuels. Use of the dual-wavelength instrument along with additional single-wavelength photoacoustic instruments allowed for analysis of the spectral dependence of absorption and scattering by the different fuel types. Variation of absorption and scattering with wavelength was found to allow for differentiation of fuel type according to optical properties of the wood smoke. Comparison with absorption and scattering measurements from other instruments, including the Magee Scientific seven-wavelength Aethalometer and the TSI three-wavelength integrating nephelometer, provide additional and confirming results on wood smoke spectral properties.

This chapter begins with a description of the motivation and scope of the Fire Lab at Missoula Experiment (FLAME), including instrumentation, experimental set-up and method, as well as a description of the vegetative fuels that were burned. Single scattering albedo and the Ångström exponent, parameters to quantify absorption and scattering at different wavelengths, are defined and reviewed. Aethalometer and nephelometer data from two representative burns is presented, followed by results from photoacoustic measurements depicting the spectral variation of absorption and scattering

among the different fuel types. A discussion of photoacoustic measurements in light of particle composition and morphology will lead to conclusions that can be drawn from the findings.

4.2 Fire Lab at Missoula Experiment (FLAME)

The Fire Lab at Missoula Experiment (FLAME), which took place during May and June of 2006, was concerned with air quality assessments proposed by the Joint Fire Science Program. The underlying motivation is to determine the contribution of biomass burning to $PM_{2.5}$ (airborne particulate matter with an aerodynamic diameter less than 2.5 microns) and visibility to support the needs of policy makers and wildland fire managers. In particular, the project is aimed at filling certain gaps in information and available tools needed for air quality assessments. Federal land managers and policy makers are in need of analytical techniques and composition reports that allow for differentiation of carbonaceous aerosols which originate from biomass burning versus those from mobile or industrial sources. Also needed is a greater understanding of the optical properties of fire emissions, as well as optical property emission rates and measurement-based particulate matter (PM) emission rates for relevant combustion conditions and fuels. To serve these objectives FLAME 2006 was the first of two campaigns conducted at the Fire Sciences Lab in Missoula, Montana which involve laboratory measurements of smoke emission composition profiles from several important fuel types. Emission rates and critical optical and physical properties of the wood smoke were also measured in the laboratory setting. The project includes cooperation by a number of organizations and groups including representatives from the US Forest Service, the National Park Service,

the Desert Research Institute of Reno, NV, Colorado State University, Aerodyne Research, Inc. of Billerica, MA, the Environmental Protection Agency of Utah, Los Alamos National Laboratory, Pacific Northwest National Laboratory, and the University of Nevada, Reno.

A multitude of varying instrumentation was employed during the FLAME 2006 campaign to measure optical, chemical, and physical properties of fire emissions. Only those instruments relevant to this discussion will be mentioned here. Optical aerosol properties were measured by six photoacoustic instruments, including a single-wavelength photoacoustic operating at 532 nm and the dual-wavelength instrument described in Chapter 2. Two seven-wavelength Aethalometers manufactured by Magee Scientific and a TSI three-wavelength integrating nephelometer were also used to assess light absorption and scattering. The Aethalometers measure light attenuation through a loading filter to determine black carbon mass concentration at the following wavelengths: 370, 450, 571, 615, 660, 880, and 950 nm. The TSI nephelometer measures light scattering by a suspended aerosol sample at center wavelengths of 450, 550 and 700 nm and bandwidths of 40 nm. Particle morphology was determined in part by use of a scanning electron microscope (SEM) to image particles impacted using a Time-Resolved Aerosol Collector (TRAC). Chemical composition of the wood smoke was analyzed using a number of methods. The fraction of organic material to inorganic components was determined using an Interagency Monitoring of Protected Visual Environments (IMPROVE) outdoor aerosol filter sampler with analysis by the IMPROVE method.

The experimental set up for the chamber burns is depicted in Figure 4.1. For each of the 19 chamber burns 200 grams of fuel were ignited on a flame bed. The smoke from

these fires was allowed to fill the large chamber, from which two main sample lines drew air using vacuum pumps to instrumentation located in separate rooms. Sample lines to individual instruments branched off from the primary lines. The sample time for each burn was approximately two hours, although the smoke from the last burn of the day was measured overnight. In addition, three hour-long measurements were made by the filter-based instruments of the "clean" chamber after it had been emptied of smoke remnants for background or "dynamic blank" filter samples.

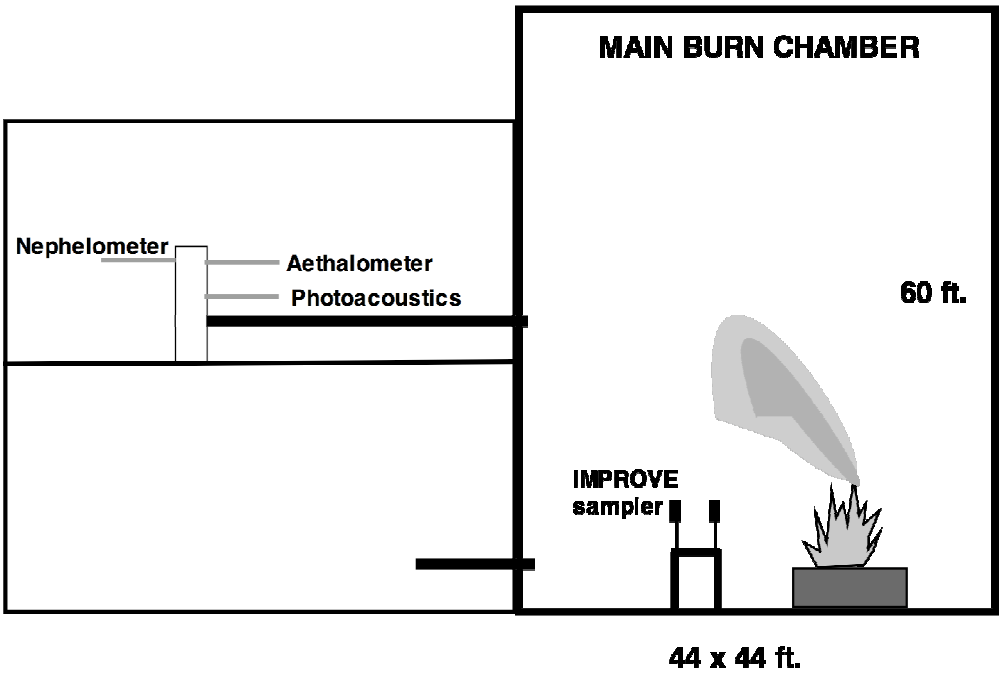

Figure 4.1 FLAME chamber burn experimental set-up. Only instrumentation relevant to this discussion is pictured

The majority of fuels that were burned during the chamber burns are native to the United States and are thought to be representative of wildfire activity in different parts of the country. The 16 fuel types are listed in Table 4.1. Two of these fuels are not discussed in this analysis, including lignin because it is not a biomass fuel but a filter material, and Puerto Rico mixed woods due to sampling errors that rendered

photoacoustic data from that burn unreliable. The fuels have been characterized based on vegetation type, with the primary divisions being between coniferous and deciduous flowering plants. Other fuel types include the duffs and those that are more difficult to group, including the fern (not a seed plant) and other miscellaneous flowering plants. The burn letter refers to the chamber burn label given to each separate burn. Ponderosa pine and chamise burns have multiple labels because those fuels were burned in the chamber two and three times each, respectively.

Fuel	Fuel Characterization	Burn (Label)
Ponderosa Pine, dried needles and sticks	conifer (pine)	A, C
Lodge pole Pine, needles and twigs	conifer (pine)	L
Utah Juniper, foliage and sticks	conifer (pine)	I
Southern Pine, needles	conifer (pine)	P
Ponderosa Pine duff	duff (pine)	F
Alaskan duff (feather moss)	duff	G
Southern California Manzanita	flowering shrub	H
Southern California Chamise	flowering shrub	B, D, N
Southeastern Wax Myrtle	flowering shrub	O
Utah Sage and Rabbitbrush, foliage and sticks	flowering shrub	J
Southern California Ceanothus	flowering shrub	S
Southeastern US Palmetto, leaves	miscellaneous flowering plant	R
Asian Rice Straw (Taiwan)	miscellaneous flowering plant	E
Puerto Rico Fern	fern	M
(Puerto Rico mixed woods)		Q
(Lignin)		K

Table 4.1 Fuel listing and classification for the 19 chamber burns conducted during FLAME 2006

4.3 Radiative Property Parameters

Light absorbing carbon particles, often called black carbon (BC) are the most abundant and efficient light absorbing components in the atmosphere in the visible spectrum. Such particles are emitted due to incomplete combustion of carbon-based fuels such as from industrial processes, motor vehicles or biomass burning. Light absorbing carbon aerosol has been found by modeling simulations to be an important factor in the radiative balance of the planet and climate forcing (Jacobson, 2001). Solar radiation is absorbed by the particles, warming the atmosphere and cooling the earth's surface. Reduction in the uncertainties of light absorbing carbon representations, particularly aerosol optical properties, is needed to improve the accuracy of climate models.

Measurements of light absorption by atmospheric particles are often made at a single wavelength. Absorption at additional solar wavelengths is then extrapolated assuming a power-law relationship between aerosol absorption coefficient, β_{abs}, and radiation wavelength, λ:

$$\beta_{abs} = a\lambda^{-b}. \qquad \text{(Eq. 4.1)}$$

Here a is a constant and b is the Ångström exponent of absorption. Absorption of visible radiation by BC is generally thought to have an inverse relationship to wavelength, or $\beta_{abs} \sim \lambda^{-1}$. An Ångström exponent of one implies a wavelength-independent refractive index for BC and "small" particle size (Bergstrom, Russell, and Hignett, 2002). Particles from diesel combustion have been shown to display a weak wavelength dependence on absorption, with b equal to approximately one (Schnaiter et al., 2003). A stronger spectral dependence on absorption, characterized by Ångström exponent values greater than 1, has been found for other aerosol species. The increased Ångström exponent

values result from stronger absorption at shorter wavelengths. Particles emitted from low-temperature combustion of coal (Bond, 2001) and lignite (Bond et al., 1999b) exhibit absorption with a strong wavelength dependence. Smoldering combustion of pine needles also produces non-BC particulate matter with a strong spectral dependence on absorption (Patterson and McMahon, 1984). Organic carbon (OC) components of aerosol exhibit enhanced absorption at wavelengths shorter than 600 nm. Recently, Kirchstetter et al. (2004) used a filter-based method to measure aerosol light absorption for particles from biomass and motor vehicle combustion. The researchers found light absorption by aerosols from motor vehicles varied approximately as λ^{-1}, as expected for BC-dominated particles. However, an Ångström exponent of approximately $b = 2$ was found to be the most appropriate spectral model for biomass smoke aerosols. This stronger spectral dependence was strongly diminished when OC was extracted from the biomass smoke aerosol samples. Ångström exponents between 2.2 and 3.5 were also deduced for aerosols from propane combustion with high OC content (Schnaiter et al., 2006). The presence of OC components in optically relevant quantities in wood smoke aerosols during FLAME produced increased Ångström exponents for certain fuel types, as demonstrated in Section 4.4. The spectral dependence of light absorption in this chapter is parameterized using Ångström exponent b.

The ratio of the scattering coefficient, β_{sca}, to the extinction coefficient, β_{ext}, is defined as single-scattering albedo, ω, where the extinction coefficient is the sum of absorption and scattering coefficients,

$$\omega \equiv \frac{\beta_{sca}}{\beta_{ext}} = \frac{\beta_{sca}}{\beta_{abs} + \beta_{sca}}. \qquad \text{(Eq. 4.2)}$$

The value for ω can extend between zero and one and is determined at a single wavelength. Single scattering albedo is normally a function of wavelength, and affects radiative transfer in a scattering medium. A "dark" aerosol with low single scattering albedo (e.g. less than 0.5) as is assumed to have a primarily warming effect on the atmosphere, while a "white" aerosol with a high single scattering albedo (e.g. greater than 0.85) is highly scattering and tends to have a cooling effect. An example of an aerosol with low ω is diesel soot (Schnaiter et al., 2003), while sulfate aerosols are highly scattering and thought to cool the atmosphere (Houghton et al., 2001). The heating and cooling consequence of single scattering albedo is at best an estimate, and in no way a means to deduce climate forcing as a fundamental property of the aerosol. (Forcing refers to the net temperature effect an atmospheric component has on climate. Positive radiative forcing tends on average to have a warming effect, and negative forcing tends on average to cool.) Too many additional radiation factors exist in ascertaining the forcing effect of an aerosol to allow conclusive determination from single scattering albedo alone, including surface albedo, solar zenith angle, and effects at infrared wavelengths. However, ω is a very useful qualitative parameter in estimating whether a sample is primarily absorbing (warming) or scattering (cooling). Single scattering albedo for each of the different wood smoke aerosols is presented in the next section of this chapter at wavelengths of 405 and 532 nm.

4.4 Results

4.4.1 Aethalometer and Photoacoustic Analysis

Photoacoustic absorption measurements can be compared to measurements made by the more ubiquitous Aethalometer (Magee Scientific, Berkeley, CA). Light absorption measurements by the dual-wavelength photoacoustic instrument correspond to and supplement the more common instrumentation. Measurements of light absorption, calculated from the change in attenuation of light transmission through a loading filter, *[ΔATN],* are converted by the Aethalometer into quantities of black carbon mass concentration. Black carbon mass concentration, *[BC]*, in units of mass per volume is determined using the formula

$$[BC] = \frac{[\Delta ATN]}{\sigma}\frac{A}{F\Delta t}. \qquad \text{(Eq. 4.3)}$$

The absorption efficiency in units of area per mass is given by σ. F is the volumetric flow rate, A is the sample area over which particulate matter is deposited on the filter, and Δt is the measurement interval (typically two minutes). The manufacturer's calibration assumes that all absorption of light is accomplished by black carbon. A more descriptive term for the reported Aethalometer measurement, as proposed by Andrea et al. (2006), is "equivalent black carbon" concentration, or the amount of BC that would produce the same signal as the measurement.

Absorption efficiency is taken to be a function of inverse wavelength: $\sigma(1/\lambda)$. A model AE-31 "Spectrum" Aethalometer was used during FLAME 2006, which reports black carbon mass concentration at seven wavelengths: 370, 450, 570, 615, 660, 880, and 950 nm. Determination of *[BC]* at each wavelength is achieved by using an absorption

efficiency for BC at a visible wavelength, and extrapolating this value to other wavelengths assuming inverse wavelength dependence. For example, the absorption efficiency at 450 nm for BC is almost twice that at 880 nm. Light absorption measurements by the dual-wavelength photoacoustic instrument are calibrated directly as light absorption values and are reported in units of inverse distance, typically inverse megameters (Mm^{-1}).

The variation with time of equivalent black carbon mass concentration measured by three channels of the Aethalometer is presented along with light absorption measurements by the dual-wavelength photoacoustic instrument in Figures 4.2 and 4.3. Figure 4.2 exhibits results from burn D of Southern California chamise fuel, and Figure 4.3 is burn E of Asian rice straw. Chamise and rice straw fuels are presented repeatedly as examples in this chapter because they are representative of diverse aerosols with very different optical properties. The left axis of the figures reports the level of equivalent BC mass concentration, and the right axis refers to the photoacoustic light absorption. Aethalometer transmission wavelengths of 370, 470, and 880 nm are chosen here because they are most representative of the operational wavelengths of the photoacoustic instrument. The gaps in the Aethalometer data are associated with filter changes. The sharply declining "ski slope" behavior comes about because Aethalometer calibration is not based on filter loading. Aethalometers have been found to over predict BC concentration on a fresh filter and under predict it on a loaded filter (Arnott et al., 2005). Figures 4.2 and 4.3 are presented in part to depict the shortcomings of Aethalometer measurements, especially in light of photoacoustic measurements of the same data. The light absorption signal from the dual-wavelength instrument is without the gaps and

sloping behavior of BC mass concentration data, and no assumptions are made regarding absorption efficiency or spectral response of the sample in instrument calibration. Notice that the slight declining trend of the central Aethalometer signal is present in the photoacoustic data as well.

Figure 4.2 depicts aerosol data from a burn of chamise fuel. Chamise is a U.S. native flowering shrub that grows in California and Nevada. Chamise smoke is a very dark aerosol: single scattering albedo at 405 nm is 0.40 as determined by photoacoustic data. The BC mass concentration reported by the Aethalometer nearly overlaps at the different wavelengths, indicating very little spectral variability in absorption properties for this fuel. The Aethalometer calibration assumption of light absorption strictly by BC results in an inverse wavelength dependence of absorption efficiency which is well represented by chamise smoke. The Ångström exponent of absorption calculated from Aethalometer measurements is near unity: $b = 1.07$.

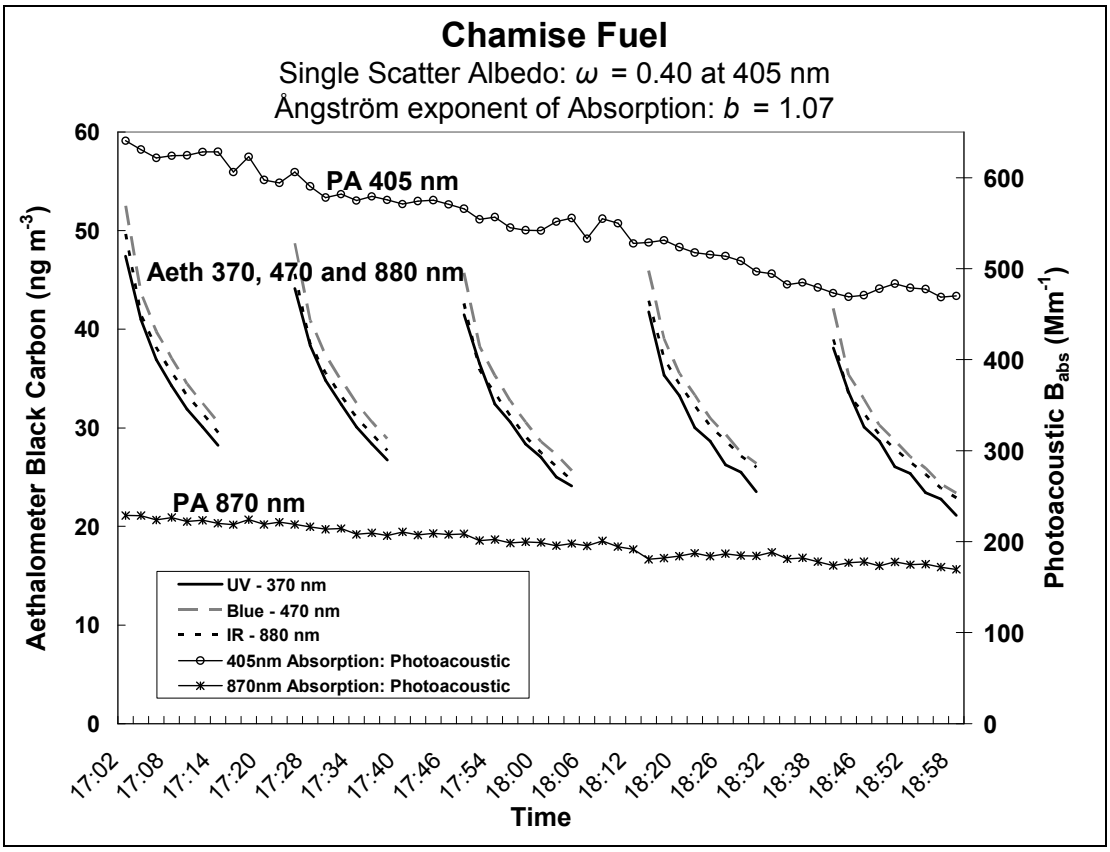

Figure 4.2 Aethalometer and dual-wavelength photoacoustic measurements for burn D: chamise fuel. Note the inverse dependence of absorption on wavelength ($\beta_{abs} \sim 1/\lambda$), characteristic of classical BC aerosol

Figure 4.3 depicts BC mass concentration and the photoacoustic absorption signal from burn E of Asian rice straw. Rice straw is a highly scattering fuel, with a single scattering albedo of $\omega = 0.88$ at 405 nm. In contrast to the chamise smoke, the mass concentration of equivalent BC as reported by the seven-wavelength Aethalometer does not overlap at the three depicted wavelength channels. Instead, considerably more BC is measured at shorter wavelengths indicating increased light absorption for higher energy radiation. A stronger wavelength dependence on absorption than $1/\lambda$ is needed to accurately represent the wavelength response of smoke from fuels like rice straw. Greater absorption at shorter-wavelength visible and ultraviolet radiation suggests the

substantial presence of non-BC components in the aerosol, such as organic materials, which preferentially absorb light at shorter wavelengths. The Ångström exponent for absorption, as calculated from Aethalometer data at 470 and 880 nm is b = 2.36.

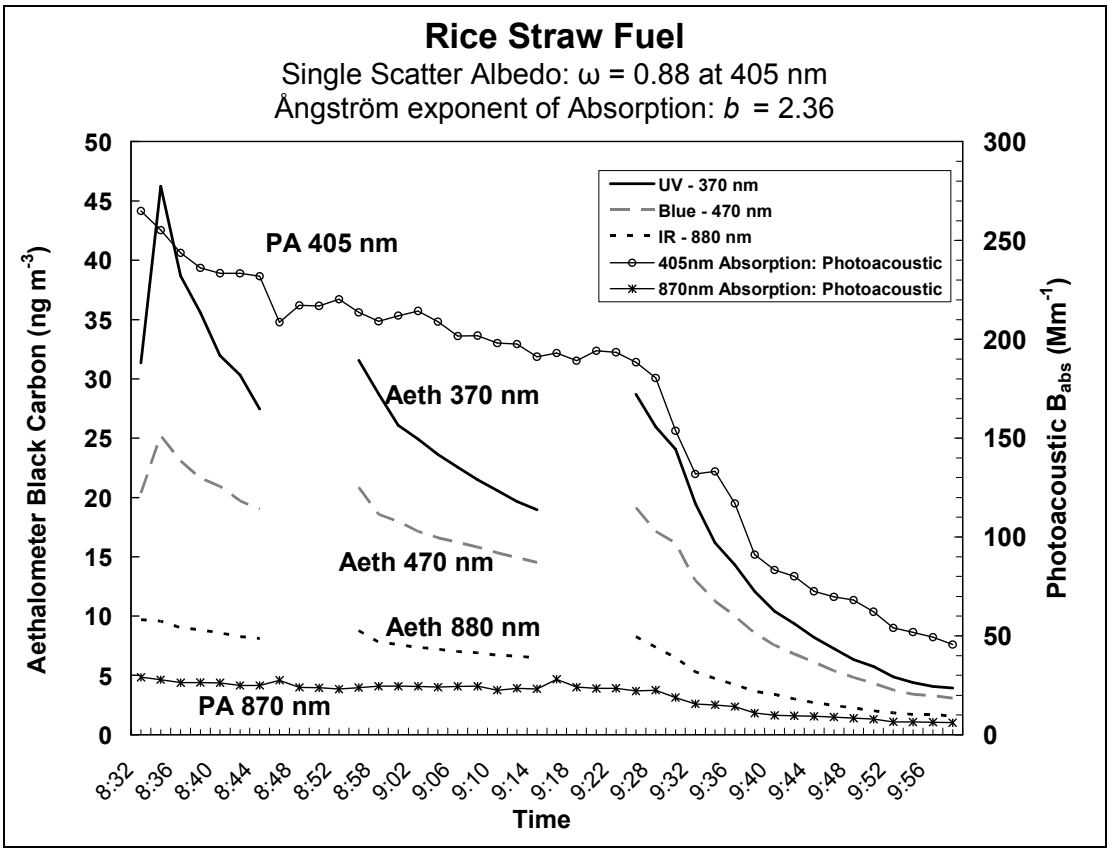

Figure 4.3 Aethalometer and dual-wavelength photoacoustic measurements for burn E: rice straw fuel. Note the significant spectral variation of light absorption and the Ångström exponent greater than one, indicating light absorbing organic aerosol components in rice straw fuel

4.4.2 Nephelometer and Photoacoustic Analysis

Photoacoustic measurements of light scattering by wood smoke can be evaluated along side measurements from the TSI integrating nephelometer. The nephelometer measures light scattering by suspended particles at three visible wavelengths: 450, 550 and 700 nm. Nephelometer data and the dual-wavelength photoacoustic instrument's

scattering measurements at 405 and 870 nm, along with scattering data from a single-wavelength instrument operating at 532, are presented in time series form for the same two burns analyzed in Section 4.4.1. Scattering measurements for chamise burn D and rice straw burn E are depicted in Figures 4.4 and 4.5, respectively. The nephelometer correction for angular nonidealities developed by Theodore L. Anderson and John A. Ogren (Anderson and Ogren, 1998) assuming sub-micron particles was applied to the nephelometer measurements shown in Figures 4.4 and 4.5.

At each wavelength scattering is almost twice as much for rice straw aerosol as it is for that from the chamise fuel. Recall that the single scattering albedo for rice straw at 405 nm is 0.88 while for chamise it is a very low 0.40. As expected for "small" sub-micron particles light scattering decreases with increasing incident wavelength. Comparison of photoacoustic scattering data with Nephelometer measurements in Figures 4.4 and 4.5 provides verification of photoacoustic instrument calibration and performance. Considerably more fluctuation is found in scattering measurements provided by the photoacoustics due to high scattering background on these instruments. Use of a multimode fiber coupling the PMT and cosine scattering sensor is likely another source of scattering measurement fluctuations. This problem is more pronounced for lower levels of light scattering, as with the smoke from the chamise burns. The estimated uncertainty in light scattering measurements by the photoacoustic instruments is plus or minus 100 Mm^{-1}. Photoacoustic measurements of both light scattering and absorption are averaged over an entire burn for determination of single scattering albedo and spectral analysis in the following sub-section of this chapter, so effects of measurement uncertainty are minimized.

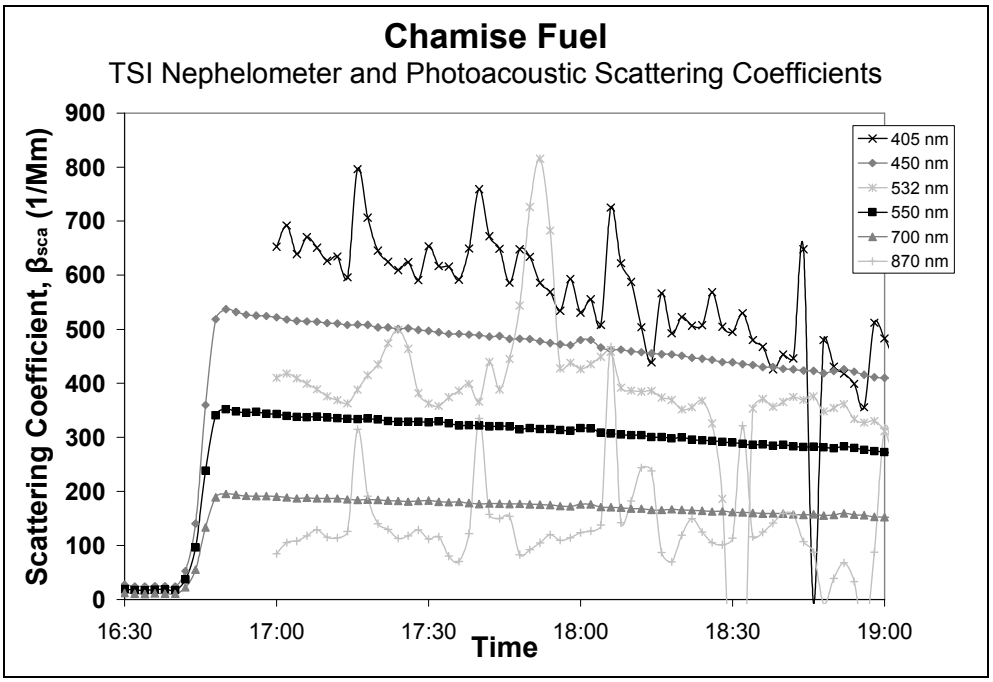

Figure 4.4 Measurements of aerosol light scattering during FLAME burn D of chamise fuel at six wavelengths by three instruments: two photoacoustic instruments and a TSI integrating nephelometer. Nephelometer measurements provided by the Missoula Fire Sciences Lab

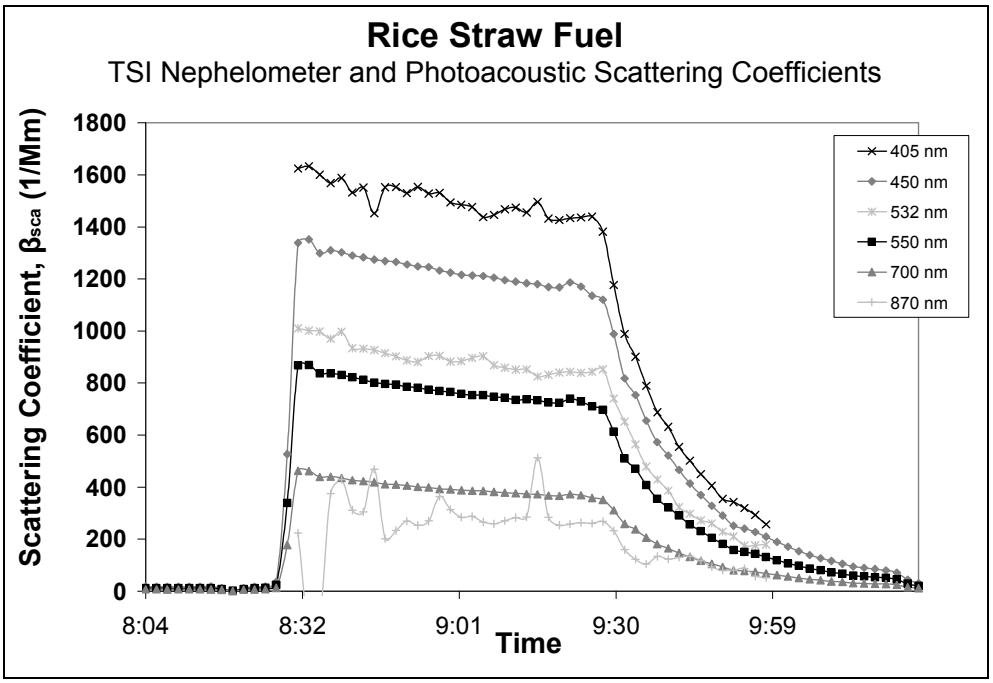

Figure 4.5 Measurements of aerosol light scattering during FLAME burn E of rice straw fuel at six wavelengths by three instruments: two photoacoustic instruments and TSI integrating nephelometer. Nephelometer measurements provided by the Missoula Fire Sciences Lab

4.4.3 Spectral Response by Fuel Type

The dependence of aerosol light absorption on wavelength is parameterized using the Ångström exponent of absorption, *b*. This parameter is calculated using β_{abs} measurements at two different wavelengths:

$$b\left(\lambda_1 / \lambda_2\right) = -\frac{\ln\left(\beta_{abs}(\lambda_1) / \beta_{abs}(\lambda_2)\right)}{\ln\left(\lambda_1 / \lambda_2\right)}, \qquad \text{(Eq. 4.4)}$$

where λ_1 and λ_2 represent two different radiation wavelengths, and $\beta_{abs}(\lambda_1)$ is the coefficient of absorption measured at λ_1. Spectral response is analyzed in light of single scattering albedo, ω. Recall that ω indicates the relative magnitude of scattering versus absorption of an aerosol, and is calculated at a single value of λ.

The Ångström exponent *b* and single scattering albedo results shown in Figures 4.6 and 4.7 are derived from photoacoustic measurements of light absorption and scattering from each of the FLAME burns. The data points represent *b* and ω values calculated from absorption and scattering coefficients averaged over a single two hour chamber burn. The results in Figures 4.6 and 4.7, excluding a few outliers, have been grouped and labeled according to fuel characterization. Fuel labels are also provided in the legend. The two figures have matching axes.

Figure 4.6 depicts Ångström exponents derived from absorption coefficients at 405 and 870 nm (*b(405/870)*) measured by the dual-wavelength photoacoustic instrument. The horizontal axis of Figure 4.6 presents average single scattering albedo values for each burn derived from photoacoustic measurements at 405 nm (ω*(405 nm)*). It is apparent from Figure 4.6 that those fuels which produce relatively "dark" aerosol

similar to chamise with ω values ranging from 0.37 to 0.5 also exhibit b values near unity. Such fuels exhibit optical properties of BC, and are very much like diesel soot. Fuels with higher single scattering albedos, particularly those above 0.75 (or corresponding to at least three times as much scattering as absorption by the particles) have Ångström exponents increasingly greater than one. Such fuels show increased absorption at shorter wavelengths. The optical properties of the highly scattering fuels are not well represented by the BC assumption of absorption efficiency that scales as $1/\lambda$. The Ångström exponent calculated from the rice straw burn is 2.8. This b value corresponds to an absorption ratio at wavelengths of 405 and 870 nm which is nearly four times that expected for inverse-wavelength dependence.

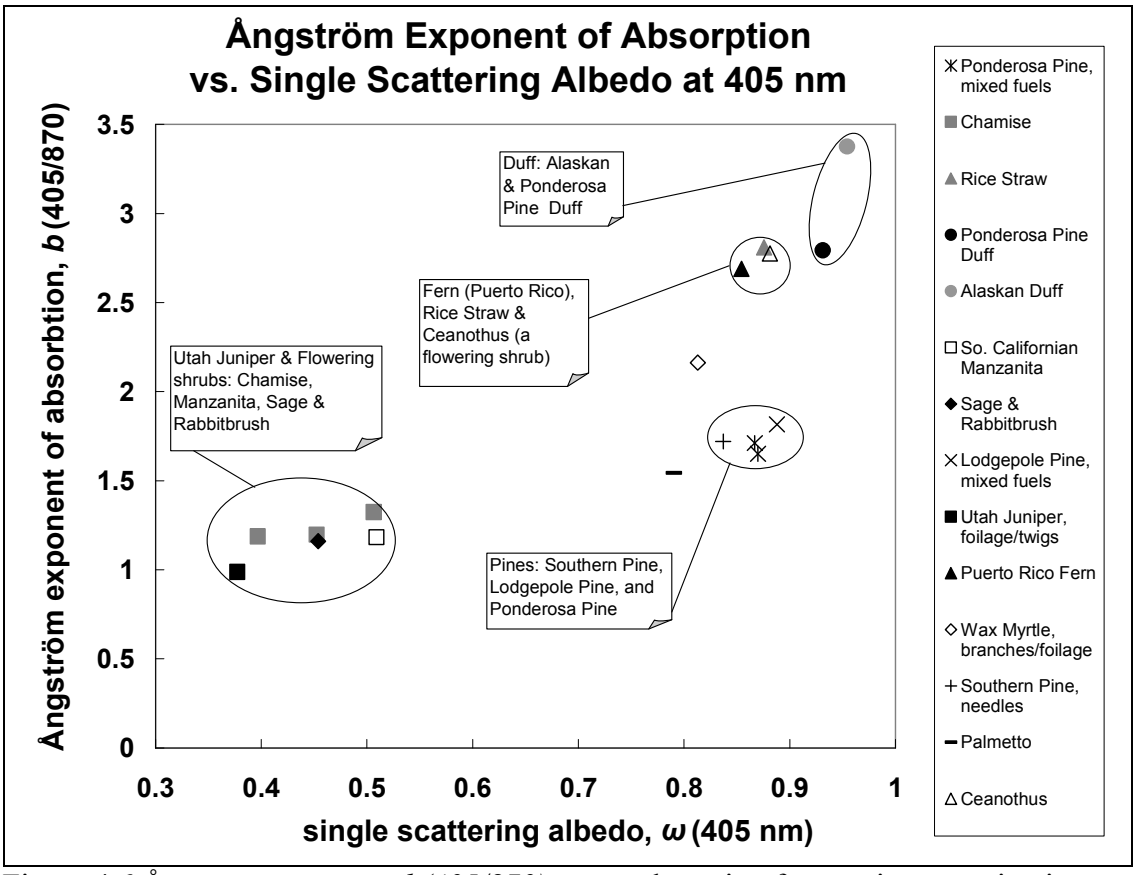

Figure 4.6 Ångström exponent *b(405/870)* versus the ratio of scattering to extinction at 405 nm by smoke from each burn, labeled by fuel type. Fuels with high ω also show increased *b* values and, therefore, a strong spectral dependence of absorption

Angstrom exponent *b* and ω values presented in Figure 4.7 were also determined using photoacoustic absorption and scattering at 532 and 870 nm. The same general trend present in Figure 4.6 is also apparent in Figure 4.7. Fuels producing "dark" aerosols are well represented by an inverse-wavelength absorption dependence model, while this model fails for certain other fuels with increased scattering and Ångström exponents greater than one. Increased *b* values for certain fuels indicate the smoke absorbs short-wavelength radiation much more efficiently. The range of Ångström exponents when determined by signals at 532 and 870 nm (*b(532/870)*) is not as great as that by signals at 405 and 870 nm. For example, for rice straw fuel *b(532/870)* = 2.0 and

recall *b(405/870)* = 2.8. This indicates much more absorption at the near-UV wavelength of 405 nm than of green radiation at 532 nm.

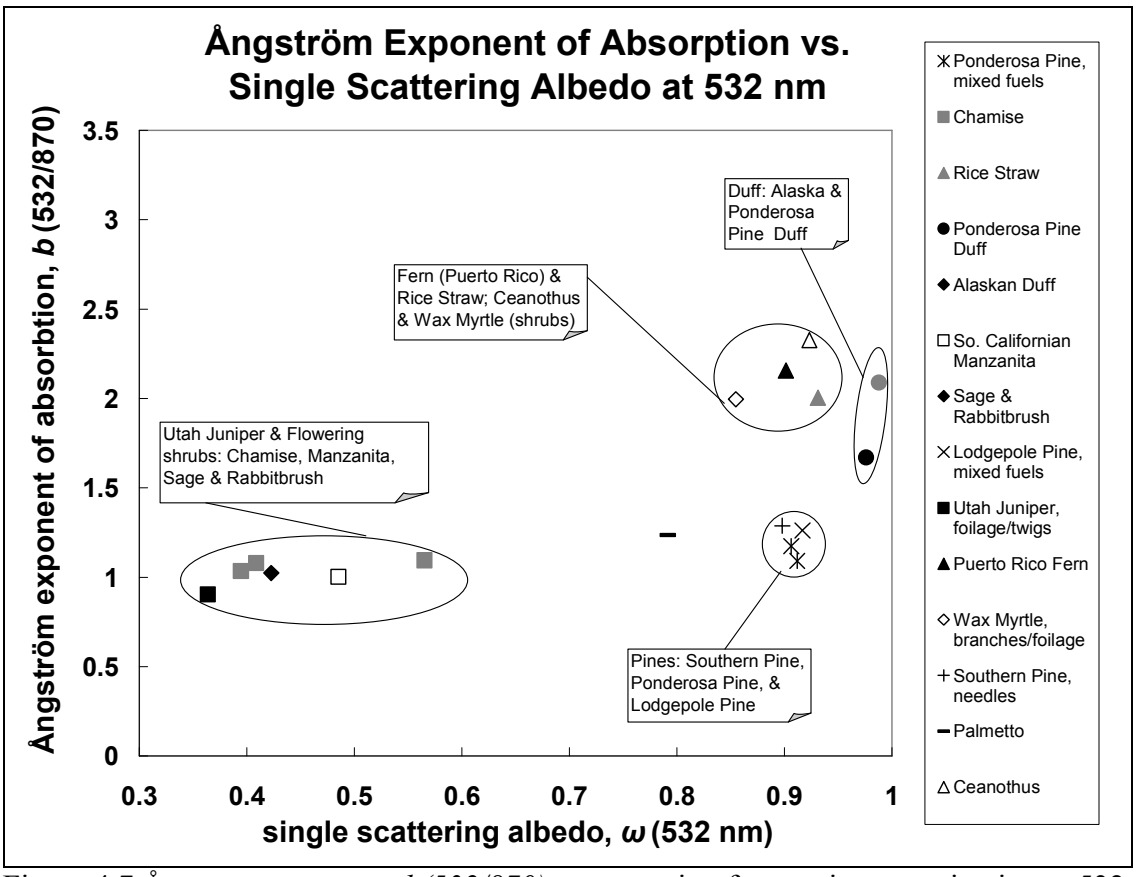

Figure 4.7 Ångström exponent *b(532/870)* versus ratio of scattering to extinction at 532 nm by smoke from each burn, labeled by fuel type. Certain fuels not well-represented by $\beta_{abs} \sim \lambda^{-1}$ assumption typically held for light absorbing BC aerosol

The results shown in Figures 4.6 and 4.7 suggest the presence of non-black carbon components that preferentially absorb light at shorter wavelengths in those fuels with *b* greater than one. Organic materials, which have been shown to strongly absorb radiation at wavelengths shorter than 600 nm (Kirchstetter, Novakov, and Hobbs, 2004), are postulated to be responsible for the increased absorption at shorter wavelengths resulting in increased *b* exponents. Analysis of fuel composition supports this assumption. Organic species are present in optically relevant quantities on the smoke

produced from certain fuels. These fuels are also generally much more scattering than typical BC-dominated aerosols. Assuming optical properties of BC for all light absorbing particulates will introduce large errors for many biomass aerosols due to the strong spectral dependence of absorption. Casual use of the inverse wavelength dependence, such as in remote sensing data, can result in errors as large as a factor of six in determining UV absorption and a factor of two in the visible when β_{abs} is extrapolated to shorter radiation wavelengths from a single near-IR absorption measurement.

Uncertainties in the photoacoustic absorption measurement not arising from calibration or operator error come about in measurement of those parameters that go into determination of β_{abs} (see the photoacoustic equation: Equation 1.1 in Chapter 1). Measurement of resonance frequency, f_o, resonator quality factor, Q, laser power, P_L, and microphone pressure, P_M, introduce uncertainties in measured absorption. The fractional uncertainty in β_{abs}, or the uncertainty in β_{abs} divided by the absolute value of β_{abs}, is the sum of fractional uncertainties in the measured quantities:

$$\frac{\delta\beta_{abs}}{|\beta_{abs}|} = \frac{\delta P_M}{|P_M|} + \frac{\delta P_L}{|P_L|} + \frac{\delta Q}{|Q|} + \frac{\delta f_o}{|f_o|}. \qquad \text{(Eq. 4.5)}$$

The fractional uncertainty in microphone pressure is equal to the measured noise of the absorption measurement divided by $|\beta_{abs}|$. When this value is averaged over an entire burn, as it is in the measurements presented in this section, the error in microphone pressure is very small, so that only the small uncertainties in P_L, f_o, and Q cause error in β_{abs}. A five percent uncertainty exists in the laser power measurement. Resonance frequency can be measured to within 0.2 Hz, and the uncertainty in resonator quality factor measurement is less than one. Assuming typical values of f_o and Q (1500 Hz and

72, respectively) the uncertainty in average absorption values is approximately 0.07 inverse megameters.

Extinction is the sum of light absorption and scattering. The percent of light extinction that is due to absorption versus that due to scattering for each FLAME chamber burn is depicted in Figures 4.8 and 4.9. Figure 4.8 includes average absorption and scattering for each burn measured by the 405 nm channel of the dual-wavelength photoacoustic instrument, while Figure 4.9 includes that from the 870 nm channel. For fuel types that produce aerosols with Ångström exponent *b* values greater than one a higher percentage of extinction is due to absorption at 405 nm than at 870 nm. Rice straw smoke provides an example of this phenomenon, as well as both ponderosa pine duff and Alaskan duff. For these three fuels, absorption makes up a greater percentage of total extinction at 405 nm. In contrast, fuels that produce darker, sootier aerosols with lower single scattering albedos, such as the flowering shrubs like chamise, manzanita, sage and rabbitbrush, exhibit a higher percentage of absorption at 870 nm compared to that at 405 nm. Such fuels scatter more strongly at the shorter wavelength, so that a larger fraction of extinction is due to scattering at 405 nm.

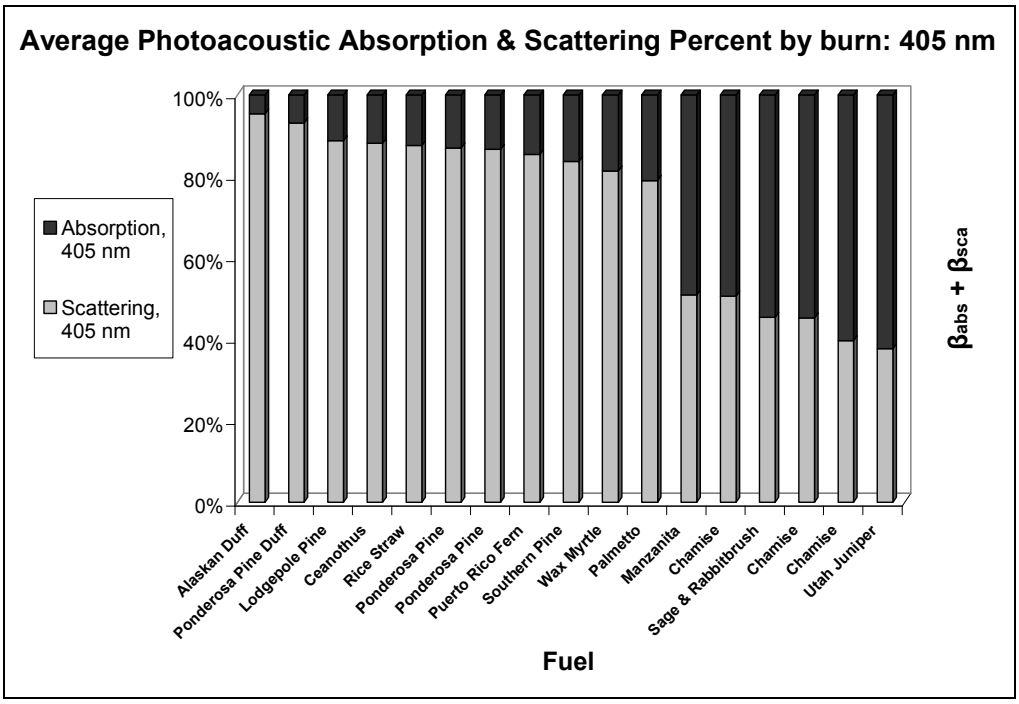

Figure 4.8 Absorption and scattering fractions of total extinction at 405 nm for each FLAME chamber burn as measured by the dual-wavelength photoacoustic instrument, labeled by fuel type

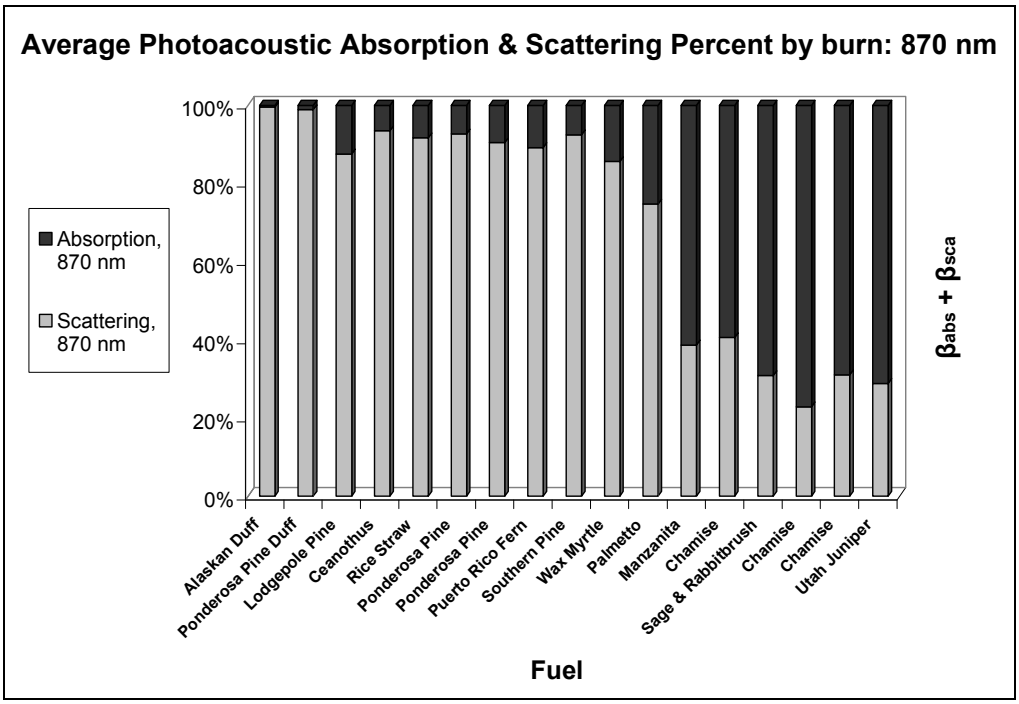

Figure 4.9 Absorption and scattering fractions of total extinction at 870 nm for each FLAME chamber burn as measured by the dual-wavelength photoacoustic instrument, labeled by fuel type

Mass concentration measurements of different chemical components comprising the aerosol from each fuel type are provided by the IMPROVE aerosol sampler which was present within the chamber during the FLAME burns. IMPROVE data is provided by FLAME collaborators from the Atmospheric Science Department at Colorado State University. The filter-based aerosol sampler is identical to those employed at over a hundred sites across the U.S. as part of the Interagency Monitoring of Protected Visual Environments (IMPROVE) program. The IMPROVE program assists the National Park Service and other federal land managers in protecting visibility at Class I areas, including most national parks and wilderness areas, in compliance with the Clean Air Act. IMPROVE aerosol samplers are used as part of this program for measurement of the concentration and composition of fine particulate matter, which contributes to optical extinction and contains tracers for identification of emission sources.

The standard IMPROVE sampler consists of four independent sampling modules, two of which are relevant to this analysis. Module B is for measurement of $PM_{2.5}$ particles on nylon filters. The nylon filters are analyzed by ion chromatography at Research Triangle Institute for nitrate, chloride, sulfate and nitrite. Nitrate vapors are removed prior to collection by a denuder, so that measured concentrations represent only particulate nitrate. Measured concentrations from module B represent the inorganic content of the aerosol sample.

Carbon concentration is found using module C, which measures $PM_{2.5}$ particles on quartz filters. The quartz filters are analyzed for carbon at the Desert Research Institute using the Thermal Optical Reflectance (TOR) combustion method. As described in the IMPROVE data guide on the IMPROVE website

(http://vista.cira.colostate.edu/improve/) the TOR combustion method proceeds as follows. Evolved CO_2 is measured as the sample on the quartz filter is heated in steps, and reflectance of the sample is monitored throughout the heating. The reflectance of the sample decreases at 120° C and then returns to the initial value during the 550° C step. It is also during the 550° C step that 2% oxygen (O_2) is added to the sample atmosphere, which prior to that was 100% helium. Each heating step produces a carbon fraction, referred to by number and as either organic or elemental: O1, O2, E1, etc. All carbon fractions measured before the return of initial reflectance are considered organic carbon, and all those measured after are elemental carbon. OP is the portion of an elemental carbon fraction before the reflectance returns to the initial value. The TOR method is summarized in Table 4.2, taken from the IMPROVE data guide.

Fraction	Pyrolized Fraction	Temperature Range	Atmosphere	Reflectance vs. Initial Reflectance
O1		ambient to 120 deg C		at initial
O2		120 - 250 deg C	100% He	under initial
O3		250 - 450 deg C		
O4		450 - 550 deg C		
E1	OP	remains at 550 deg C	98% He	over initial
E2		550 - 700 deg C	2% O_2	
E3		700 - 800 deg C		

Table 4.2 Summary of carbon components measured by the TOR combustion method as a function of temperature and added oxygen

The total organic carbon and total elemental carbon fractions are calculated as follows:

total organic carbon ≡ OC = O1 + O2 + O3 + O4 + OP, (Eq. 4.6)

total elemental carbon ≡ EC = E1 + E2 + E3 – OP. (Eq. 4.7)

The total inorganic mass concentration measured by module B is calculated for this analysis as:

total inorganic = $CL^- + NO_2^- + NO_3^- + SO_4^- + NA^+ + NH_4^+ + K^+ + Mg^+ + Ca^+$. (Eq. 4.8)

Measured ratios of total inorganic content, OC, and EC from the IMPROVE aerosol sampler for each of the FLAME chamber burns are shown in Figure 4.10. This figure reveals those fuel types with large fractions of elemental carbon components, such as chamise, manzanita, sage and rabbitbrush. For these fuels one would expect typical BC optical properties, including strong absorption characterized by weak wavelength dependence and low single scattering albedo. Such fuel types produce soot-like aerosols. In contrast, Figure 4.10 also depicts fuels that were shown to have high single scattering albedo values, like rice straw and ponderosa pine, are composed of high fractions of OC and inorganic components.

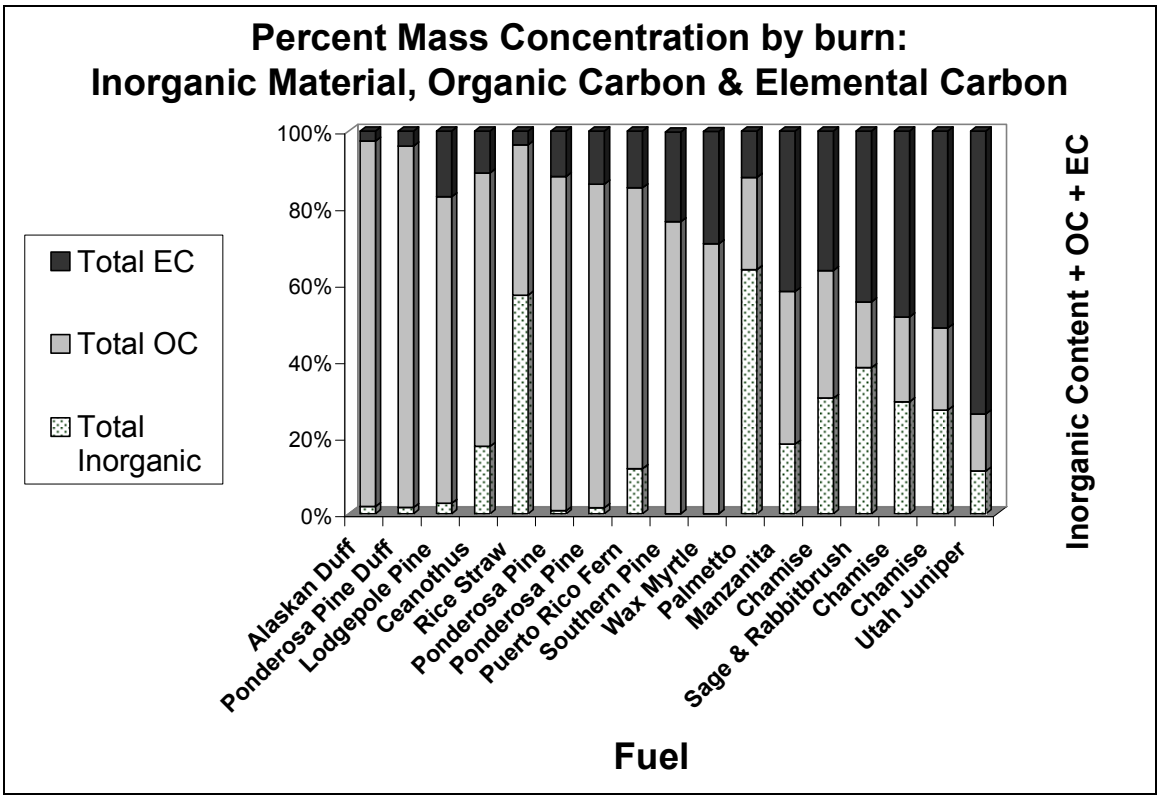

Figure 4.10 Mass concentration fractions of total elemental carbon, organic carbon and inorganic content for each fuel type for FLAME chamber burns, as measured by the IMPROVE aerosol sampler

Comparison of the mass concentration percentages in Figure 4.10 with absorption and scattering percentages at 870 nm in Figure 4.9 provides insight into the aerosol composition fractions responsible for optical properties. At 870 nm most of the light absorption by a sample is accomplished by the EC fraction, and light scattering is accomplished by the OC and inorganic components.

Images of aerosol particles from three representative fuels are shown in Figures 4.11, 4.12 and 4.13. The images and their analysis are provided by Yury Desyaterik and Alex Laskin of EMSL/PNNL (Environmental Molecular Sciences Laboratory/Pacific Northwest National Laboratory). The images are included here to illustrate the complexity of particle morphology and composition. A Time Resolved Aerosol

Collector (TRAC) was used to deposit 0.35 to 2.5 mm particles on Transmission Electron Microscope (TEM) grids every 10 minutes during the FLAME 2006 chamber burns. The TRAC is a one stage impactor for particle collection. Particles are then analyzed using Computer Controlled Scanning Electron Microscopy/Energy Dispersed X-ray (CCSEM/EDX) single-particle analysis. In CCSEM/EDX microanalysis a computer-controlled electron beam assails the particles, and the resulting X-ray fluorescence is observed by an EDX spectrometer (Laskin, Iedema, and Cowin, 2003).

The images presented in Figures 4.11, 4.12 and 4.13 are aerosol particles from chamise, ponderosa pine, and rice straw fuels, respectively. These three are chosen as representative fuel types based on composition and resulting optical properties. Flowering shrubs, such as chamise, manzanita, sage and rabbitbrush, produce typical soot-chain aerosol particles with low single scattering albedos. The pines, including ponderosa, lodgepole and southern pine, are dominated by organic particulate matter, and are more highly scattering than typical soot particles. Aerosol from rice straw fuel shows almost no soot particles, with high concentrations of inorganic components as crystalline particles mixed with organic materials. Fuels with similar composition and optical properties to those of rice straw include palmetto and ceanothus. Observations of aerosol composition from CCSEM/EDX analysis of the samples, as reported by researchers Desyaterik and Laskin, are included in the captions of Figures 4.11, 4.12, and 4.13.

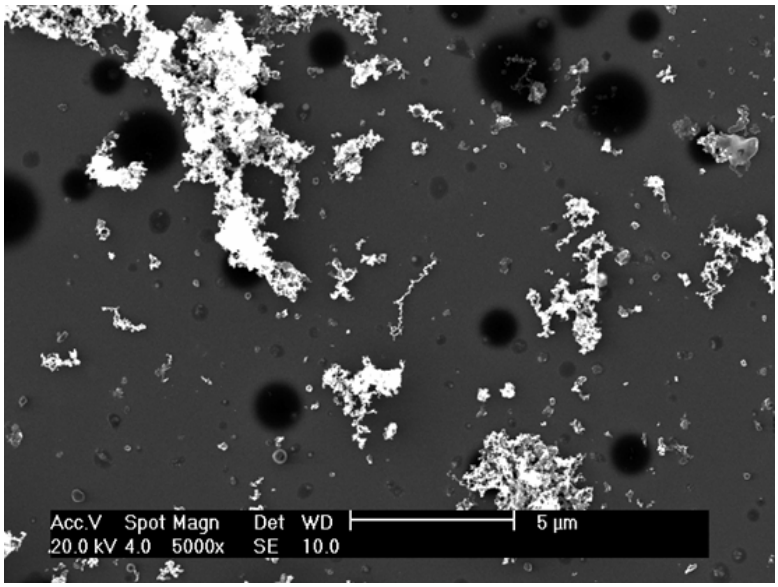

Figure 4.11 Chamise (burn B): extremely "sooty" sample with many typical soot chain particles; no liquid or oily organic particles are seen.

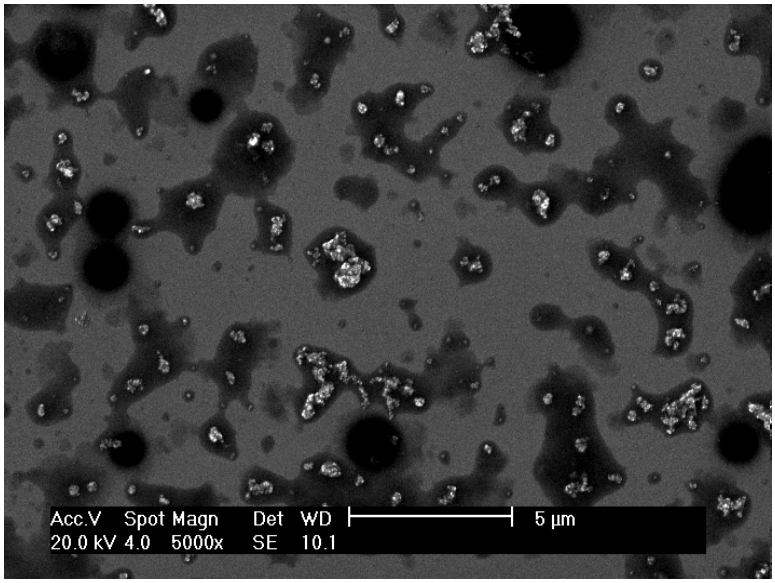

Figure 4.12 Ponderosa pine (burn A): sample dominated by organic carbonaceous particles, including oily liquid substances surrounding soot-like cores.

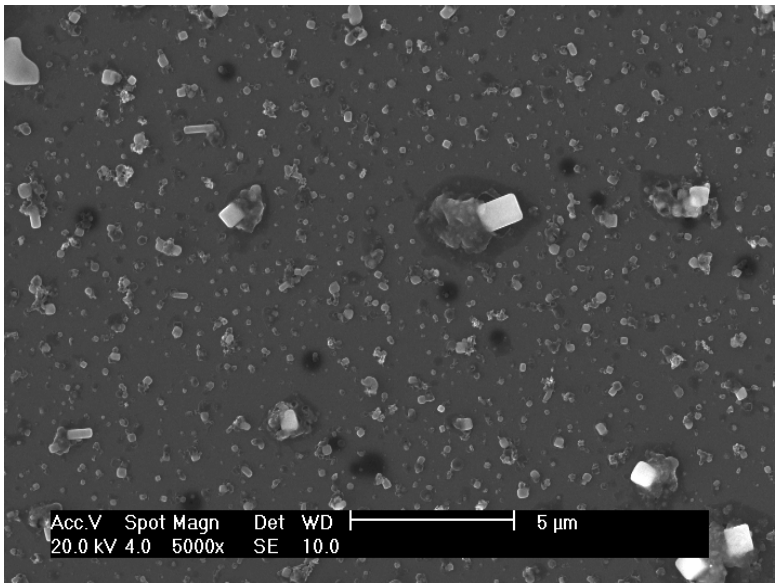

Figure 4.13 Rice straw (burn E): very little soot or liquid/oily organic particles present; KCl (inorganic) particles dominate and are believed to be mixed with organic materials.

4.5 Conclusion

The spectral response of absorption for light absorbing carbonaceous aerosols is quite complex. The simple assumption applied to BC aerosol of inverse wavelength dependence of absorption efficiency has been shown to be inaccurate for smoke from many biomass fuels. The substantial presence of organic carbon and inorganic components in addition to BC in certain biomass fuel aerosols affects aerosol optical properties. Wood smoke from these fuels scatters much more light than does typical BC aerosol, such as diesel soot. In addition the wood smoke exhibits increased absorption at shorter radiation wavelengths due to the presence of light absorbing organic material. In analysis of aerosols from biomass burning in remote sensing and modeling applications errors will be introduced by the extrapolation of absorption at longer wavelengths to UV

or short visible wavelengths under the commonly used model that the Ångström exponent of absorption is equal to one.

Biomass fuel classification is suggested by optical properties of the aerosol produced during combustion, based on the spectral response of absorption parameterized by the Angstrom exponent b and aerosol single scattering albedo, ω. Increased absorption at shorter wavelengths due to organic carbon in the particles and higher ω values separate combustion of many pines, duffs and rice straw from typical BC-producing fuels from mobile or industrial sources, such as diesel fuel. The fraction of organic materials present in smoke from fuels such as the shrubs chamise, manzanita, sage and rabbitbrush is considerably less than that of elemental carbon. Black carbon optical properties dominate for these dark and sooty fuels.

Additional research into the effects of combustion conditions of biomass fuels might provide further insight into determination of aerosol optical properties. Combustion of different fuels in the laboratory burns during FLAME 2006 was not uniform in terms of temperature or amount of flaming versus smoldering. For example, burning of the duffs produced very little flame as they generally smoldered, while the shrubs exhibited longer flaming periods and generally higher temperature combustion. It is postulated that in addition to composition, combustion may influence aerosol optical properties. This hypothesis deserves further investigation in laboratory and field studies.

4.6 References

Anderson, T. L., and Ogren, J. A. (1998). Determining Aerosol Radiative Properties Using the TSI 3563 Integrating Nephelometer. *Aerosol Science and Technology* **29**(1)**,** 57-69.

Andreae, M. O., and Gelencser, A. (2006). Black carbon or brown carbon? The nature of light-absorbing carbonaceous aerosols. *Atmospheric Chemistry and Physics Discussions* **6**(3)**,** 3419-3463.

Arnott, W. P., Hamasha, K., Moosmüller, H., Sheridan, P. J., and Ogren, J. A. (2005). Towards aerosol light absorption measurements with a 7-wavelength Aethalometer: Evaluation with a photoacoustic instrument and a 3 wavelength nephelometer. *Aerosol Science & Technology* **39,** 17-29.

Bergstrom, R. W., Russell, P. B., and Hignett, P. (2002). Wavelength Dependence of the Absorption of Black Carbon Particles: Predictions and Results from the TARFOX Experiment and Implications for the Aerosol Single Scattering Albedo. *Journal of the Atmospheric Sciences* **59**(3)**,** 567-577.

Bond, T. C. (2001). Spectral dependence of visible light absorption by carbonaceous particles emitted from coal combustion. *Geophysical Research Letters* **28,** 4075-4078.

Bond, T. C., Bussemer, M., Wehner, B., Keller, S., Charlson, R. J., and Heintzenberg, J. (1999b). Light Absorption by Primary Particle Emissions from a Lignite Burning Plant. *Environmental Science & Technology* **33**(21)**,** 3887-3891.

Houghton, J. T., Ding, Y., Griggs, D. J., Noguer, M., van der Linden, P. J., Dai, X., Maskell, K., and Johnson, C. A. (2001). "Climate Change 2001: The Scientific Basis." Cambridge University Press, New York.

Jacobson, M. Z. (2001). Strong Radiative Heating due to the Mixing State of Black Carbon in Atmospheric Aerosols. *Nature* **409**(6821)**,** 695-697.

Kirchstetter, T. W., Novakov, T., and Hobbs, P. V. (2004). Evidence that the spectral dependence of light absorption by aerosols is affected by organic carbon. *Journal of Geophysical Research* **109**(D21209)**,** doi:10.1029/2004JD00499.

Laskin, A., Iedema, M. J., and Cowin, J. P. (2003). Time-Resolved Aerosol Collector for CCSEM/EDX Single-Particle Analysis. *Aerosol Science and Technology* **37**(3)**,** 246-260.

Patterson, E. M., and McMahon, C. K. (1984). Absorption characteristics of forest fire particulate matter. *Atmospheric Environment* **18,** 2541-2551.

Schnaiter, M., Gimmler, M., Llamas, I., Linke, C., Jager, C., and Mutschke, H. (2006). Strong spectral dependence of light absorption by organic particles formed by propane combustion. *Atmospheric Chemistry and Physics Discussions* **6**(2)**,** 1841-1866.

Schnaiter, M., Horvath, H., Möhler, O., Naumann, K. H., Saathoff, H., and Schöck, W. (2003). UV-VIS-NIR spectral optical properties of soot and soot-containing aerosols. *Journal of Aerosol Science* **34,** 1421-1444.

5 Ambient Measurement in an Urban Environment

5.1 Introduction

As discussed in previous chapters, light absorption is often thought to be primarily due to the presence of atmospheric black carbon particulate matter. Light absorbing carbon aerosol is produced by incomplete combustion of carbonaceous fuels (Horvath, 1993). Aerosol light absorption is used to define black carbon mass concentration. That is, black carbon is an operational definition, indicating the use of optical methods in its determination (Bond and Bergstrom, 2006). However, depending on the wavelength, species other than elemental carbon may absorb light, especially for wavelengths in the near and mid-ultraviolet (UV). Carbonaceous compounds with spectral properties such that absorption increases significantly at shorter wavelengths in the visible and near-ultraviolet have been termed "brown carbon," to accent their optical properties (Andreae and Gelencser, 2006). The photoacoustic instrument's absorption measurement provides detailed information on ambient concentrations of light absorbing carbon aerosol (Arnott et al., 2005), the spectral properties of which will be explored further in later sections of the chapter.

Ambient measurements at the University of Nevada, Reno were made continuously beginning December 21, 2006 through January 3, 2007. Measurements of absorption and scattering properties of particulates in the atmosphere during that time were made using the dual-wavelength photoacoustic instrument for the purpose of evaluating its use in ambient measurement. The study was aimed at quantifying and confirming the reasonability of signal levels, instrument stability, and spectral variation.

Large variations existed between different days of the study due to meteorological conditions. Variations also existed on smaller time scales within particular 24-hour periods. This chapter presents analysis of the influence of meteorological factors on aerosol light absorption. In addition, the spectral properties of absorbing ambient aerosols and variation of these properties with time of day will be discussed.

5.2 Ambient Absorption Time Series

The dual-wavelength photoacoustic instrument is described in Chapters 1 and 2. An example of it is use in ambient measurements in given here. Ambient absorption measurements at 405 and 870 nm are shown in Figures 5.1a and 5.1b as measured by the dual-wavelength photoacoustic instrument on the University of Nevada campus for 14 days beginning Thursday, December 21, 2006. The instrument inlet was located outside the window on the third floor of the Leifson Physics building. A vacuum pump pulled ambient air through the instrument. Each data point is a two-minute average. The highest aerosol concentrations are present on the first day of observation, and other strong peaks are present late in the day on December 22, December 24 and January 2. Minimal absorption is seen on December 26 and 27. These variations can be understood in regard to meteorological conditions.

Comparing Figures 5.1a and 5.1b, the relative magnitude of the 405 nm and 870 nm measurements is roughly 2.3. The typical assumption for wavelength dependence is reciprocal dependence on wavelength, or 870/405 = 2.15. The wavelength dependence will be addressed in detail in Section 5.4.

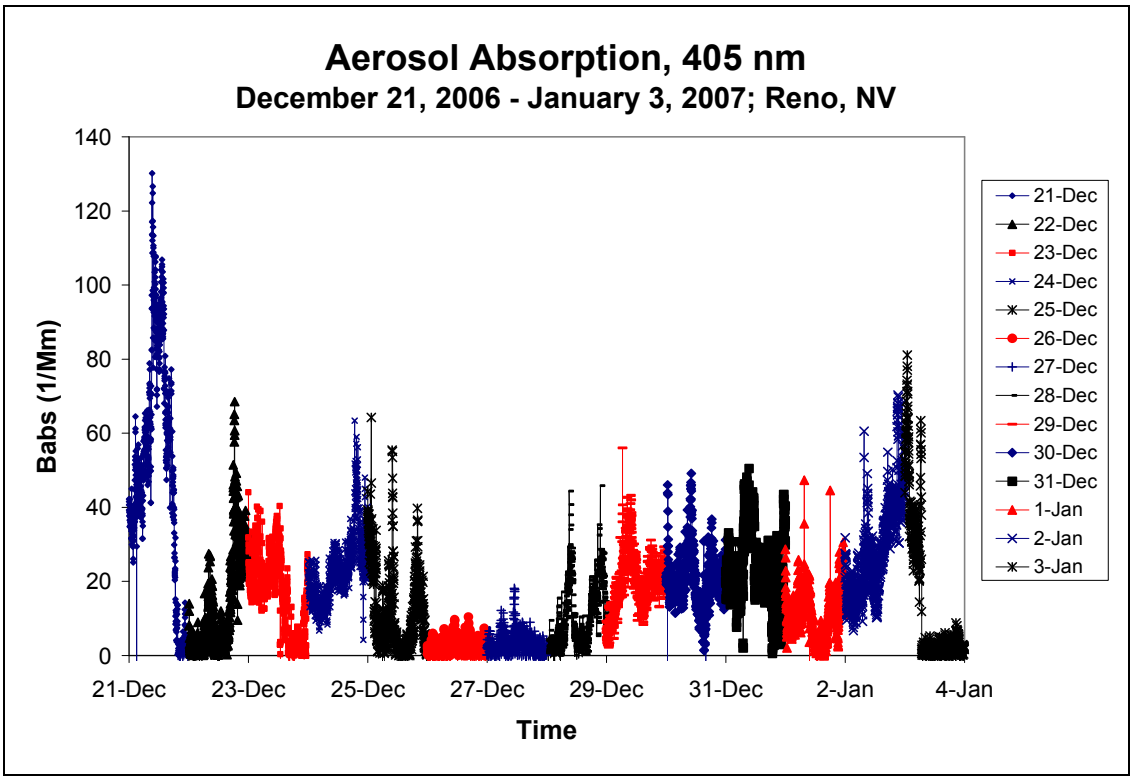

Figure 5.1a Ambient photoacoustic measurements of absorption at 405 nm

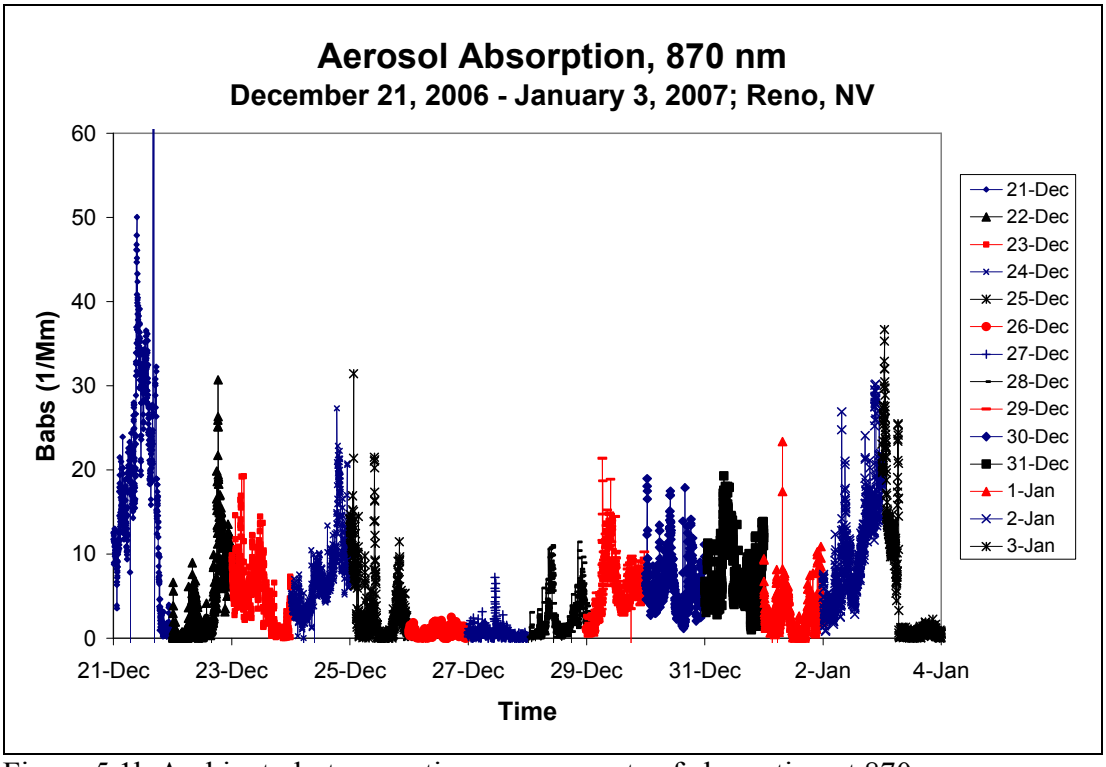

Figure 5.1b Ambient photoacoustic measurements of absorption at 870 nm

5.3 Meteorological Analysis

Along with source strength, meteorology plays a crucial role in determining aerosol concentrations. Given ever-present sources of light absorbing particles in an urban environment the atmospheric boundary layer where people live grows increasingly polluted under stable atmospheric conditions. Under these conditions ambient aerosol concentrations are able to build up, as no precipitation and little wind exists to remove particulate matter from the local atmosphere.

Stability of the atmospheric boundary layer is modeled here using wind speed measurements at the university obtained from the Western Regional Climate Center (WRCC), as well as near-surface conditions established from upper-air observations. Stagnation, as determined by relatively low wind speeds, is a characteristic of atmospheric stability. Increased wind speeds indicate a ventilating boundary layer in which one would expect low aerosol concentrations. Figure 5.2 depicts winds speeds measured at ten minute intervals at the University of Nevada, Reno Valley Road Farm from December 20, 2006 through January 3, 2007. When compared with the absorption time series plots of Figures 5.1a and 5.1b it is clear that days of relatively high recorded wind speeds, such as those with values above five miles per hour, correspond to days of low absorption by atmospheric aerosol. For example, absorption measured at 405 nm never exceeded 20 inverse megameters (Mm^{-1}) on December 26 and 27, and these were days that had the strongest winds with speeds greater than 20 miles per hour. This absorption coefficient value roughly corresponds to a black carbon concentration of approximately 2 $\mu g/m^2$, where a mass absorption efficiency of 10 m^2/g was used for the 405 nm wavelength. In addition, based on days of weak wind depicted in Figure 5.2, one

would expect increased aerosol concentrations on December 21, 24, December 29 through 31, and January 2. In particular, the second or third day in a row of low wind speeds, such as December 21 or January 2 would be expected to have exceptionally polluted conditions corresponding to increased amounts of time for accumulation of atmospheric particulate matter. Such high aerosol concentrations are confirmed in Figures 5.1a and 5.1b. The high absorption values on December 24 are similar to those present on December 21 and January 2.

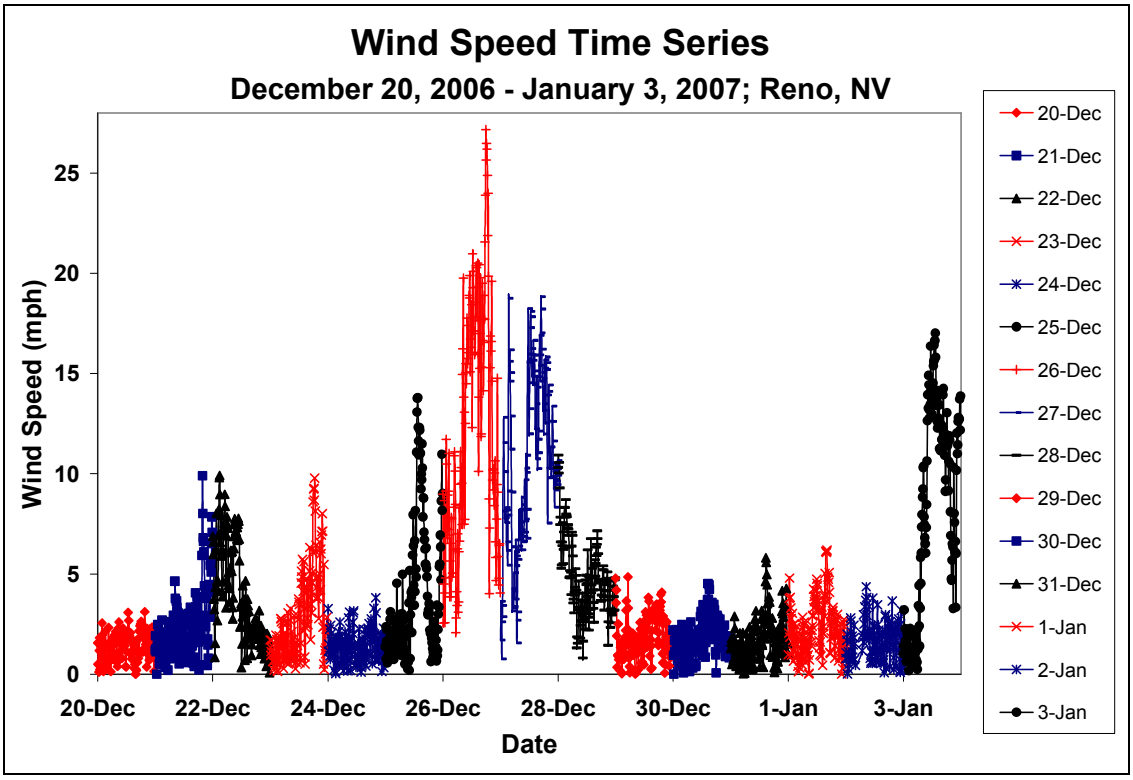

Figure 5.2 Wind speed, measured in miles per hour by WRCC

Very strong wind stagnation conditions are present on December 24, and stability on this day is further documented in the upper air observations for Reno plotted on Skew-T Log-P graphs shown in Figure 5.3a and 5.3b from the National Weather Service (NWS), as processed by the Atmospheric Science Department of University of

Wyoming. The atmospheric sounding data is acquired twice daily in Reno at 0:00 and 12:00 Greenwich Mean Time (GMT), corresponding to 16:00 (on the previous day) and 04:00 Local Standard Time (LST), respectively. The station identification number and station name abbreviation for Reno is acknowledged in the upper left-hand corner of the Skew-T Log-P plots. The sounding measurement time and date are documented in the lower left-hand corner. Figure 5.3a is the sounding for 04:00 LST and Figure 5.3b is for 16:00 LST on December 24. The most important feature of the sounding plots for the photoacoustic measurements featured in this ambient study is near the surface, indicated by the highest atmospheric pressures. A strong inversion (temperature increasing with height) can be seen in Figure 5.3a from the surface up to approximately 775 millibars (mb). The same feature is present at the surface on the morning of December 24th at 16:00 in Figure 5.3b, which shows the inversion layer reaching a height corresponding to a pressure of approximately 825 mb. Inversion layers accord extremely stable atmospheric conditions near the Earth's surface because the air parcels at the surface are colder and, therefore, heavier than those aloft. Surface air parcels sink or remain stagnant, allowing for pollutants to accumulate in the stable atmospheric environment.

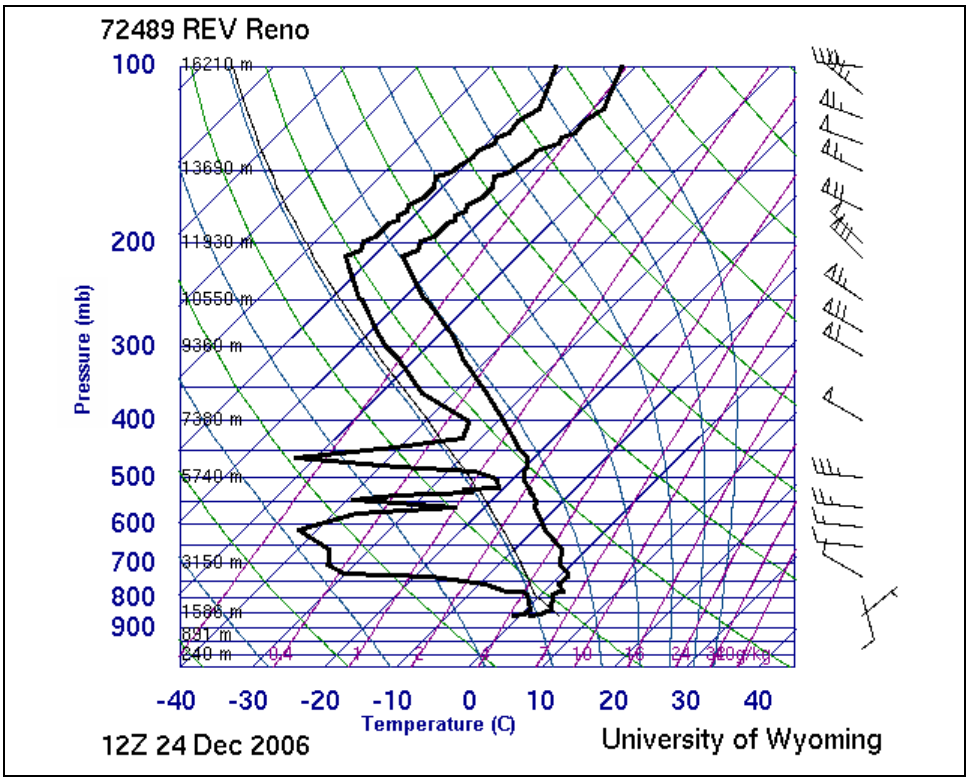

Figure 5.3a Reno atmospheric sounding: December 24, 2006; 04:00 LST

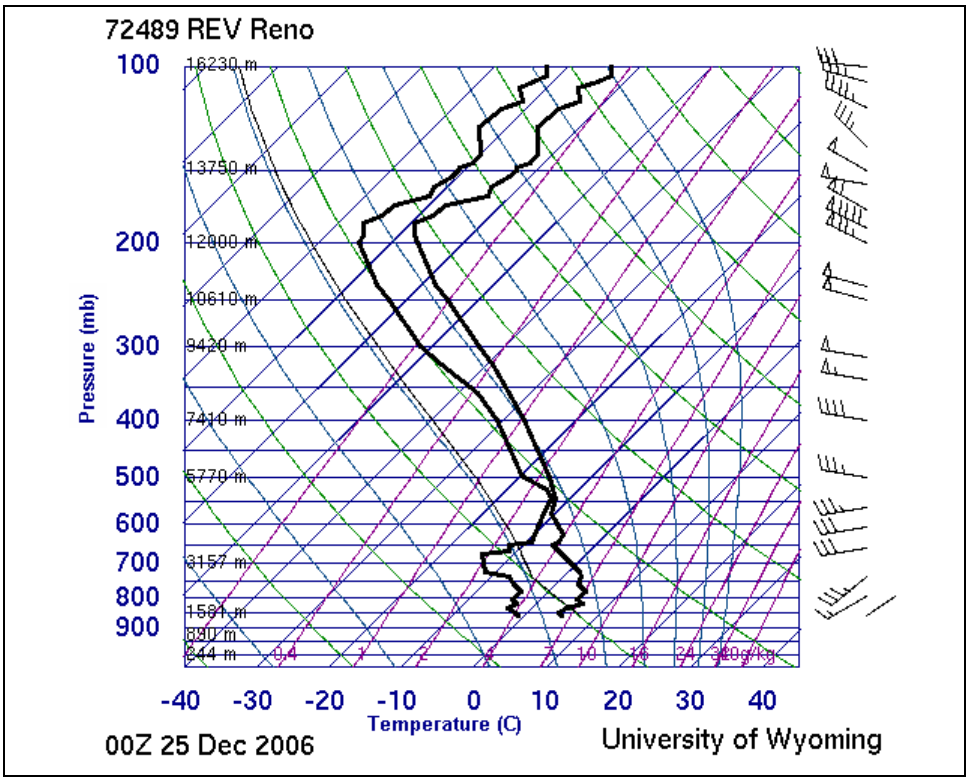

Figure 5.3b Reno atmospheric sounding: December 24, 2006, 16:00 LST

In contrast to those days featuring a strong surface inversion, Figures 5.4a and 5.4b depict atmospheric soundings from December 26, which had highest measured wind speeds and lowest aerosol absorption measurements. Figure 5.4a is the 04:00 LST sounding, and 5.4b is for 16:00 LST. No inversion is present at either of these times on the 26th of December. From the surface to pressures of at least 650 mb temperature decreases with height. The temperature curve is approximately parallel to the dry adiabats, indicating a well-mixed, dry boundary layer. The morning sounding also shows a cloud layer at 650 mb where the temperature and dew point curves meet.

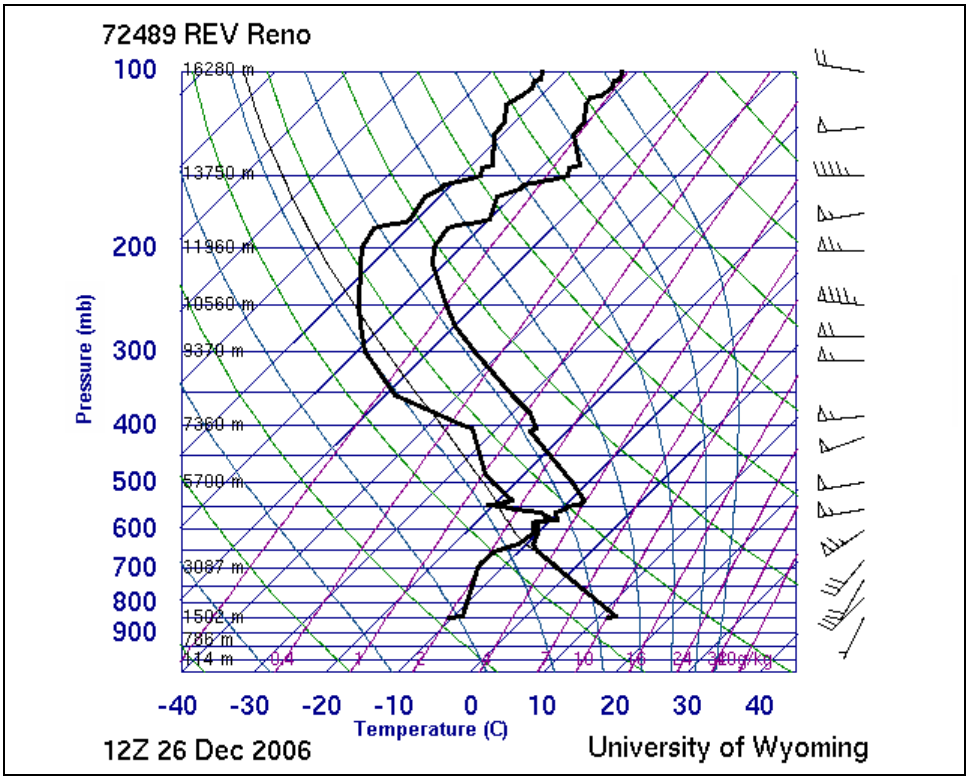

Figure 5.4a Reno atmospheric sounding: December 26, 2006, 04:00 LST

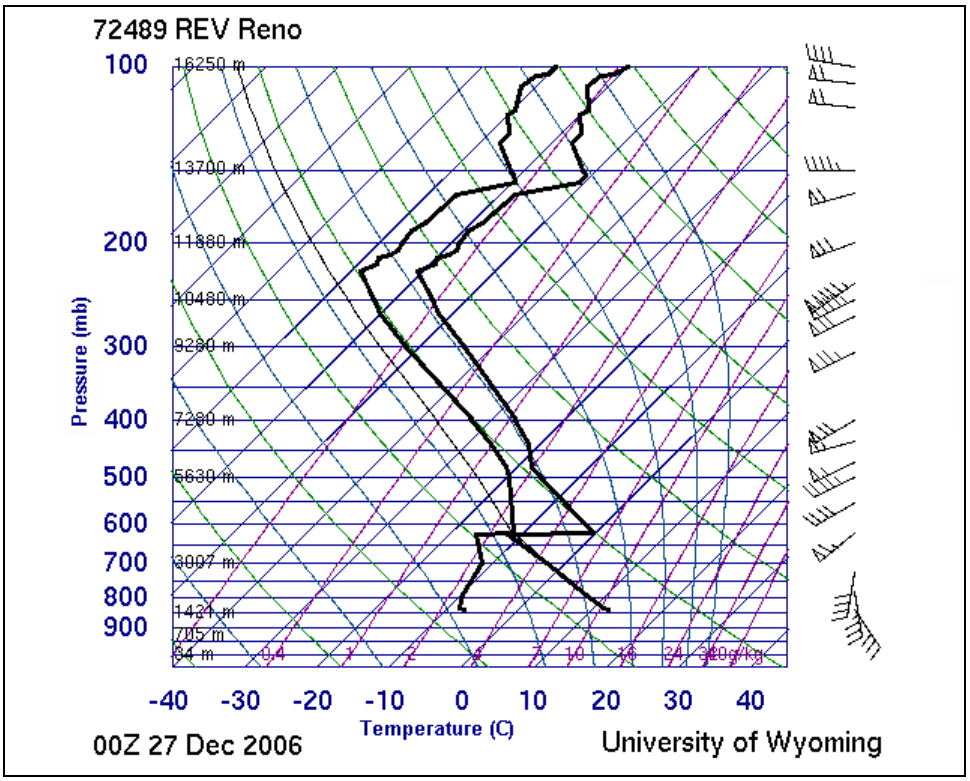

Figure 5.4b Reno atmospheric sounding: December 26, 2006, 16:00 LST

The direction and strength of atmospheric winds with height are depicted by wind barbs to the right of all Skew-T Log-P plots. Small winds of random direction are present at the surface under inversion conditions shown in Figures 5.3a and 5.3b. While upper-air observations indicate mostly westerly winds aloft on December 24 in these figures, surface winds are very weak and out of the east. Figures 5.4a and 5.4b however, depict stronger southerly surface winds on December 26.

Strong inversion conditions also existed at 04:00 on December 21, and a weaker surface inversion was still present at 16:00 on that day, as evinced in the third set of atmospheric soundings in Figures 5.5a and 5.5b. The surface winds are calm on December 21, as indicated by the open circle wind barb. The extremely high concentration of light absorbing aerosol present on December 21 can be understood by

taking into account the meteorological conditions present on that day: a stable and persistent low wind environment and a surface inversion layer. The 21st of December was one of the final days before the weekend marking the beginning of the Christmas holiday. Therefore, one might also expect considerably more road traffic contributing to high atmospheric aerosol concentrations on the 21st and 22nd than the following days.

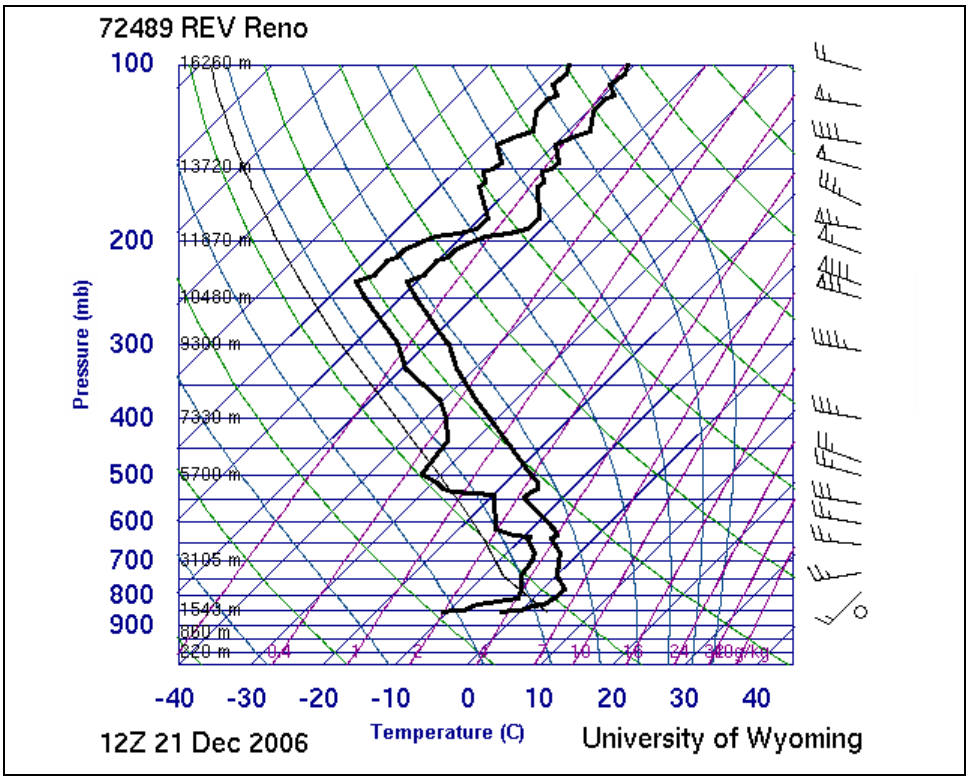

Figure 5.5a Reno atmospheric sounding: December 21, 2006, 04:00 LST

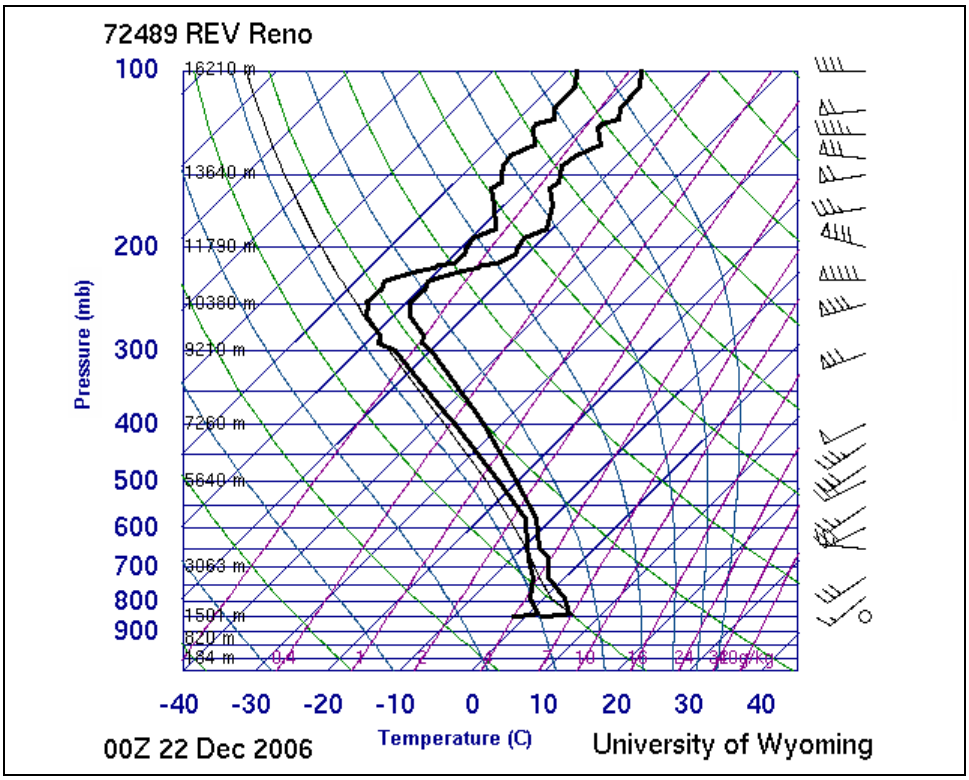

Figure 5.5b Reno atmospheric sounding: December 21, 2006, 16:00 LST

5.4 Spectral Variation of Ambient Aerosol Light Absorption

In addition to the longer time scale day-to-day fluctuations in light absorbing particle concentrations, variations in measurements exist within a single 24-hour period associated with activities such as rush hour traffic. In this section the days of the ambient study that had relatively large measurements of light absorption will be further analyzed and compared in order to elucidate any patterns in the aerosol sources and their relative importance by hour of the day.

Figures 5.6a and 5.6b depict absorption at 405 nm and 870 nm, respectively, as a function of time for the first five days of measurement. The time series in these figures covers a single 24-hour period. The patterns in absorption measurements discussed below do not apply to the very large values measured on December 21. The reason for this

discrepancy is thought to be due to meteorological conditions, and is highlighted at the end of Section 5.3. Later days of large absorption measurements are depicted in the same manner in Figures 5.7a and 5.7b. There are two separate peaks in absorption measurements for most high concentration days that can often be seen on Figures 5.6a and 5.6b and Figures 5.7a and 5.7b. The first increase takes place beginning at approximately 7:00 and peaks around 9:30 in the morning. Absorption values fall off substantially by approximately 11:00 but begin to rise again for the second time during the day at approximately 16:00. The increased aerosol concentrations during the morning and evening hours are attributable to workday vehicle traffic sources with maximum output during rush hour periods. Additional light-absorbing aerosol during a typical winter day in Reno is also supplied by residential heating sources such as oil or wood burning stoves, which are used most prevalently during evening hours.

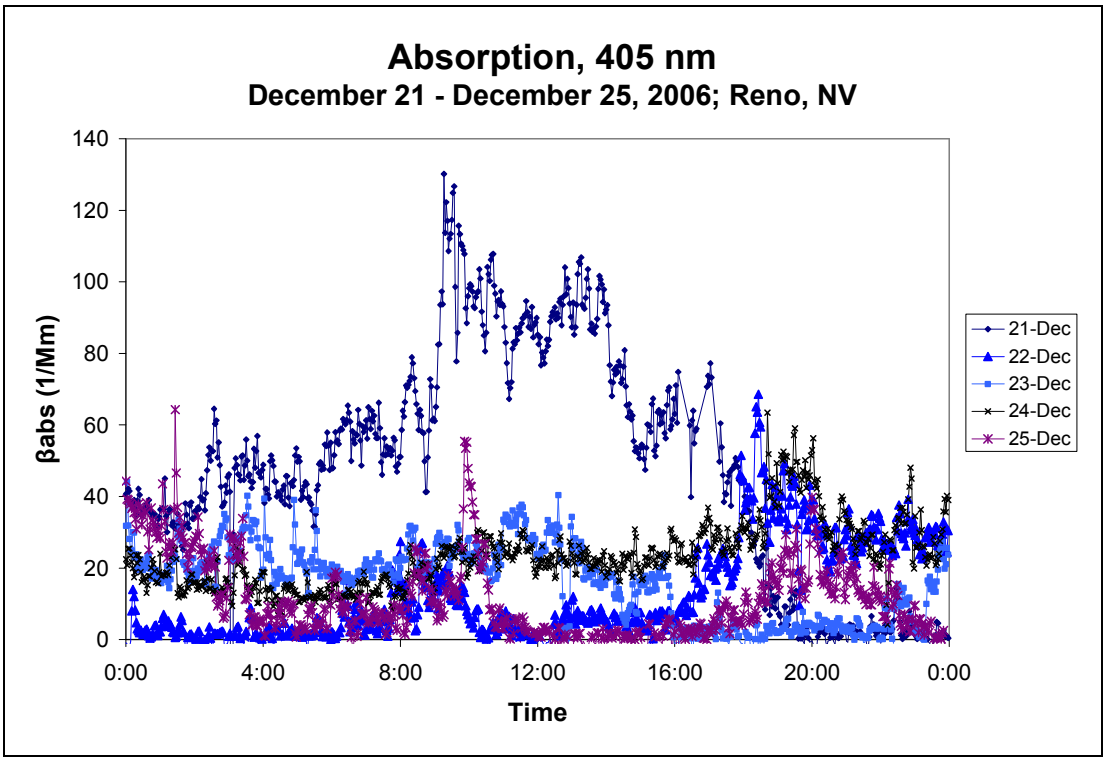

Figure 5.6a Ambient measurements of absorption over 24 hours, Dec. 21 – 25, 2006

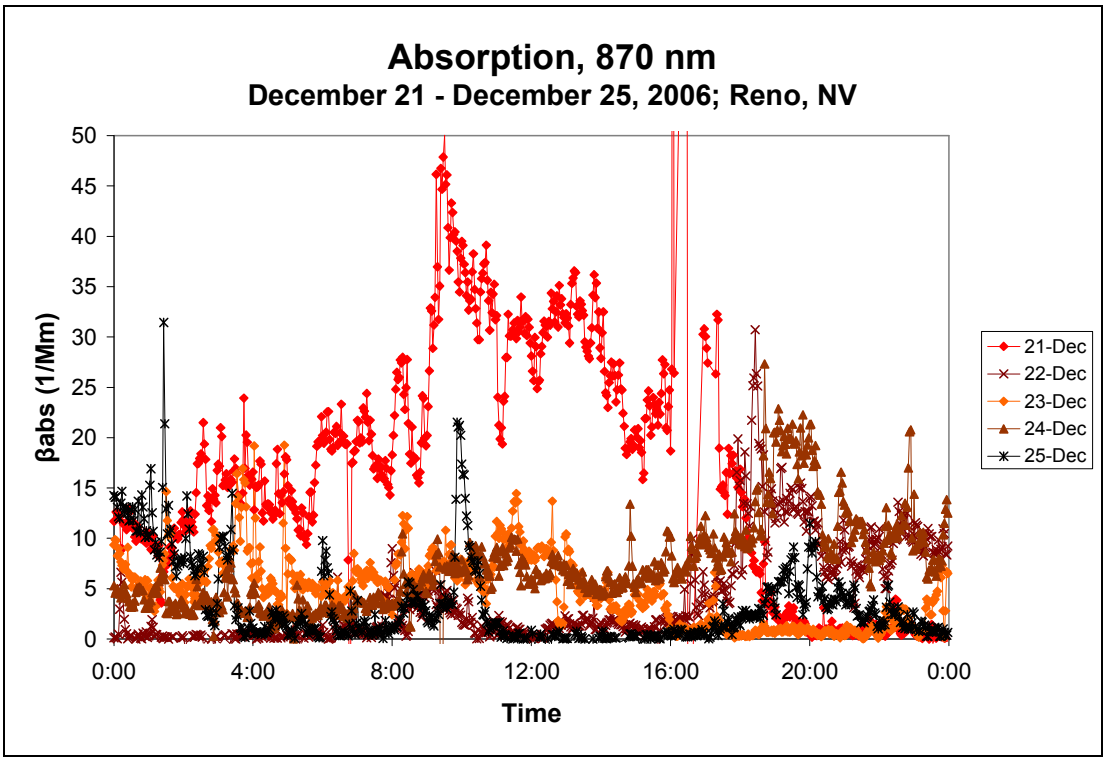

Figure 5.6b Ambient measurements of absorption over 24 hours, Dec. 21 – 25, 2006

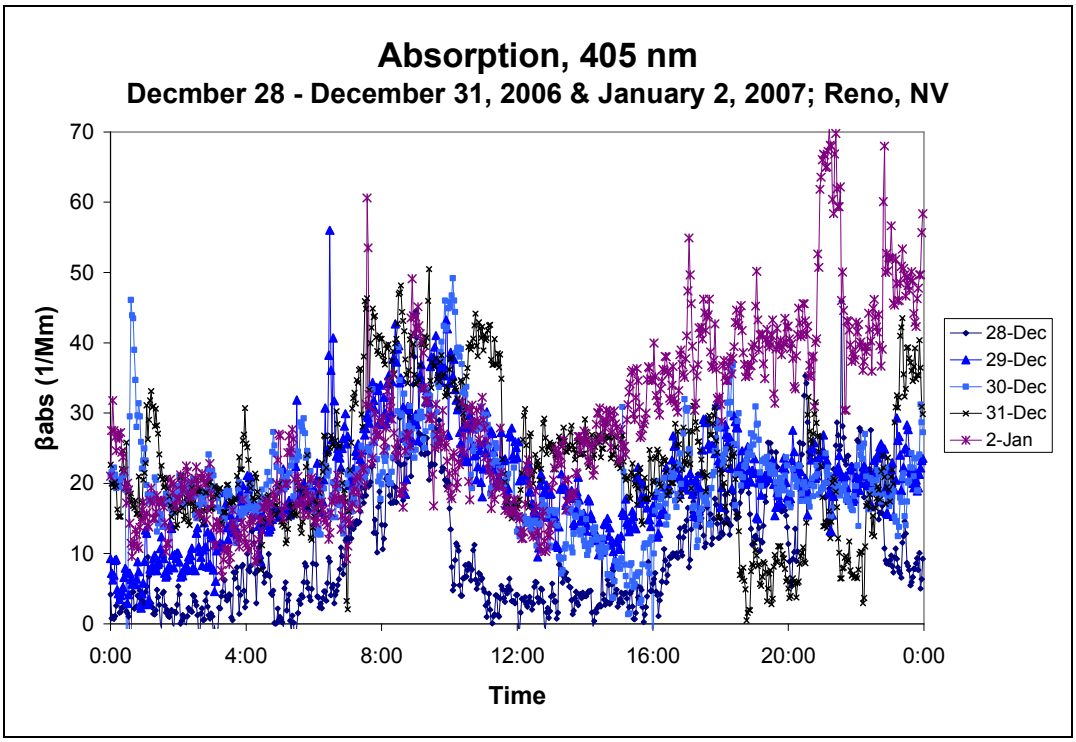

Figure 5.7a Ambient measurements of absorption over 24 hours, Dec. 28 – 31, 2006 and Jan. 2, 2007

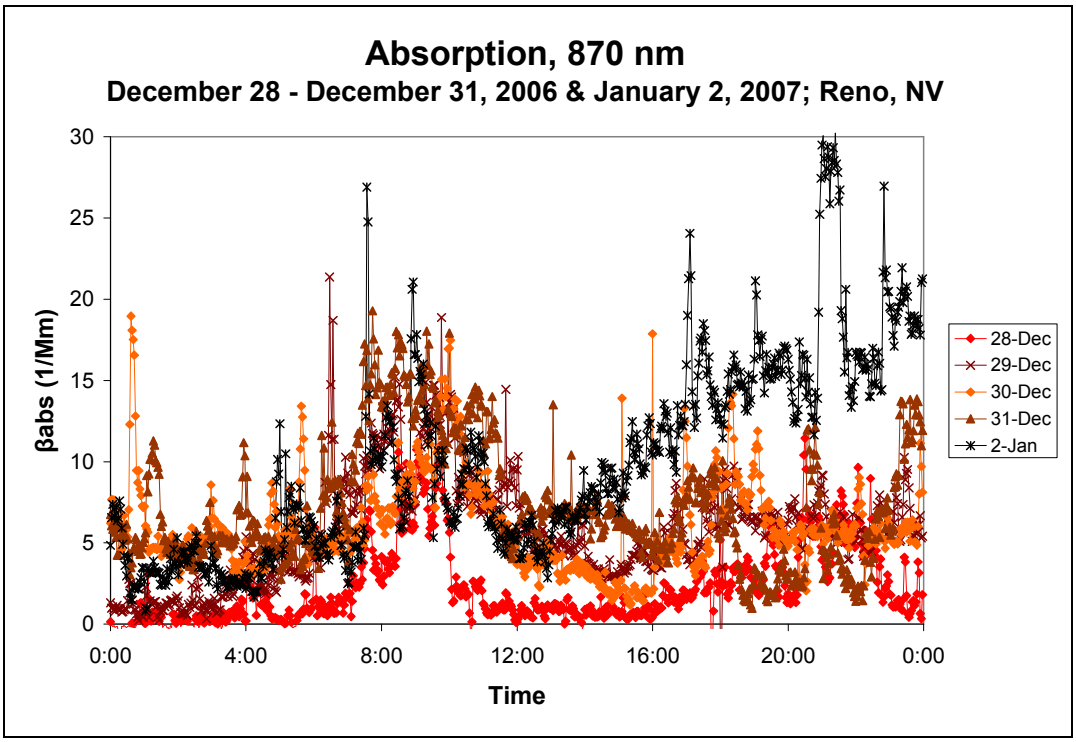

Figure 5.7b Ambient measurements of absorption over 24 hours, Dec. 28 – 31, 2006 and Jan. 2, 2007

In order to explore further the spectral properties and sources of absorbing ambient aerosol the dual-wavelength properties of the photoacoustic instrument are utilized. The parameter which measures the degree of spectral variation in absorption measurements at different wavelengths, the Ångström exponent *b*, was calculated. This parameter is responsive to the chemical composition of the aerosol. Recall, the Ångström exponent model is given by

$$\beta_{abs} = a\lambda^{-b} \quad . \qquad \text{(Eq. 5.1)}$$

β_{abs} in Equation 5.1 refers to the absorption coefficient measured at wavelength λ; a is a prefactor, and b is the Ångström exponent that characterizes spectral dependence. The expected b value for motor vehicle sources in which black carbon is the dominate species would be close to 1 (Bond and Bergstrom, 2006; Horvath, 1997; Schnaiter et al., 2003), while the expected values for wood or organic burning sources such as residential wood stoves would cover a broader range from 1 to 3 or more (Bond et al., 1999b; Hoffer et al., 2006; Kirchstetter, Novakov, and Hobbs, 2004; Schmid et al., 2006; Schnaiter et al., 2005). The difference in these values is due to light absorption by organic species present in relatively high concentration in the wood smoke.

The Ångström exponent was calculated using absorption measurements at 405 and 870 nm. Figure 5.8 depicts the average Ångström exponent for each day, as well as a horizontal line indicating the mean of those daily averages. The average values are calculated using only absorption measurements at 405 nm that are greater than 10 Mm^{-1} and the corresponding 870 nm signal in order to filter out data with a negligible or noisy signal.

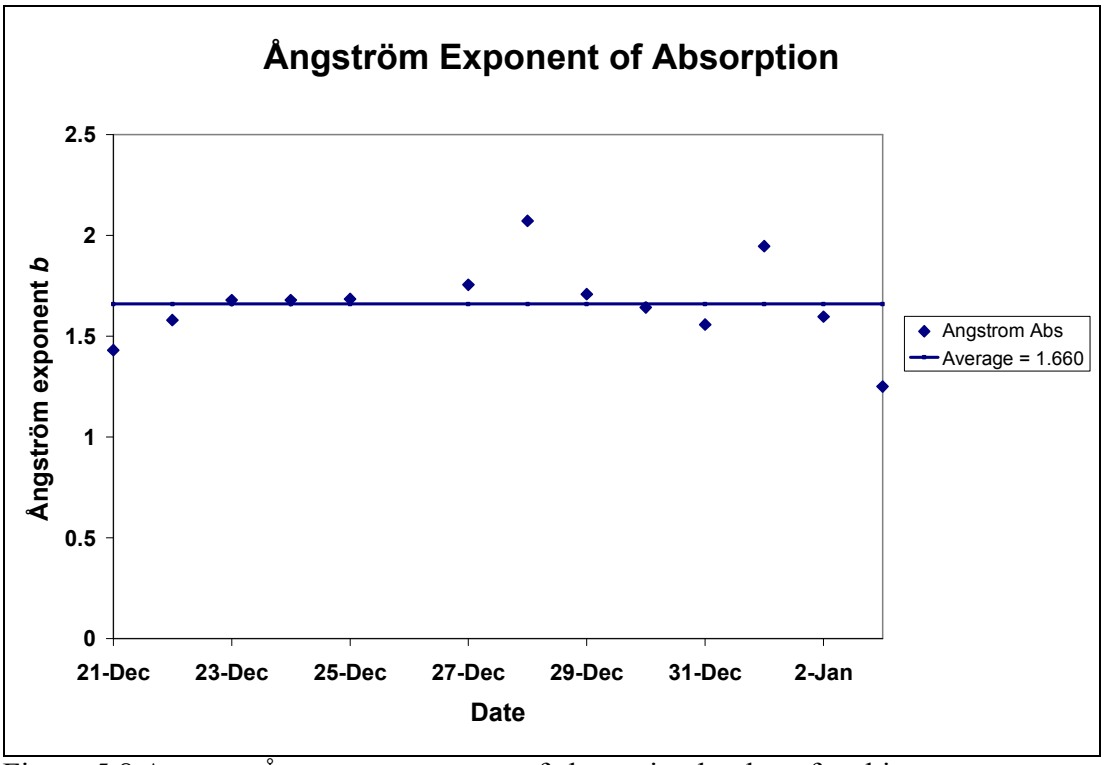

Figure 5.8 Average Ångström exponent of absorption by day of ambient measurement

While the Ångström exponent of absorption when averaged over the entire day is around 1.6, the fluctuation of this value throughout a single day shows certain patterns, as depicted in the Ångström exponent time series plot in Figure 5.9. This figure presents the Ångström exponent for absorption calculated using two minute average data from the dual-wavelength photoacoustic instrument, plotted as a function of time in a 24-hour day for each polluted day of the study. Three distinct periods are visible on Figure 5.9: Large variation in *b* values from midnight to 10:00, significantly less deviation from the mean from 10:00 to 16:00, and increased variation again from 16:00 to midnight. These three periods have been indicated on the time series in Figure 5.9.

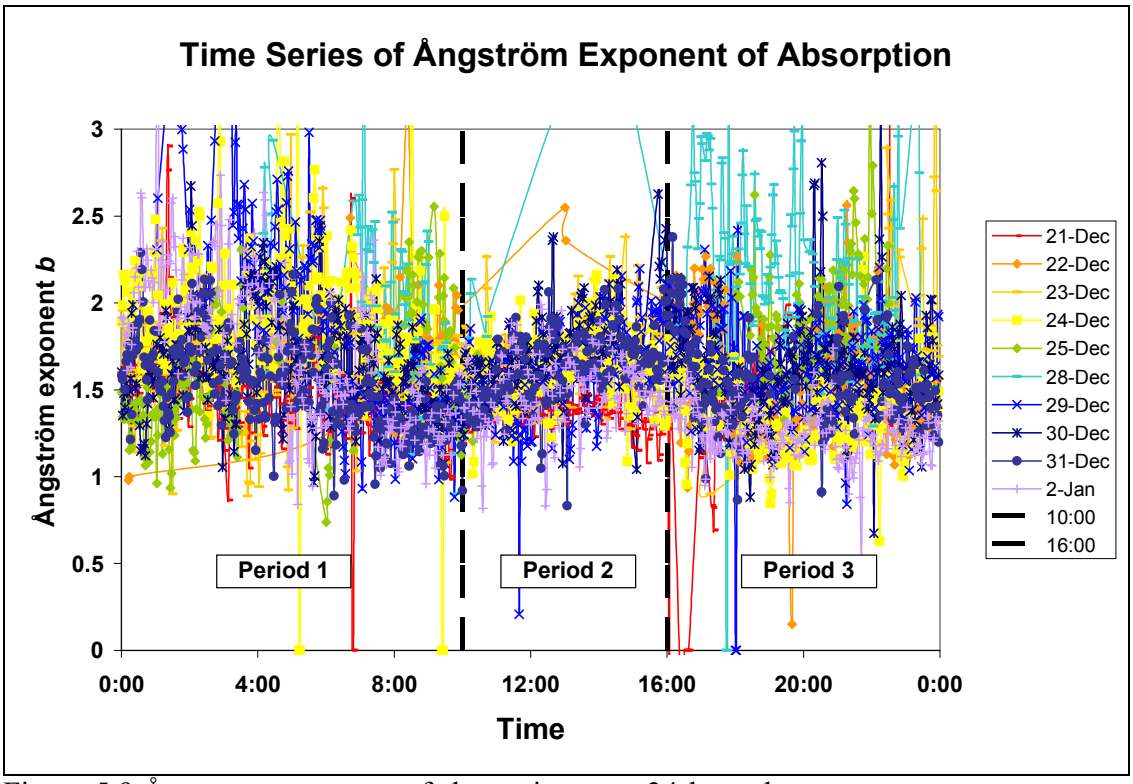

Figure 5.9 Ångström exponent of absorption over 24-hour day

The histogram analysis in Figures 5.10a, 5.10b, and 5.10c allows for further investigation into the spread and range of absorption Ångström exponent values during these three time periods. Each histogram corresponds to one of the three time periods mentioned above. The number of Ångström exponent values in each bin is indicated on the y-axis, and the x-axis indicates the minimum values of coefficient in the bin. The bin size is 0.2. For example, the largest column in Figure 5.10a indicates 600 occurrences of *b* values transpired from midnight to 10:00 over the scope of the study that were greater than or equal to 1.4 and less than 1.6. While most Ångström exponents calculated for all three time periods fell between 1.2 and 1.8, it is clear that the range of values is much greater from midnight to 10:00 (Figure 5.10a) and from 16:00 to midnight (Figure 5.10c) compared to the middle of the day (Figure 5.10b). In addition, both the morning and

evening values are right skewed such that the tail of the distribution is larger for higher Ångström exponents, whereas the distribution for the middle period of the day in Figure 5.10b is more symmetrical about its central peak. This variation in distribution by time period indicates a greater range of ambient aerosol sources during the earlier and later periods of the day, such as wood smoke plus motor vehicle aerosol, and a more consistent source in the intermediate period, such as motor vehicles alone. Furthermore, the long tails of distributions associated with periods 1 and 3 trending towards high Ångström exponents indicate ambient aerosols not only with a graphitic carbon nature, such as those from motor vehicles for which one would expect absorption Ångström exponents nearer to unity, but also aerosols containing organics and resembling wood smoke particles which have higher and more variant Ångström exponents, as discussed in detail in Chapter 4.

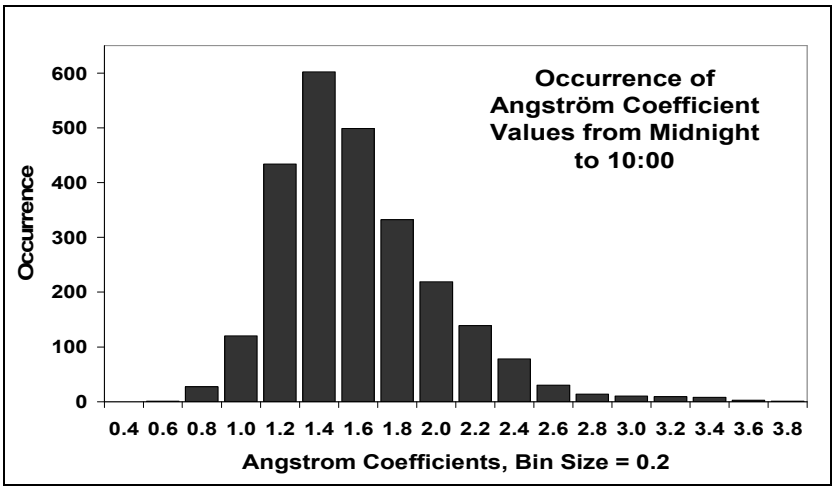

Figure 5.10a Distribution of *b* values from midnight to 10:00

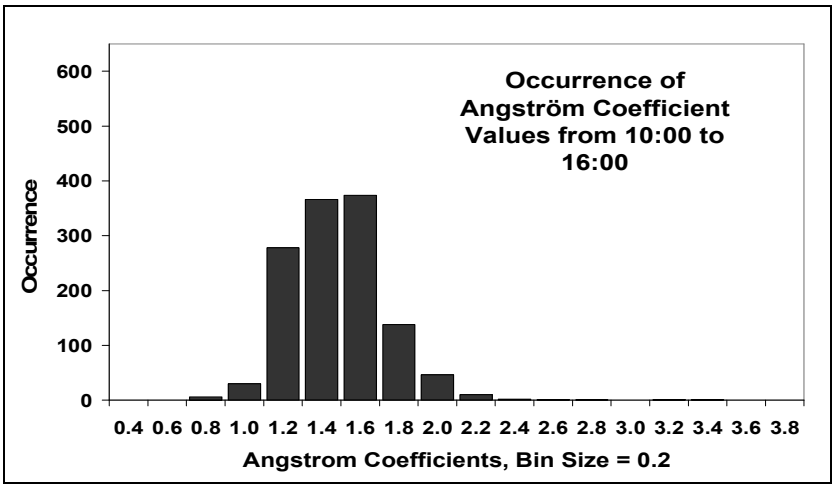

Figure 5.10b Distribution of *b* values from 10:00 to 16:00

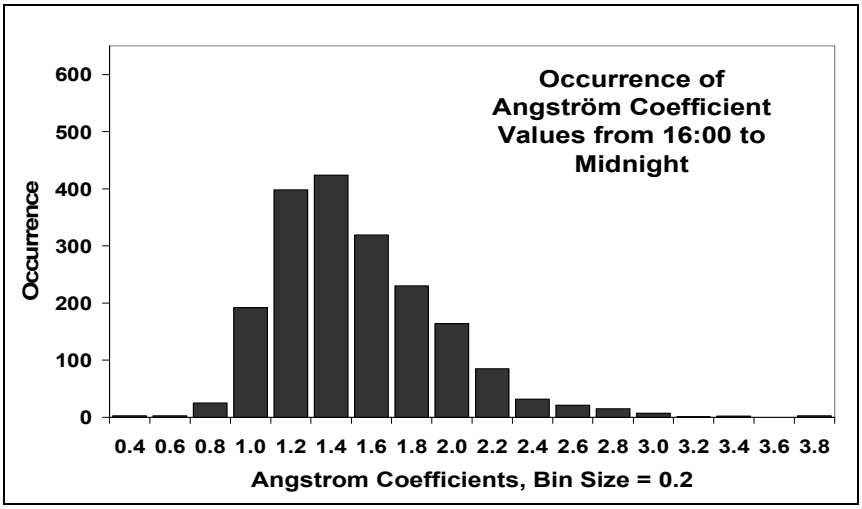

Figure 5.10c Distribution of *b* values from 16:00 to midnight

5.5 Conclusion

Correlations of meteorological data with absorption measurements made by the dual-wavelength photoacoustic instrument over a two-week winter period in Reno provide analysis of the instrument for use in ambient measurement. Signal strength and instrument stability are shown to be reasonable, and the dual-wavelength measurements of the photoacoustic instrument provide practical and interesting results which are perhaps useful in apportioning source aerosol between wood smoke and motor vehicle origin. Information on aerosol source strength and variation was inferred from photoacoustic data. Absorption by ambient aerosols produced during the central period of a winter day in Reno is presumed to be mainly due to black carbon components, and the aerosol sources are most likely combustion sources such as motor vehicles. The ambient aerosols present during early morning and evening exist in greater quantities. While still dominated by graphitic carbon, these aerosols also contain other absorbing components, such as organics, which exhibit larger Ångström exponents. Morning and evening atmospheric particle sources, therefore, probably include wood and organic material combustion, such as that from woodstoves.

5.6 References

Andreae, M. O., and Gelencser, A. (2006). Black carbon or brown carbon? The nature of light-absorbing carbonaceous aerosols. *Atmospheric Chemistry and Physics Discussions* **6**(3)**,** 3419-3463.

Arnott, W. P., Zielinska, B., Rogers, C. F., Sagebiel, J., Park, K., Chow, J., Moosmüller, H., and Watson, J. G. (2005). Evaluation of 1047-nm Photoacoustic Instruments and Photoelectric Aerosol Sensors in Source-Sampling of Black Carbon Aerosol and Particle-Bound PAHs from Gasoline and Diesel Powered Vehicles. *Environmental Science & Technology* **39**(14)**,** 5398-406.

Bond, T. C., and Bergstrom, R. W. (2006). Light Absorption by Carbonaceous Particles: An Investigative Review. *Aerosol Science and Technology* **40**(1)**,** 27-67.

Bond, T. C., Bussemer, M., Wehner, B., Keller, S., Charlson, R. J., and Heintzenberg, J. (1999b). Light Absorption by Primary Particle Emissions from a Lignite Burning Plant. *Environmental Science & Technology* **33**(21)**,** 3887-3891.

Hoffer, A., Gelencser, A., Guyon, P., Kiss, G., Schmid, O., Frank, G. P., Artaxo, P., and Andreae, M. O. (2006). Optical properties of humic-like substances (HULIS) in biomass-burning aerosols. *Atmospheric Chemistry and Physics* **6**(11)**,** 3563-3570.

Horvath, H. (1993). Atmospheric Light Absorption - A Review. *Atmospheric Environment* **27A**(3)**,** 293-317.

Horvath, H. (1997). Experimental calibration for aerosol light absorption measurements using the integrating plate method -- summary of the data. *Journal of Aerosol Science* **28,** 1149-1161.

Kirchstetter, T. W., Novakov, T., and Hobbs, P. V. (2004). Evidence that the spectral dependence of light absorption by aerosols is affected by organic carbon. *Journal of Geophysical Research* **109**(D21209)**,** doi:10.1029/2004JD00499.

Schmid, O., Artaxo, P., Arnott, W. P., Chand, D., Gatti, L. V., Frank, G. P., Hoffer, A., Schnaiter, M., and Andreae, M. O. (2006). Spectral light Absorption by ambient aerosols influenced by biomass burning in the Amazon Basin. I: Comparison and field calibration of absorption measurement techniques. *Atmospheric Chemistry and Physics* **6**(11)**,** 3443-3462.

Schnaiter, M., Horvath, H., Möhler, O., Naumann, K. H., Saathoff, H., and Schöck, W. (2003). UV-VIS-NIR spectral optical properties of soot and soot-containing aerosols. *Journal of Aerosol Science* **34,** 1421-1444.

Schnaiter, M., Schmid, O., Petzold, A., Fritzsche, L., Klein, K. F., Andreae, M. O., Helas, G., Thielmann, A., Gimmler, M., Mohler, O., Linke, C., and Schurath, U. (2005). Measurement of Wavelength-Resolved Light Absorption by Aerosols Utilizing a UV-VIS Extinction Cell. *Aerosol Science and Technology* **39**(3)**,** 249-260.

6 Summary, Conclusions, and Future Work

6.1 Summary and Conclusions

Photoacoustic measurement of light absorption and concurrent measurement of light scattering by reciprocal nephelometry, as reviewed in Chapter 1, provides a powerful method of aerosol and gas optical property analysis. The large dynamic range of measurement, the number of calibration methods available for instrument evaluation, and the simultaneous measurement of both absorption and scattering make the photoacoustic instrument an improvement upon much commonly used instrumentation to measure atmospheric aerosol optical properties.

Spectral properties of atmospheric particles are important in determining aerosol forcing of climate, atmospheric photochemistry, and in interpreting remote sensing measurements. Development and operation of the dual-wavelength instrument, described in Chapter 2, provides additional advancement in photoacoustic instrumentation, and affords analysis of the spectral dependence of aerosol optical properties. Dual-wavelength photoacoustic instrumentation allows for simultaneous measurement of absorption and scattering by atmospheric aerosol and gases at two separate wavelengths, without the drawbacks of particle/filter interactions and calibration assumptions of filter-based instruments. The instrument can also be simply calibrated using gases and aerosol with a range of optical properties, as described in Chapter 3. Unique measurements made by the dual-wavelength photoacoustic instrument in an urban ambient environment (Chapter 5) and laboratory measurement of wood smoke optical properties (Chapter 4) solidify confidence in instrument performance in various applications and provide

interesting results concerning the spectral properties of absorption by atmospheric aerosol from different combustion sources.

Absorption results from urban ambient measurements by the dual-wavelength photoacoustic instrument justify its use in ambient applications. Application of the instrument in an urban environment, based on results concerning spectral properties of absorption by wood smoke obtained during FLAME, hints at differentiation of source aerosol between motor vehicle and wood smoke origin. Absorption by ambient aerosol produced during the central period of a winter day in Reno, Nevada is presumed to be mainly due to black carbon components; aerosol sources are most likely motor vehicles. Ambient aerosol present during the early morning and evening exist in greater quantities, and in addition to black carbon contain other absorbing components, such as organics from wood combustion.

Increased absorption at shorter wavelengths compared to that expected for typical black carbon aerosol (for which absorption is expected to be inversely proportional to wavelength) was measured for wood smoke from a number of biomass fuels during the FLAME campaign in 2006. Increased absorption of shorter wavelength radiation is parameterized by an Ångström exponent of absorption greater than one, which was measured as high as three for certain fuel types. The spectral properties of these fuels indicate the presence in optically relevant quantities of some non-black carbon component, and are postulated to be due to high fractions of organic carbon constituents in the wood smoke. Chemical analysis of the aerosol from different fuels indicates large organic carbon fractions and lesser elemental carbon fractions in those fuels with increased absorption of near-UV and UV radiation. It is concluded that organic

components present in the smoke of many biomass fuels preferentially absorb shorter wavelength radiation. Spectral properties of this organic material indicate that casual use of the inverse wavelength dependence of aerosol light absorption in remote sensing and modeling applications can introduce large errors in UV and visible wavelengths when extrapolated from near-IR absorption for certain types of wood smoke.

6.2 Future Work

The primary development suggested for the photoacoustic instrumentation is improvement of the dynamic range of measurement of the scattering coefficient. High background scattering levels render high uncertainty in low-level scattering signal measurements. This improvement might be accomplished by removal of the multimode optical fiber coupling the light detector and photomultiplier tube. Additionally, distancing the windows that allow the laser beam to enter and exit the sample cavity from the center of the resonator where scattering measurement occurs would lower the scattering background, but at the expense of increased instrument size.

The evaluation of photoacoustic instrument calibration would be improved by a more sensitive means of measuring extinction, which would limit the gas or aerosol concentration needed for the calibration method. A more sensitive photodiode for laser intensity measurement might improve calculation of the sample's extinction coefficient. In addition, alternative gases to nitrogen dioxide could be used in evaluation of the absorption calibration, such as ozone or carbon dioxide gas.

Future work in analysis of biomass burning aerosol optical properties should include investigation into the role of combustion and fuel conditions (e.g. dry versus wet)

on absorption and scattering coefficients of the wood smoke. Additionally, the effects of relative humidity and particle coatings on absorption and scattering at different wavelengths could be explored.

Appendix A

A. Polynomial Fit of Acoustic Pressure Response Equation during Acoustic Calibration

In conducting aerosol light absorption measurements the temperature, pressure, and relative humidity-dependent values of Q and f_o are determined every 100 to 200 seconds. Q is the quality factor of the resonator and f_o is the resonance frequency. These values are measured using a piezoelectric transducer attached to the resonator by fitting a Lorentzian resonance curve of pressure versus frequency and using the values of Q and f_o as adjustable quantities. Such a resonance scan can be completed in about 5 seconds. In an effort to reduce this calibration time for measurements aloft a curve fit based on only five values of acoustic pressure versus frequency (restricted to near the vicinity of resonance) was proposed to replace the scan of 50 such values that were needed when using the previous crude curve fit.

The complex response of acoustic pressure in the frequency domain is provided in Equation 1.24. In practice calibrations with the acoustic transducer are fit to the magnitude of the acoustic pressure as a function of frequency

$$\left|P_m(f)\right|^2 = \frac{P_o^2}{1+\left(\frac{2Q(f-f_o)}{f_o}\right)^2}, \qquad \text{(Eq. A.1)}$$

where P_o is the peak pressure at resonance: $P_m(f = f_o)=P_o$. Please note that Equation A.1, as provided by Arnott et al. (2006), is incorrectly given in that publication without the square on the second term in the denominator. The inverse of this equation produces a second-degree polynomial function of frequency f

$$\frac{1}{\left|P_m(f)\right|^2} = \frac{4Q^2}{P_o^2 f_o^2} f^2 - \frac{8Q^2}{P_o^2 f_o} f + \frac{1+4Q^2}{P_o^2}. \qquad \text{(Eq. A.2)}$$

During an acoustic calibration a general polynomial fit of five input values of frequency within the vicinity of resonance is performed to determine corresponding inverse magnitudes of acoustic pressure. The following values are used in Equation A.2 as a starting point in the calibration: $Q = 70$, $f_o = 1500Hz$, and $P_o = 1$.

The quality factor is also equal to the resonance frequency divided by the frequency width at half maximum of the function represented in Equation A.1:

$$Q = \frac{f_o}{\Delta f}. \qquad \text{(Eq. A.3)}$$

From this relationship and the assumed values of Q and f_o, Δf can be approximated, and input values of frequency can be restricted to the vicinity of resonance. That is, five frequencies within the range $f_o \pm (2)\Delta f$ can be used as input values.

National Instrument's LabVIEW 7.0 software was used to write the virtual instrument code to conduct the polynomial fit and provide calibration measurements of f_o and Q. The virtual instrument operates as follows: the five frequency values, in Hertz, are entered into the *General Polynomial Fit.vi* as x-values, and the pressure measurements are first inverted and then entered as y-values. The *General Polynomial Fit.vi* returns the three polynomial coefficients, a, b and c, so that Equation A.2 can be expressed as

$$\frac{1}{\left|P_m(f)\right|^2} = af^2 + bf + c, \qquad \text{(Eq. A.4)}$$

where a, b and c are polynomial coefficients with the following values:

$$a = \frac{4Q^2}{P_o^2 f_o^2}, \qquad b = \frac{-8Q^2}{P_o^2 f_o}, \quad \text{and} \quad c = \frac{1+4Q^2}{P_o^2}. \qquad \text{(Eq. A.5)}$$

Therefore, manipulation of the polynomial coefficients in the following formulas returns the values of f_o, Q, and P_o:

$$f_o = \frac{-b}{2a}, \qquad Q = \frac{\sqrt{b^2}}{2\sqrt{\left(4ac - b^2\right)}}, \quad \text{and} \quad P_o = \sqrt{\frac{4a}{\left(4ac - b^2\right)}}. \qquad \text{(Eq. A.6)}$$

Note that the absolute value of polynomial coefficient b is obtained before it is entered into the formula for Q: $(b^2)^{1/2} = |b|$.

In summary, given a rough estimate of the quality factor Q and resonance frequency f_o, a limited number of frequency measurements within the vicinity of resonance and corresponding acoustic pressure measurements are fit to a simple polynomial equation. The polynomial equation is derived from the acoustic resonance response of microphone pressure. The polynomial fit returns more precise values of Q and f_o to be used in measurement of aerosol light absorption. The peak acoustic pressure at resonance P_o is also determined. This value is useful for assessing microphone calibration stability and microphone response under changing environmental conditions.